Marian Smoluchowski Institute of Physics
Faculty of Physics, Astronomy
and Applied Computer Science
JAGIELLONIAN UNIVERSITY

in collaboration with

Electronic Materials
Peter Grünberg Institute
FORSCHUNGSZENTRUM JÜLICH

Marcin Młynarczyk

Doctoral dissertation

Physicochemical properties of the $Sr_{1-x}Ca_xRuO_3$ thin films

Under supervision of:

Dr hab. Edward A. Görlich

and

Prof. dr hab. Krzysztof Szot

Kraków, March 2013

JAGIELLONIAN UNIVERSITY IN KRAKOW

JÜLICH FORSCHUNGSZENTRUM

I would like to express my gratitude to my supervisors.
First to Professor Krzysztof Szot for guiding me through the whole experimental work, supporting with ideas and most of all, for sharing his great experience with XPS.
Then to Doctor Edward A. Görlich for leaving no result undiscussed and no conclusion unquestioned and helping me to finally build a consistent image of all the analysed components.

I remain in debt to Professor Krzysztof Tomala for pointing me to the area of thin films and helping me to choose and refine the subject of this work.

My grateful thanks are extended to Dr. Adrian Petraru and Dr. Ulrich Poppe for introducing me to high pressure sputtering technique.

I deeply appreciate the help of my co-workers: Uwe Breuer who provided me with the TOF-SIMS data, Shaobo Mi who performed the HRTEM imaging, Dr. Andreas Gerber and Dr. Martin Wagner who let me assist them during RBS measurements, Mr. Jochen Friedrich who conducted thermogravimetry analysis and Dr. Bronisław Psiuk who spent hours acquiring the XPS spectra.

I also wish to thank Dr. Jürgen Schubert, Dr. Paul Meuffels, Dr. Lars Müller-Meskamp, Dr. Björn Lüssem, Dr. Reji Thomas and Dr. Arkadiusz Zarzycki for their guidance and assistance during AFM, STM, resistivity and magnetic measurements and for being supportive throughout the course of my studies.

Abstract

Epitaxial $Sr_{1-x}Ca_xRuO_3$ thin films were grown on $SrTiO_3$ and $LaAlO_3$ substrates with use of high pressure sputtering in a wide range of the deposition conditions. A many-sided characterization of the deposited layers revealed compositional inhomogeneity of a stratified character occurring naturally as a result of ruthenium deficiency. Although the deficiency was significant for the as-made samples and further increased by a storage or exposure to elevated temperatures the interior of the thin films tended to retain its nearly nominal stoichiometry.

Two competitive mechanisms of growth were a reason for a variety of observed topographical features. Locally, a transition from a pure layer-by-layer 2D mode to spiral 3D grains could be induced by several factors, e.g. an increased substrate-thin film lattice mismatch or higher calcium content.

The layers were grown fully strained to the substrate and the out-of-plane lattice constant of the $SrRuO_3$ thin films on $SrTiO_3$ approached the value estimated from the lattice cell volume of the bulk material whereas calcium doping led to its pronounced elongation, contrary to the bulk predictions.

Samples stored under normal conditions underwent extended over several days compositional change of the surface region, involving incorporation of water and carbon dioxide present in an ambient atmosphere and a subsequent rearrangement of the surface atoms. Annealing, even at moderately high temperatures also resulted in deterioration of the near-surface region under both, oxidizing and reducing conditions.

The shapes of the valence bands were similar for all the samples deposited on $SrTiO_3$ regardless of calcium content and consistent with theoretical calculations by other authors. The observed Fermi edge was indicative of their metallic character.

List of abbreviations

XRD – x-ray diffraction
AFM – atomic force microscopy
STM – scanning tunneling microscopy
LC-AFM – local conductivity atomic force microscopy
XPS – x-ray photoelectron spectroscopy
RBS – Rutherford backscattering spectroscopy
HRTEM – high resolution transmission electron microscopy
TOF-SIMS – time-of-flight secondary ion mass spectrometry
RP-phases – Ruddlesden-Popper phases
3D – 3-dimmensional
2D – 2-dimmensional
PLD – pulsed laser deposition
rms roughness – root mean squared roughness
FWHM – full width at half maximum
MOCVD – metal organic chemical vapor deposition
DOS – density of states
DFT – density-functional theory
LSDA – local spin-density approximation
GGA – generalized-gradient approximation
LMTO – tight-binding linear muffin-tin orbital
ASA – atomic sphere approximation
APW – augmented plane wave
SIC – pseudopotential with self-interaction correction
HPS – high pressure sputtering
UHV – ultra-high vacuum
SLA – straight line approximation
SIS – surface image system
χ_{min} – minimum ratio of the backscattering yield

Acknowledgements
Abstract
List of abbreviations

Contents

1. Introduction

It was in 1829 when Gustav Rose, German mineralogist and associate of Alexander von Humboldt, discovered calcium titanate during their expedition in the Ural Mountains. He named it after a Russian minister Lev Alekseevich Perovskiy, known mainly for his prowess in acquiring rare gemstones for the Tsar Peter the Great and even more for his own private collection. The term "perovskites" was later assigned to the whole class of compounds having the same type of a crystal structure. The name proved quite apt considering that several members of the family, like for example diamond-feigning strontium titanate, could undoubtedly attract Perovskiy's attention. However, it is not the appearance that makes the perovskites a subject of constant interest for nearly two centuries now. A simple atomic arrangement allows accommodation of many different cations and thus variety of new materials can be synthesized with a wide spectrum of interesting properties, like ferroelectricity or ferromagnetism. Thanks to their simple and well defined structure it is possible to obtain not only polycrystalline samples but also to grow single crystals and deposit thin layers of desired composition. In fact, in the modern solid state physics research perovskites remain under investigation mostly due to their potential in fabrication of nanodevices.

When I started my postgraduate studies at the M. Smoluchowski Institute of Physics at Jagiellonian University in Cracow, under supervision of Dr. Edward A. Görlich, my group had intensely worked on polycrystalline calcium doped strontium ruthenate perovskites ($Sr_{1-x}Ca_xRuO_3$). Having an opportunity to start collaboration with Prof. Krzysztof Szot at the Institute of Solid State Research at Jülich Research Center in Germany we decided to move our studies beyond the bulk compounds. When I was leaving Poland my task appeared to be simple: I was to produce single crystal $Sr_{1-x}Ca_xRuO_3$ thin films, verify their quality and bring home for further analysis of magnetic and transport properties. At the time, in Jülich undoped $SrRuO_3$ thin films deposited with high pressure sputtering on $SrTiO_3$ substrates were successfully utilized as electrodes in several types of multilayered structures. Therefore I was going to use this composition to enter the field of thin films deposition and characterization and at the same time create reference data for my later work with the Ca-doped compounds. Unexpectedly, a standard examination revealed major flaws of the obtained samples. A nearly perfect crystal structure and a surface topography reflecting atomic steps of the substrate were accompanied by a large average instoichiometry. Since the deviations from the nominal atomic ratios, even on a local scale, may significantly affect macroscopic properties of the material a detailed analysis was performed to acquire information selectively from different regions of the thin film. The results were intriguing enough to change the presumed area of interest and focus on a full structural characterization of $SrRuO_3$ and two Ca-doped thin film compositions promising improved compatibility with the $SrTiO_3$ substrate, namely $Sr_{0.8}Ca_{0.2}RuO_3$ and $Sr_{0.6}Ca_{0.4}RuO_3$. With the support of my supervisors I prepared the samples, verified their crystallinity with XRD and imaged the surface with AFM, STM and LC-AFM. I participated in XPS and RBS measurements. HRTEM and TOF-SIMS data were acquired by my co-workers. On the basis of the obtained results I was able to create a stratified model of the $Sr_{1-x}Ca_xRuO_3$ thin films.

The observed excessive aging of the samples brought to our attention the problem of the thermal and electrochemical stability of the ruthenates. Therefore a description of the changes induced by an exposure to hydrocarbon contaminations, a thermal treatment under oxidizing and reducing conditions or applied voltage was also included in this thesis.

Most of the results presented here were published in two extensive articles[1,2]. For the clarity the figures concerning particular subjects were grouped in the whole pages. I hope the reader finds it helpful.

2. Overview

2.1. Crystal structure

The $Sr_{1-x}Ca_xRuO_3$ ($0 \le x \le 1$) materials belong to a perovskite family having general stoichiometry ABO_3. The simplest crystal structure adopted by perovskites is cubic (fig. 1a) with the B-cation at the center of the cube, A-cations situated at the corners and oxygen anions occupying centers of the cube faces (Pm-3m space group). Such an ideal symmetry occurs only when the A- anb B-cations have fitting sizes, e.g. $SrTiO_3$ at room temperature. Any mismatch results in a distortion of the lattice. The Sr atoms are too small to appropriately fill the cubic cell with Ru cation in the center. In the literature it is commonly assumed that Ru cation and six nearest oxygen anions form a rigid octahedron having equal lengths of Ru-O atomic bonds and 90º O-Ru-O angles[3,4,5]. Accordingly, the distortion observed in this case is related only to a rotation of the RuO_6 octahedron about one or more axes (fig. 1a). Progressive substitution of Sr with even smaller Ca cations is expected to further increase this disorder leaving the octahedron intact.

To validate this approach a computer model of the octahedron was proposed for the purpose of this work. The (½, ½, ½) position of Ru ion and 90º O-Ru-O angles were fixed. The length of the Ru-O bond was set as a variable. Crystallographic <001> axis (z) was chosen as the first rotation axis. The second, so-called tilt axis was defined at the (00½) plane. The rotation and tilt angles as well as the exact orientation of the tilt axis were also set as variables. The model was then optimized to minimize the distances between calculated positions of oxygen ions $\vec{r}_{cal}$ and the positions $\vec{r}_{ex}$ obtained from the experimental data published by different authors[3,6,7,8]. Minimized least squares function S was defined as:

$$S = \sum_{i=1}^{6} \left[\vec{r}_{cal}(i) - \vec{r}_{ex}(i)\right]^2$$

For the 12 checked sets of data the average deviation of calculated positions was better than 0.06 Å. Moreover, a model with 3 different Ru-O bond lengths in perpendicular directions gave no better results than the one assuming a single bond length. Therefore the approximation of rigid octahedron seems to be sufficient for polycrystalline $Sr_{1-x}Ca_xRuO_3$.

Figure 2 shows obtained rotation and tilt angles. Such a large distortion affects also the cubic grid of A-type ions. The closest A-A distances differ up to 5% for $CaRuO_3$ (fig. 3a) and the angles are no longer equal to 90º (fig. 3b). A description in terms of a larger tetragonal cell (Pnma space group) becomes more appropriate (fig. 1b). The increase of Ca-doping leads to a smooth variation of the tetragonal lattice parameters (fig. 4 and 5) while the basic structural features are retained[3].

In case of epitaxial thin films the strain induced by the substrate may influence the crystal structure of the deposited material. At the same time the XRD analysis is limited to the reflections from the planes nearly parallel to the thin film surface and having lowest Miller indices, as the intensity of the XRD peaks depends on the number of atoms contributing to the diffraction. Thus in several aspects the $Sr_{1-x}Ca_xRuO_3$ thin film lattice will be referred to as pseudo-cubic. It is noteworthy that with increasing temperature the distortion of polycrystalline $SrRuO_3$ and $CaRuO_3$ decreases and both limiting compositions undergo a transition to cubic phase[9].

The $SrTiO_3$ and $LaAlO_3$ single crystals were used as substrates for the deposition of the $Sr_{1-x}Ca_xRuO_3$ thin films. Both perovskites are frequently used due to the fact that the lattice parameters of cubic $SrTiO_3$ (3.906 Å) and pseudo-cubic $LaAlO_3$ (3.792 Å) are very close to the pseudo-cubic parameters of the $Sr_{1-x}Ca_xRuO_3$ family and thus should provide a perfect atomic grid for a deposition of single crystal epitaxial thin films. First the $SrRuO_3$ thin films on $SrTiO_3$ were produced. This is a largely investigated configuration of the materials and as such was used as a reference. Further improvement of the structural quality was expected with a substitution of strontium with different element. In 1997 Eom et al.[10] investigated $SrRuO_3$ thin films doped with calcium. According to their work changing a level of doping with smaller calcium atoms on a strontium sublattice should reduce a lattice misfit with the $SrTiO_3$ substrate. Indeed, the analysis of the crystallographic data described above showed that the volume of the pseudo-cubic lattice cell of the $Sr_{1-x}Ca_xRuO_3$ bulk compound, in the range of $0.2 \le x \le 0.4$ approaches the value for the $SrTiO_3$ lattice cell. Therefore both compositions limiting this interval, namely $Sr_{0.8}Ca_{0.2}RuO_3$ and $Sr_{0.6}Ca_{0.4}RuO_3$ were used for the purpose of this study.

$ARuO_3$ (A = Sr, Ca) perovskites may also be viewed as a limiting composition of Ruddlesden-Popper (RP) phases $AO(AO\text{-}RuO_2)_n$ with $n \to \infty$, built up by stacking of AO and RuO_2 planes. RP phases consist of n consecutive perovskite blocks, each of them separated by a single rock salt layer (AO).

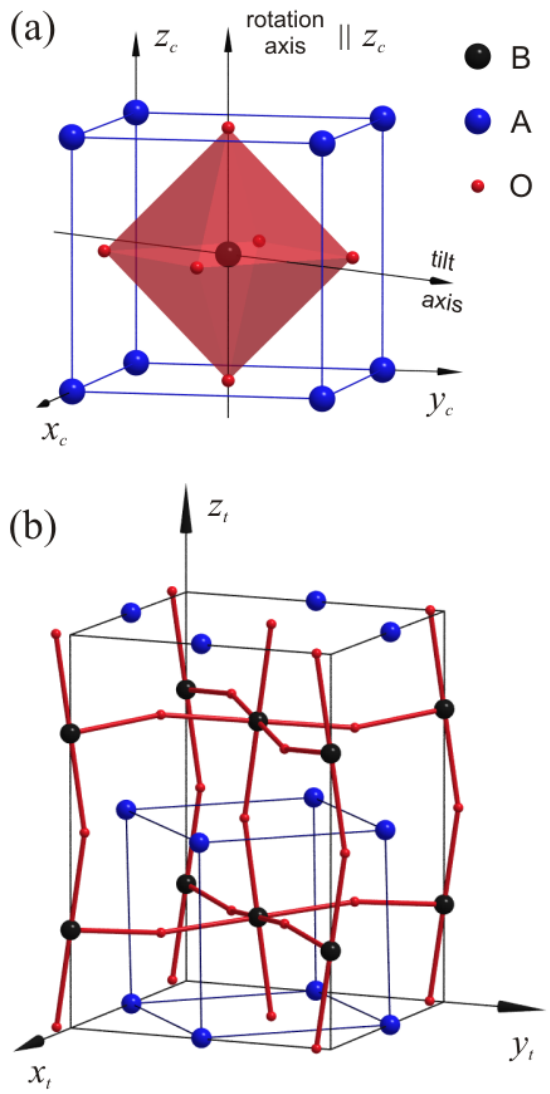

Figure 1
Perovskite ABO_3 crystal structures. Transformation from simple cubic (Pm-3m) (a) to tetragonal (Pnma) (b) occurs through a rotation and a tilt of the BO_6 octahedron.

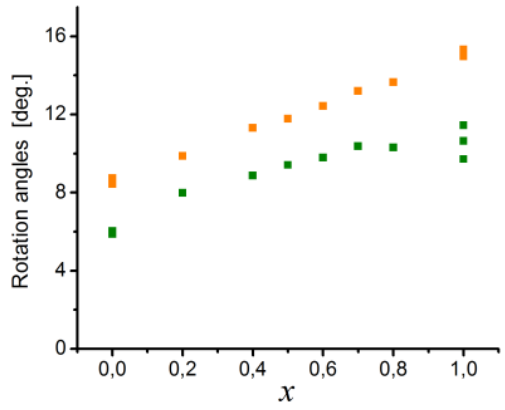

Figure 2
The rotation (green) and tilt (orange) angles of the RuO_6 octahedra for polycrystalline $Sr_{1-x}Ca_xRuO_3$ calculated in this study.

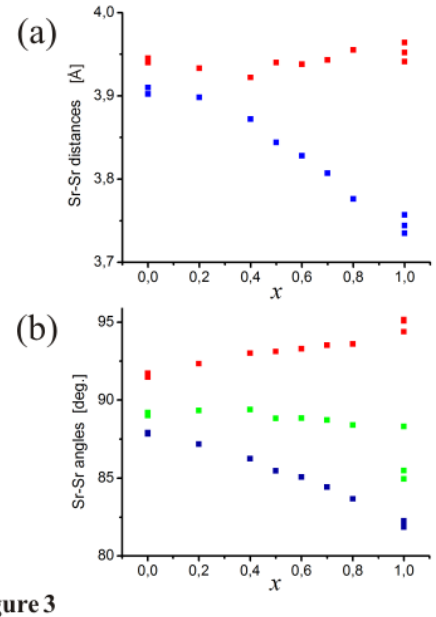

Figure 3
Minimum (a – blue) and maximum (a – red) distance between closest A-type cations, A-A-A angles calculated at one corner of the distorted-cubic lattice cell (b) of polycrystalline $Sr_{1-x}Ca_xRuO_3$ for the data obtained from the literature /Ref. 3, 6, 7, 8/.

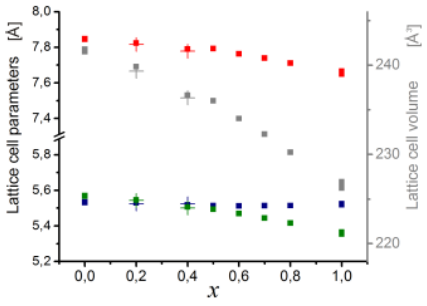

Figure 4
Tetragonal lattice cell parameters (red, blue, green) and volume (gray) for polycrystalline $Sr_{1-x}Ca_xRuO_3$. Values calculated for the materials used for thin film production (crosses) are shown compared to the data published by other authors (squares) /Ref. 3, 6, 7, 8/.

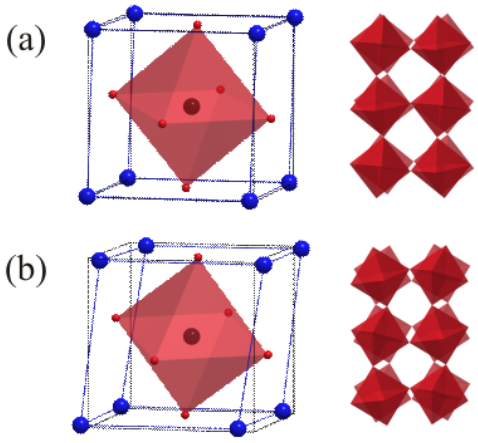

Figure 5
Crystal lattice distortion of polycrystalline $SrRuO_3$ (a) and $CaRuO_3$ (b).

The RP phases with lower n may appear locally in the $ARuO_3$ samples as a result of stoichiometry deviations. It is an important problem because high volatility of ruthenium oxides makes it very difficult to obtain a stoichiometric thin film with no Ru deficiency. Accommodation of defects, namely Ru vacancies in the $ARuO_3$ structure follows a typical path[11]. At low concentration the vacancies are randomly distributed, contributing significantly to the configurational entropy. When the number of defects increases interactions between them become important leading first to appearance of defect clusters and finally to a formation of extended planar defects i.e. shear planes. Interactions through Coulomb forces and elastic forces impose a superlattice ordering of the extended planar defects thus constitutes a homologous series of compounds (RP phases). This way the defects can be coherently inserted in the host structure at a low cost of their enthalpy of formation. The ordering of such structures can be a kinetically very slow process therefore variable spacing between planar boundaries is frequently observed. On the other hand similar incorporation of additional Ru atoms in the perovskite structure is unlikely. Even little excess of RuO_2 in the $SrRuO_3$ thin films accommodates as separate precipitations[12].

2.2. Bulk properties of the limiting compounds

A large family of perovskite compounds has been subjected to extensive research for decades now, due to a broad spectrum of interesting properties and possible applications. Variety of compositions is nearly infinite considering that pure $ARuO_3$ compounds can be easily modified through a substitution of the A- or B-type cations at a chosen sublattice. Among the $Sr_{1-x}Ca_xRuO_3$ materials until now, both limiting compositions ($x = 0$, $x = 1$) attracted particular attention.

Bulk samples of the $SrRuO_3$ and $CaRuO_3$ compounds exhibit resistivity temperature dependence of metallic character, with room temperature values below 300 μΩ·cm in both cases[13,14]. $SrRuO_3$ is an itinerant ferromagnet with a transition temperature T_C of approximately 160 K[15,16]. Introduction of about 9% Ru vacancies suppresses ferromagnetic ordering, lowering T_C to 45 K and surprisingly, increasing the lattice cell volume[17]. Dilution of the strontium sublattice by the calcium atoms leads in the $Sr_{1-x}Ca_xRuO_3$ bulk system to a systematic decrease of the Curie temperature. Schneider *et al.*[18] obtained the T_C values of about 105 K for $x = 0.2$ and 60 K for $x = 0.4$ from the inflection point of magnetization, Roshko et al.[19] slightly higher values of about 120 K and 75 K, respectively. The ferromagnetism disappears via a quantum phase transition at the calcium concentration $x \cong 0.7$ [18,20]. Materials with higher Ca content are nonmagnetic metals. $CaRuO_3$ stays paramagnetic down to milikelvin temperatures[14,21]. Further studies of the boundary compounds covered a wide range of properties including thermodynamics of formation[22,23] or electronic structure calculations[24] as well as experimental measurements[8]. Both materials were also doped with several elements, mostly with the 3d transition metals on the $Ru\text{-}O_2$ sublattice. Among others $SrRuO_3$ was doped with Zn, Ni, Mn, Co, Cr[25], Zr[26] and Pb[27] and $CaRuO_3$ with Cu[28], Sn[27], Ti, Fe[29], Al, Zn, V, Pt, Mn, Co and Ni[30]. Investigations mainly focused on the influence of such a substitution on structural, magnetic and electrical properties.

2.3. Thin films production

Nonetheless technological potential of ruthenium perovskites is bound to the properties of thin films. The properties of the materials deposited as a sub-micrometer coating covering a base grid of another compound (substrate) may be quite different from their corresponding bulk form as a result of the presence of strains, atomic disorder and variation of oxygen concentration in the films[31,32]. The chemical composition, quality of the structure and surface termination of the substrate may also have a great impact on physical properties of the deposited layer[33,34]. Therefore it is obvious that a problem of structural perfection, including individual features of the surface region is extremely important for the materials with a possible application as a part of thin multilayered devices.

Most of the modern deposition techniques allow the thin film growth by a progressive condensation of the compound supplied in its gaseous form. If a single crystal specimen is used as a substrate providing lateral spacing of atoms similar to that of the material being deposited, there exists a possibility that a new forming layer will strictly accept the same arrangement. This, so-called epitaxial type of growth may occur in several different modes[35]. In the Volmer-Weber mode particles arriving at the substrate surface concentrate in numerous favorable sites such as structural defects. These sites act as nucleation centers from which the deposited material spreads over the entire surface. A large number of nuclei disrupt their full coalescence leading usually to a 3-dimmensional (3D) columnar growth of the thin film. In the 2-dimmensional (2D) Frank-van der Merwe mode a new layer nucleates only when the coalescence of the

one below is completed on a large area. It is possible if the number of nucleation sites is limited and the growth proceeds mainly at the edges of the newly formed islands (layer-by-layer growth). For the monocrystal substrates with a low concentration of defects the favorable sites are located at the edges of the atomic steps. If the mobility of the adparticles is sufficient single atoms and atomic complexes can diffuse to those places and the new layers form simply as extensions of the substrate steps (step-flow growth). Unidirectional flow of the steps can be obtained by introduction of a controlled substrate miscut. This type of growth is usually desirable as the produced samples are highly uniform and homogeneous. The Stransky-Krastanov mode is considered intermediate between the two previously described. If the strain coming from the lattice mismatch between the substrate and the deposited material is significant the layer-by-layer growth proceeds only up to a certain critical thickness. Above this limit a rapid transition to a 3D island growth is observed. All the types of growth can be affected by some unfavorable phenomena like step bunching or screw-islands growth. The step-bunching occurs when the higher layer catches up with the lower one and they move together. The steps built in this manner may have the heights of several monolayers. The screw-islands usually result from an intensified nucleation around a screw dislocation.

It is clear that each type of growth differently affects the properties of the obtained samples and therefore its characterization cannot be omitted in the thin film description.

Until today virtually every known technique was utilized to produce the $SrRuO_3$ thin films. Mostly PLD with XeCl or KrF excimer laser was utilized, at deposition temperatures varying from 350 to 810 ºC, and oxygen pressures in the range of 0.03-0.5 mbar[36,37]. Usually preparation conditions were optimized to obtain the lowest resistivity and a flat surface. The best films, with rms roughness about 0.1 nm and rocking curves with FWHM lower than 0.1º, were grown at temperatures 640-800 ºC and oxygen pressures 0.1-0.4 mbar[36,38]. Several other methods, such as 90º off-axis sputtering[39] at a temperature and pressure range 300-680 ºC and 0.03-0.1 mbar, respectively, techniques requiring extremely low oxygen pressures (10^{-6}-10^{-3} mbar) such as magnetron sputtering[40], ion beam sputtering[12] or molecular beam epitaxy[41], but also high pressure sputtering[42], MOCVD[43] or spin coating[44] have been successfully applied. Most of them give the results comparable with PLD. Mainly $SrTiO_3$ substrates have been utilized, because of a small lattice mismatch. $LaAlO_3$ and MgO substrates were chosen whenever a strain resulting from a larger misfit of the lattice parameters was desired[45].

The $CaRuO_3$ thin films have been produced mostly by means of 90º off-axis sputtering[46,47] and PLD[48,49]. The sputtered samples were deposited at the temperatures in the range of 660-710 ºC and oxygen pressure of 0.01-0.1 mbar or 0.13 mbar O/Ar mixture. Their thickness usually exceeded 100 nm. PLD parameters were 600-800 ºC and 0.1-0.13 mbar of oxygen. Other utilized techniques included rf-magnetron sputtering[50] and MOCVD[51]. $LaAlO_3$ and in some cases $SrTiO_3$ monocrystals were used as substrates. Reported FWHM values of the rocking curves were 0.16-0.33º and rms roughness higher than 1 nm[50,51].

2.4. Technological application

In the course of research done within several years $SrRuO_3$ attained a status of the first-choice thin film to use as an electrode in several applications. Its lattice parameters make it perfect for an epitaxial deposition on substrates like $SrTiO_3$, $LaAlO_3$ or $NbGaO_3$ [10] and the lattice mismatch can be further reduced with buffer layers like $CaHfO_3$[52] or $Ba_{1-x}Sr_xTiO_3$[53]. $SrRuO_3$ is not only a standard bottom electrode for the $(Pb,La)(Zr,Ti,Nb)O_3$ and $(Ba,Sr)TiO_3$ families of ferroelectric capacitors[54,55] but it is also a common metal layer in $SrRuO_3/YBa_2Cu_3O_7$ Josephson junctions[56], $SrRuO_3/Sr_2YRuO_6$ magnetic tunnel junctions[57] and others. The thin film itself was also subjected to basic research[58,59], including such phenomena as quantum oscillations in electrical resistivity[60] or magnetic anisotropy[61]. Other studies concerned changes induced by a substitution of Sr with Na[62], by a substitution of Ru with Fe[63], Co, Mn[64,65], Sn[66] or Ti[67] and also introduction of oxygen deficiency[36] or ruthenium excess[68]. For instance a certain concentration of titanium turns the thin film into a paramagnetic insulator, ruthenium excess is accommodated as metallic precipitations and oxygen vacancies are reflected in increasing resistivity of the specimen.

Contrary to a general opinion that the $SrRuO_3$ thin film structure is thermally and electrochemically stable[69,70,71] there exist several reports stating that $SrRuO_3$ is highly reactive in atmospheres containing hydrogen at the temperatures as low as 200 ºC[72], that it decomposes during vacuum annealing close to a temperature of 600 ºC [72] and that structural changes may appear after a subsequent deposition of a different layer on top of it[69]. Decomposition in vacuum occurs at even lower temperatures if the surface was previously contaminated by an exposure to air, leading mainly to a formation of numerous

RP phases[73]. Therefore the stability of the $SrRuO_3$ thin films is limited to the processes conducted in oxygen containing ambience within certain limits of the oxygen partial pressure and the temperature.

Properties of the $CaRuO_3$ thin film were also widely investigated[46,50] and its structural compatibility with $Pb(Zr,Ti)O_3$ compounds, giving potential for application as a bottom electrode was confirmed[51]. Although examples of utilization can be found in literature[74] the compound has never been widely used in fabrication of multilayers. On the other hand this material offers an intriguing playground for basic research due to unusual properties, e.g. a non-Fermi liquid behavior observed in the resistivity[75].

The resistivity of both limiting compositions strongly depends on deposition parameters, thin film thickness or the substrate used. It is possible to obtain $SrRuO_3$ and $CaRuO_3$ samples having positive thermal coefficient of resistivity with a room temperature value in the range of 200-300 $\mu\Omega\cdot cm$[48,76] and thus showing properties similar to those of the bulk materials. Accordingly, photoemission spectra confirmed existence of occupied electronic states near the Fermi level[77,78]. However, frequently a minor modification of the deposition procedure results in a change of the thermal coefficient to negative and the resistivity values rising as high as to justify a description in terms of metal-insulator transition. For instance, significant worsening of conductivity was observed for $SrRuO_3$ samples deposited in low temperatures[76] or low ambient oxygen pressure[36] and $CaRuO_3$ samples deposited in high temperatures[48]. It was also observed that the $CaRuO_3$ thin films consist of conductive and insulating regions and their macroscopic conductivity improves with the sample thickness[48] as well as the quality of the substrate[46]. Additionally both boundary compounds displayed a sign reversal of the Hall-effect[79].

2.5. Theoretical calculations

Several attempts were made to describe the electronic band structure of the $Sr_{1-x}Ca_xRuO_3$ crystal. The DOS was calculated by means of the density-functional theory (DFT) within the local spin-density approximation (LSDA)[80,81,82,83,84,85,86] or generalized-gradient approximation (GGA)[24]. The tight-binding linear muffin-tin orbital method (LMTO)[8,24,80,81,83] was commonly used but utilization of the atomic sphere approximation (ASA)[8] was also reported. The computations involved the augmented plane wave (APW) method[24,84,85,86] or the pseudopotential with self-interaction correction (SIC) method[86]. Spin-orbit coupling[24,81] and other relativistic effects were included in some models[24]. Additionally the Hubbard model was applied[86] to improve a description of the bands near the Fermi level.

The total and partial DOS was calculated for $SrRuO_3$ in an idealistic cubic[80,81,83,86] and a real distorted structure[8,80,81,82,84,85,86], for $CaRuO_3$ cubic[24,81,83] and distorted structures[8,24,81,84] and several $Sr_{1-x}Ca_xRuO_3$ intermediate distorted structures[24]. The main features of the obtained DOS structures were similar. A short characterization of the aforementioned theoretical methods can be found in the appendix A.

The electronic states near the Fermi level originate from the interactions between overlapping Ru4*d* t_{2g} and O2*p* orbitals. The resulting Ru4*d* t_{2g}-O2*p* antibonding (π^*) electronic band starts at the binding energy of about 2 eV from the Fermi level and extends beyond it. The band is more than half filled therefore it is responsible for the metallic behavior of the materials. Recent studies situate the center of this band at a binding energy of about 0.5 eV and show a negligible contribution from above 1 eV. Larger distortion or longer Ru-O bonds expected with Ca-doping reduces overlapping of the orbitals, narrowing the bands and decreasing conductivity. The Ru4*d* t_{2g}-O2*p* bonding (π) and O2*p* nonbonding states appear at the energies from 2 eV to 10 eV, the latter being closer to the Fermi level. Most of the calculations predict a small gap or a semigap (a gap in the majority spin band) between the antibonding and nonbonding band, wider in case of $CaRuO_3$ than $SrRuO_3$. The Sr4*d*, Ca3*d* and Ru4*d* e_g unoccupied states are situated at the energy range of 1.5-5 eV beyond the Fermi level and have little influence on the properties of the materials.

2.6. Ca-doping

There exists a lack of systematic experimental studies of calcium doping influence on crystallographic and physical properties of the thin films of the $Sr_{1-x}Ca_xRuO_3$ system. Available evidence in the literature concerning earlier studies of the intermediate compounds is rather scarce. The dependence of out-of-plane lattice constant on *x* that is its systematic decrease with the higher calcium content was presented for the thin films deposited on $LaAlO_3$ [87] and $SrTiO_3$ [88]. In the first case the 250 nm composition-spread samples were grown with PLD by a sequential deposition of sub-monolayer amounts of the materials from the $SrRuO_3$ and $CaRuO_3$ targets with the substrate passed behind the slit-shaped aperture. The concentration of Ca was obtained from energy-dispersive x-ray spectroscopy and confirmed with RBS measurements. The out-of-plane lattice parameters obtained with XRD were slightly larger

than those of the bulk compounds in the whole range of Ca concentration. The samples on $SrTiO_3$ were produced by metalorganic aerosol deposition at the temperatures in the range of 900-940 ºC on (100) oriented polished substrates. The out-of-plane spacing decreased from about 3.93 Å for $x = 0$ to about 3.82 Å for $x = 1$. AFM scans of the $Sr_{0.8}Ca_{0.2}RuO_3$ and $CaRuO_3$ thin films showed oriented rectangular blocks more than 10 nm high confirming an epitaxial type of growth. No further structural analysis was conducted. A minimal ratio of a backscattering yield of 2.1% was reported for a sample with $x = 0.5$, deposited on $SrTiO_3$ [10]. For some compositions valence band x-ray absorption spectra were shown but with little characterization of the thin films[89]. Among the physical properties the electrical resistivity and magnetization were widely investigated[18,49,87,90].

The referenced reports focused mostly on a single property, measured as a function of concentration. In the present study this approach is shown to be insufficient to assess the quality of the thin film. The thesis points out that several features of the deposited layer, such as crystal structure parameters, average stoichiometry and in-depth as well as lateral compositional homogeneity should be taken into consideration for a complete understanding of its macroscopic properties, emphasizing also the role of the surface topography and morphology that is regular atomic steps, composition and electronic structure.

In the present thesis the many-sided investigation was performed particularly thoroughly for the $Sr_{0.8}Ca_{0.2}RuO_3$ compound on the $SrTiO_3$ substrate, providing detailed information selectively for an interface, an interior and a surface of the thin film.

3. Experimental

3.1. Sample preparation

The $Sr_{1-x}Ca_xRuO_3$ (x = 0, 0.2 and 0.4) thin films were deposited with use of the high-pressure sputtering (HPS). HPS is one of the physical vapor deposition methods in which a material of desired composition (target) is vaporized using an ionic beam and subsequently condensed in a form of a film coating on a suitable surface (substrate).

The targets were prepared from fine powders pressed in a form of a cylindrical pellet and sintered. The substrates were monocrystals of $SrTiO_3$ and $LaAlO_3$ cut in 1 mm thick rectangular pieces. The target was mounted in a holder and situated over the substrate in a deposition chamber (see figure 6). Before the deposition the chamber was evacuated to a background pressure in the range of 10^{-6} mbar and flushed with oxygen. Then the rate of oxygen flow was fixed to keep a desired ambient pressure level. A constant voltage was applied between the target and the target holder to start a plasma discharge and create a constant current of ionized oxygen gas towards the target surface. During all the adjustments and stabilization of the process the target was moved to the side of the chamber to protect the substrate surface and only then placed directly over it.

Particles of the target removed with ionic bombardment form a mixture of atoms, ions and atomic clusters falling down on the substrate surface. Adatoms arriving at the surface move to the nucleation sites and merge together. To increase their mobility the substrate is situated on a hot plate. A HPS deposition rate is slow compared to other methods, like PLD or MOCVD. A slow rate extends the time of formation of the upper layers and allows diffusion of atoms between regions of different stoichiometry but also increases the influence of re-sputtering and re-evaporation, especially at higher temperatures[91]. Intense scattering of the sputtered particles occurring thanks to the high oxygen pressure results in isotropic spreading of the elements which provides a uniform composition of the thin film. The 5 cm diameter of the target was large comparing to the 1 cm × 1 cm dimensions of the used substrates. The target-substrate distance was kept in the range of 32-48 mm to prevent the plasma from touching the substrate surface. Such geometry provided uniform thickness of the produced thin films. Target particles traveling longer distances and thermalized by multiple scattering are also less likely to cause re-sputtering from the substrate surface.

After the deposition the chamber was immediately vented with oxygen to a pressure of 800 mbar and then allowed to cool down at the rate of about 10 ºC/min.

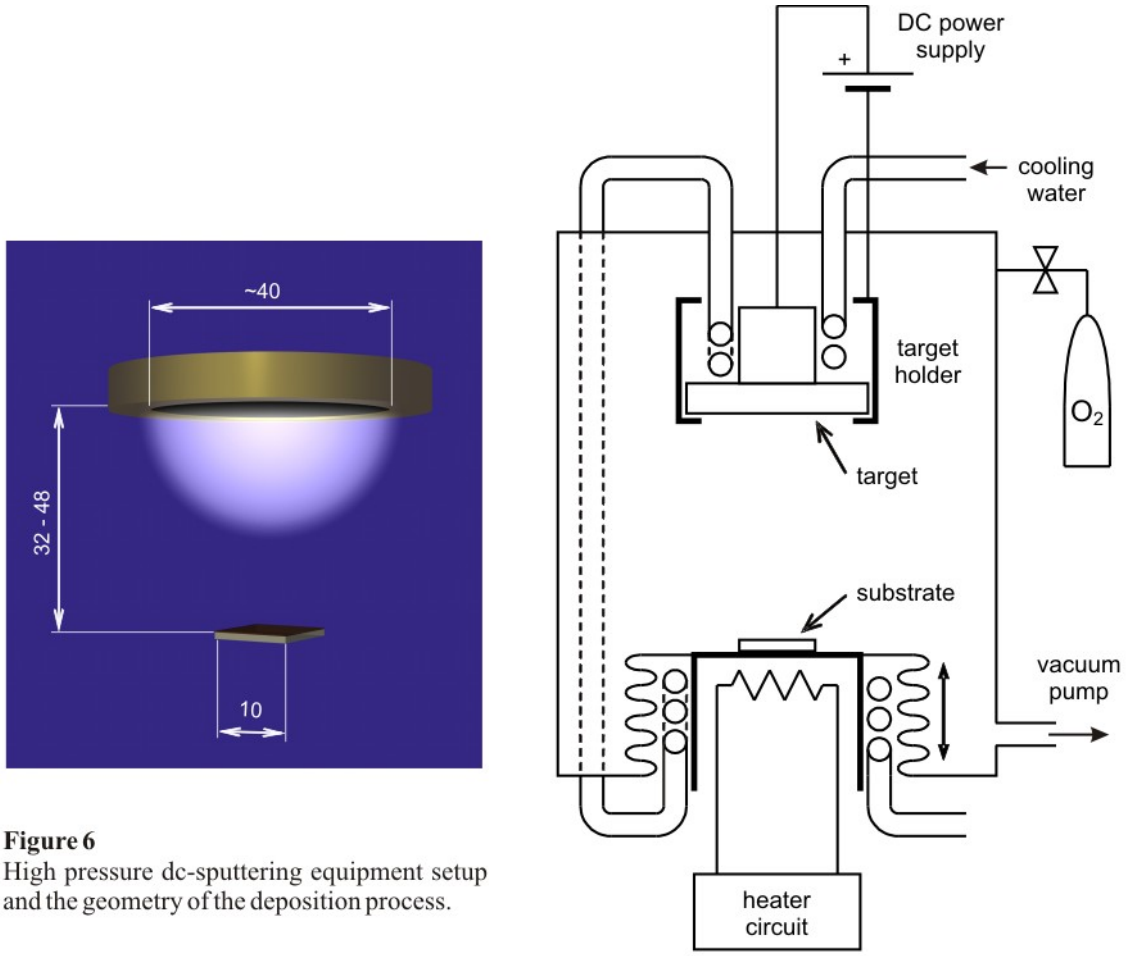

Figure 6
High pressure dc-sputtering equipment setup and the geometry of the deposition process.

Pictures of the HPS deposition chamber designed and built by Dr. Ulrich Poppe, under operation in Peter Grünberg Institute in Forschungszentrum Jülich (Germany).

The targets, obtained from a leading company, were subjected to a chemical analysis. The oxygen content was checked using infrared spectroscopy after the sample was heated in flowing helium gas in a graphite crucible. The content of Sr, Ca and Ru was determined using inductively coupled plasma with optical emission spectroscopy. The 20 mg sample was first mixed with 100 mg of KNO_3 and 800 mg of KOH and annealed for 30 min at 500 ºC and the mixture was then dissolved in water. Secondly a 3% solution of HCl was added to the mixture. The liquid sample was then introduced into argon plasma and excited. De-excitation of the sample involved an emission of characteristic radiation in the optical range. The identification of this radiation and the comparison of its intensity to the one obtained for a calibration sample permitted a quantitative analysis. The results were placed in the table 1.

Table 1
Results of the chemical analysis of the targets

Sample	Mass content [%]			
	Ca	Sr	Ru	O
$SrRuO_3$	<0.1	29.8 ±1.5	41.2 ±1.2	–
$Sr_{0.8}Ca_{0.2}RuO_3$	3.2 ±0.1	24.1 ±1.2	44.1 ±1.3	21.04 ±0.54

Calculated value of the Ru/Sr atomic ratio was 1.2 in case of the $SrRuO_3$ target and the Ru/(Sr+Ca) ratio for the $Sr_{0.8}Ca_{0.2}RuO_3$ composition was even higher. In both cases subsequent XRD analysis confirmed a presence of low intensity reflections of RuO_2 next to the full pattern of orthorhombic $Sr_{1-x}Ca_xRuO_3$ in the θ-2θ scans. Therefore it can be assumed that both targets contained about 20% excess of RuO_2. Such an excess is commonly found in commercially available targets as it is expected to compensate for the loss of volatile ruthenium oxides during deposition.

The $SrTiO_3$ and $LaAlO_3$ single crystal substrates were simply placed on a hot plate without use of any adhesive. To check the heat transfer the temperature of the substrate surface was measured with a pyrometer. The results were 100-200 ºC lower than the temperature of the heater.

The $SrRuO_3$ thin films were grown on exact (001) $SrTiO_3$ substrates (tolerance <0.5º). The substrates displayed a smooth surface with a periodic step terrace structure. No special treatment was applied to improve their quality or control termination. The temperature of the heater block was fixed at 650 ºC but a pyrometer measurement revealed that the surface temperature was about 150 ºC lower. The oxygen pressure was fixed at 3 mbar and the plasma current at 150 mA (~430 V). The deposition rate was in the range of 0.3-0.4 nm/min. The obtained samples were usually 50-60 nm thick.

The $Sr_{0.8}Ca_{0.2}RuO_3$ and $Sr_{0.6}Ca_{0.4}RuO_3$ thin films were produced using a wide range of the deposition parameters. The aim was to obtain epitaxial thin films having nearly perfect crystalline structure with a lowest possible density of defects as well as good macroscopic properties such as atomically flat surface and high conductivity, giving prospects of technological application. To achieve it the deposition process was optimized with four variable parameters i.e. substrate temperature, oxygen pressure, target-sample distance and deposition current, starting from the values optimal for the undoped $SrRuO_3$ composition. A detailed list is given in the table 2. The thickness of the $Sr_{0.8}Ca_{0.2}RuO_3$ samples varied from 8 to 43 nm, the $Sr_{0.6}Ca_{0.4}RuO_3$ thin films were about 20 nm thick.

Table 2
Deposition parameters for the $Sr_{1-x}Ca_xRuO_3$ thin films.

Thin film	$Sr_{0.8}Ca_{0.2}RuO_3$	$Sr_{0.8}Ca_{0.2}RuO_3$	$Sr_{0.6}Ca_{0.4}RuO_3$
Substrate	$SrTiO_3$ (100) exact	$LaAlO_3$ (100) exact	$SrTiO_3$ (100) exact
Temperature of the heater [ºC]	500 – 700	240 – 720	580 – 680
Oxygen pressure [mbar]	1 – 3.5	3	2.5 – 3
Substrate-target distance [mm]	32 – 48	32 – 45	36 – 44
Plasma current [mA]	25 – 140 (~400 V)	140 – 200 (~400 V)	145 – 180 (~400 V)
Deposition rate [nm/min]	0.15 (130 mA)		0.1 (180 mA)

Verification of the quality for each sample begun with an XRD based structure check and AFM surface topography imaging. Then selected samples were further investigated with RBS, TOF-SIMS and HRTEM. FWHM of a rocking curve, presence of intensity oscillations at the θ-2θ scan, a surface roughness given by rms, visibility of atomic steps at a surface and resistivity of a thin film were chosen as quality indicators.

Unfortunately, there was no clear relation between the quality of the thin film and any of the above parameters. A high deposition current and a short distance obviously increased a deposition rate but did not seem to influence the properties of a thin film. Oxygen pressure change from typical 3 mbar to 1 mbar led to a significant drop of usable current and therefore to a decrease of a deposition rate but no relevance to the properties of the thin film was confirmed.

3.2. Characterization methods

3.2.1. X-ray diffraction (XRD)

Analysis of the thin films with the use of x-ray elastic scattering involved diffraction in a typical Bragg-Brentano geometry including full θ-2θ scans and analysis of thickness dependent intensity oscillations but also rocking curve measurements, reciprocal space mapping and reflectometry.

X-ray diffraction scans are usually performed with an incident and diffracted x-ray beam laying in a plane perpendicular to a surface of a sample. An angle ω between incoming beam and a surface equals half of an angle 2θ between incoming and diffracted beam which is easy to obtain in Bragg-Brentano geometry where a detector rotates at twice the speed of a sample (so called θ-2θ scan). This configuration is thus sensitive only to the planes parallel to a surface. Typical θ-2θ scan provides information about c-lattice parameters of both a substrate and a thin film. It can be derived with the use of classical Rietveld analysis on a basis of Bragg equation,

$$2d\sin\theta = n\lambda$$

where λ is an x-ray wavelength and d – spacing between atomic planes.

Periodic intensity oscillations in the θ-2θ scans appear at the shoulders of thin film diffraction peaks as a result of reflection at a substrate-film interface. Oscillations can only be observed for the good quality crystalline thin films having uniform thickness and a clear substrate-film interface. A period of these oscillations is dependent on the thickness of a film. A thickness and an out of plane lattice constant can be calculated for samples consisting of several (>10) layers of atoms.

Rocking curve measurements give detailed information about a shape and an angular width of a selected diffraction peak. A detector is placed at a fixed 2θ angle corresponding to a substrate or a thin film peak. A sample is tilted in a range of less than 1° around θ angle. A width of the obtained rocking curve is inversely proportional to a density of defects in a material. Typical full width at half maximum (FWHM) of a (002) peak for good quality $SrRuO_3$ thin films is lower than 0.1°.

Reciprocal space mapping gives as a result a two-dimensional map of diffracted x-ray intensity as a function of position in reciprocal space. It can be carried out as a series of scans where a detector rotates at twice the speed of a sample with varying relationship between ω and 2θ. Diffracted intensity function of ω and 2θ is then converted into function of reciprocal space coordinates. In case of the substrates and the thin films both having tetragonal structure the mapping can be reduced to 2 of crystal dimensions. The range of ω and 2θ should be chosen to satisfy the Bragg law for a selected ($h0l$) substrate reflection and an adequate reflection coming from a thin film. This approach allows determine in-plane and out-of-plane lattice constants for a substrate and a film. Accuracy of the calculation of absolute values depends strongly on adjustment between geometry of a sample and a diffractometer. Relative positions of the peaks on a reciprocal plane however give much more accurate information about differences in lattice constants between substrate and a thin film and therefore their in-plane alignment.

Reflectometry is a technique using glancing incidence angles of x-ray beam to investigate properties of a sample. For x-rays all materials have indices of refraction slightly below that of a vacuum which means that at very low incident angles x-ray radiation is totally reflected from a surface of a sample. The critical angle for most materials is less than 0.3°. This phenomenon, called total external reflection, appears also at the interface between a thin film and a substrate when a thin film has a higher refractive index. Above the critical angle a reflection from the interface interferes with a reflection from the surface

and gives rise to interference fringes. From a period of the fringes a thickness of a thin film can be calculated. A measurement is a θ-2θ scan, typically in a range of θ up to 5º. The method can be used for thickness determination between 2 and 200 nm for crystalline and amorphous thin films.

Most of our data were obtained using a four-circle X'Pert Philips diffractometer with a Cu x-ray source, typically with 1 cm incident beam mask, 1/16º divergence and 1/8º anti-scatter slit. The θ-2θ scans were taken in a range of 15 to 115º with a step of 0.03º, ω-rocking curves covered less than 1º range around a peak position with a step of 0.001°. Reciprocal space mapping was conducted as a series of 5º wide ω-2θ scans, with a 0.03º step along ω axis and a 0.03º step of the offset between ω and 2θ axes. Reflectometry used a graded multilayer parabolic x-ray mirror to create a quasi-parallel incident beam and the scans covered a range of θ from 1 to 4º. Several θ-2θ diffractograms for powdered bulk samples were taken in a transmission mode with different equipment.

3.2.2. X-ray Photoelectron Spectroscopy (XPS)

XPS uses monochromatic radiation to extract information about binding energies of core electrons at the near-surface region of the specimen[92]. One of possible results of a sample surface irradiation is an emission of photoelectrons. Kinetic energy of these electrons is measured by the spectrometer working under UHV conditions. At a next step binding energy of each electron can be calculated from a simple formula:

$$E_B = h\nu - \left(E_k + W\right)$$

where E_B is the binding energy, $h\nu$ – photon energy, E_k – kinetic energy of photoelectron and W is the spectrometer work function. Photon energy, usually Al K_α or Mg K_α, is large enough to allow emission from several atomic core-levels. However, information from the sample can only be acquired up to a certain depth, determined by a distance the photoelectron can travel without being inelastically scattered. It means that 95% of the electrons come from the first few nanometers of the sample, making the method highly surface sensitive.

Our measurements were carried out *ex situ* with a Perkin–Elmer Instrument (PHI 5600), using photons of the energy 1486.6 eV from a monochromatized Al K_α radiation source, a pass energy of 11.2 eV, under the UHV condition of about 10^{-8} mbar. The energy resolution can be estimated as being about 0.3 eV.

XPS was performed for the $Sr_{1-x}Ca_xRuO_3$ (x = 0, 0.2 and 0.4) thin films deposited on $SrTiO_3$. The spectra were initially taken in the range of binding energies up to 800 eV to reveal possible contamination of the thin films. Analysis confirmed a presence of adsorbed carbonates, expected in case of *ex situ* measurements but no other contaminants were found. In the next step the energy range was limited to the regions where the photoelectrons coming from different elements of the thin film were identified, allowing their longer acquisition. The spectra were taken at two different analysis angles defined with respect to the sample surface. The higher the analysis angle the shorter the path photoelectrons travel to the surface, which indirectly increases the penetration depth and thus the results give some information about in-depth homogeneity of the sample. The angles and the covered regions were placed in the table 3.

Table 3
The list of measured XPS spectra

Thin film (on $SrTiO_3$ substrate)	Angles of analysis	XPS spectra
$SrRuO_3$	50º, 10º	Sr3*d*, O1*s*, Ru3*p*, valence band
$Sr_{0.8}Ca_{0.2}RuO_3$, $Sr_{0.6}Ca_{0.4}RuO_3$	45º, 20º	Sr3*d*, Ca2*p*, O1*s*, Ru3*p*, valence band

The valence band spectra of the as-made $Sr_{1-x}Ca_xRuO_3$ thin films, taken in the range of 0-12 eV were nearly identical, regardless of the Ca content or analysis angle. In every spectrum a steep slope between the occupied and empty electron states was observed at the Fermi level that is at a binding energy of 0 eV. Calibration of the position of all the XPS spectra was performed using the Fermi edge as a reference point (see figure 7).

For the fitting procedure the spectra measured for one sample at two different angles were initially being subtracted (see figure 8). The difference contained mostly information coming from the deeper layers of the film. It allowed first to distinguish the peaks originating from the atoms involved in the

$Sr_{1-x}Ca_xRuO_3$ thin film crystal lattice from the peaks of the surface components, that are atoms bound with physisorbates and chemisorbates at the surface, mainly with carbon oxides and hydroxyles. Large amount of adsorbed contaminations was confirmed by a presence of pronounced C1*s* lines in the XPS spectra. Subtraction removed most of the signal coming from the surface and allowed fitting lattice component single lines (O1*s*) and doublets (Sr3*d* and Ca2*p*) with much higher accuracy. For every fitted doublet the intensity ratios of 1:2 for $p_{1/2}$ and $p_{3/2}$ peaks and 2:3 for $d_{3/2}$ and $d_{5/2}$ peaks were fixed, the shapes and FWHMs of the component lines were set to be equal and the values of the spin-orbit splitting taken from the literature[93]. In the next step the original data were fitted using the shapes of the lattice components obtained from the subtraction procedure and the number of the surface components sufficient to qualitatively match the spectra. In most cases the fitting procedure revealed at least two distinct surface components in the O1*s*, Sr3*d* and Ca2*p* spectra and the relatively high FWHMs of the peaks suggest that their exact number may be higher. Only in the Sr3*d* spectrum of the $SrRuO_3$ thin film the two surface doublets could not be mathematically resolved.

The line-widths of the Ru3*p* doublet usually exceeded 4 eV, which suggested a variety of different oxidation states of Ru atoms. Thus the number of the fitted components used to effectively describe the spectra does not necessarily account for the number of different chemical surroundings of the atoms. The shape of the spectrum did not seem to change with the analysis angle therefore the subtraction procedure could not be utilized.

A depth profile analysis was performed with help of the simple model described by Cumpson and Seah[94]. In this model a near surface region of a specimen was approximated as a bilayer structure, where an overlayer of element A lays on top a substrate of element B. With an assumption that electrons follow a straight path from creation to emission (straight line approximation – SLA) an intensity I_A of electrons observed from an overlayer of thickness *d* can be written as:

$$I_A = I_A^{\infty}\left(1-\exp\left(-\frac{d}{\lambda_A(E_A)\sin\vartheta}\right)\right)$$

and the one from the substrate as:

$$I_B = I_B^{\infty}\exp\left(-\frac{d}{\lambda_A(E_B)\sin\vartheta}\right)$$

where ϑ is the angle of analysis. I_A^{∞} and I_B^{∞} are the intensities expected from a specimen of pure A and B, usually unavailable but proportional to the sensitivity factors s_A and s_B. Additionally if the compared signals originate from the same element present in both overlayer and the substrate then

$$\lambda_A(E_A) \approx \lambda_A(E_B) = \lambda$$

In the next step Cumpson and Seah defined λ as semi-empirical attenuation length rather than inelastic mean free path, to account for a number of effects neglected in the SLA model, e.g. elastic scattering. Finally the thickness of the overlayer can be calculated from the formula

$$d = \lambda \sin\vartheta \ln\left(1+\frac{I_A/s_A}{I_B/s_B}\right)$$

where *I/s* is an intensity divided by a sensitivity factor for an element A from a top layer and B from a bottom layer.

In our case the obtained values of λ, depending on the kinetic energy of the photoelectron, were 1.8, 2.0 and 2.3 nm for O1*s*, Ca2*p* and Sr3*d* states respectively. With these values it is possible to calculate which fraction of all the acquired photoelectrons is created within a certain thickness of the specimen. For example, at the angle of 50º about 50% of Sr3*d* electrons with a kinetic energy of 1486.6 – 132.1 = 1354.5 eV come from the first 5-6 sample monolayers, while there is still about 10% contribution from below 20 monolayers. At the angle of 10º the number of electrons from below 10 monolayers is negligible.

Obvious distinction between lattice and surface components observed in our XPS spectra allowed hypothesis that adsorbates affected a certain upper region of the thin film forming a uniform and fairly separated layer. Below one should expect perovskite lattice of the thin film to remain undisturbed. In such a case a bilayer model, like that of Cumpson and Seah, should allow to get a rough estimate of the thickness of this surface layer. The calculations were made independently for O1*s*, Sr3*d* and Ca2*p* spectra at both analysis angles.

Vertical axes of all XPS spectra show intensity with linear scale. Exact values are usually not presented.

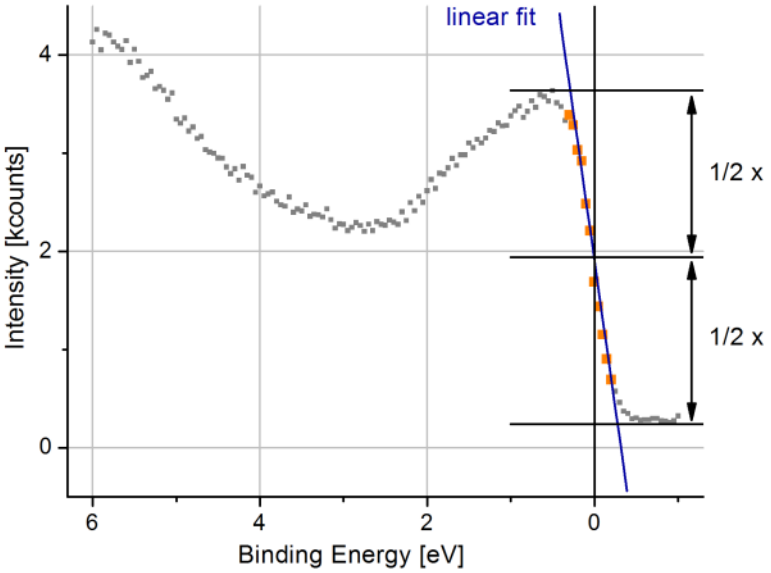

Figure 7
Illustration of a calibration procedure for XPS spectra. Example valence band spectrum of a $SrRuO_3$ thin film deposited on $SrTiO_3$, taken at two analysis angles (50° and 10°). A center of a slope between the occupied and empty electron states (orange points) was determined by finding a binding energy position at half of the height of its linear approximation (blue line). This position was then arbitrarily set to 0 eV.

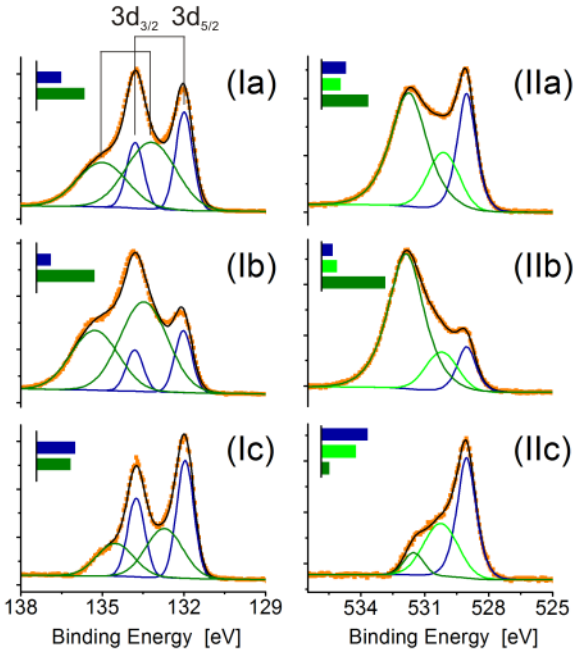

Figure 8
Illustration of a fitting procedure for XPS spectra. Example Sr3*d* (I) and O1*s* (II) core lines of a $SrRuO_3$ thin film taken at the analysis angles of 50° (a) and 10° (b), and the subtraction (a)−(b) exposing lines from the interior of the thin film (c). Usually it was possible to distinguish 2-3 separate Sr3*d* doublets, 3 Ca2*p* doublets and 3 single O1*s* lines. Small bar graphs show relative intensities of the individual components: perovskite lattice (blue) and surface compounds contribution (green).

3.2.3. Rutherford Backscattering Spectroscopy (RBS)

RBS is a direct and nondestructive method for microanalysis of materials[95]. In a thin film application it typically uses He+ ions of energy lower than 2 MeV as projectiles, which are directed towards the surface of the thin film, as a collimated beam. A projectile penetrates the target losing energy either to the electrons, by ionization and excitation of the target atoms, or during nuclear collisions. The latter can cause backscattering, thus a 180° change of direction, which can be described as a single, direct two-body collision. The energy loss during such an event can be easily described as a function of the target nucleus mass. On the other hand the amount of energy lost to the electrons ΔE is directly proportional to the penetration depth t.

$$\Delta E = S\,t$$

S is a so-called backscattering energy-loss factor, dependent on masses and stopping cross-sections of the target nuclei. Therefore energy distribution measurement of the scattered projectiles allows determination of the concentration of target atoms as a function of depth. The initial helium ion energy of 1-2 MeV provides good mass resolution and a penetration depth up to 2 μm without causing substantial radiation damage in the sample.

Characterization of single crystal thin films starts with the ion beam adjusted along one of the crystal axes. The atomic planes parallel to the beam act as potential barriers, steering the ions to the channels between them which limits the number of direct collisions. The second measurement is then taken with the crystal oriented randomly or rather in such a way that the channeling effect is suppressed. Both measurements produce different yields of backscattered ions and their minimum ratio $\chi_{\min}$ is used to describe the quality of the thin films.

Our data were collected at a Tandetron accelerator with a 1.4 MeV He+ ion beam and a scattering angle of 170°. The measurements were performed in both channeling and random mode and the minimum yield ratio calculated. Stoichiometries of our thin films were estimated with the use of RUMP software – a standard and well-described[96] tool generating theoretical RBS spectra.

3.2.4. Time-of-Flight Secondary Ion Mass Spectrometry (TOF-SIMS)

TOF-SIMS enables determination of both lateral and in-depth distribution of elements and compounds in the sample[97]. Pulsed beams of ions are used to remove and ionize species (fragments) from a target sample surface. During a measurement two beams of ions hit the target sample alternately. One (sputtering beam) is used to remove some monolayers of target atoms and another (sampling beam) to provide target ions for mass analysis. Both beams consist of low energy (keV range) ions which, hitting the target, create a so-called collision cascade of its atoms. The energy is transferred to the interior of the target and part of it back to the surface allowing surface atoms and molecular compounds to overcome their binding energy. The density of ions in the sputtering beam and the duration time of the pulse are adjusted to control the number of removed target monolayers. The sputtered area is much larger than the region of analysis. In turn, the so-called secondary ions, ejected by the sampling beam, are accelerated into a mass spectrometer, where their masses are identified by measuring the time of their flight from the target surface to the detector.

Lateral, 2-dimensional images are acquired by rastering a focused sampling beam across the sample surface. After a scan is completed, 1-3 monolayers of the sample are removed by the sputtering beam and another scan is taken. Mass analysis at each scanned point provides information about 3-dimensional distribution of compounds in the sample. Total number of ions acquired during each lateral scan gives a distribution of ions as a function of depth from the surface (a depth profile). The data acquired at the uppermost layer of the sample may be affected due to different removal rates of different species. However, such a preferential sputtering leads to a depletion of certain species reducing their flux and stabilizing the removal process of the deeper layers.

The TOF-SIMS lateral scans were performed using TOF-SIMS IV (ION-TOF, Münster, Germany) on areas from 100×100 μm^2, to 10×10 μm^2, with a resolution better than 100×100 nm^2. The depth profiles were acquired on an area of 50×50 μm^2, while the sputtered area was 250×250 μm^2. Au ion beam of 25 keV energy and density of 2-6·10^{14}/cm^2 were used for sample analysis and 1 keV Cs ion beam with a density of 3-6·10^{17}/cm^2 for a material removal.

3.2.5. High Resolution Transmission Electron Microscopy (HRTEM)

HRTEM allows studying the crystallographic structure of a sample with atomic resolution[98]. A real space image is formed for a transparent object in a system analogous to a standard 2-lens optical microscope. The object is illuminated with an electron beam instead of light thus the optical lenses are substituted with electromagnetic coils which greatly improves magnification. The beam produced and accelerated with a high electric field in an electron gun is converged on a small area of a crystalline sample. When the crystal is oriented with one of its zone axes parallel to the beam a strong diffraction occurs. To achieve assumed magnification the diffracted beams travel through a series of objective lenses. The phase contrast image is formed when diffracted electrons of different phase are allowed to pass through, thanks to a large objective aperture, and a projector lens is focused on the image plane of the objective. Interfering, each pair of beams gives rise to a set of fringes in the image. Intersecting fringes produce a pattern of dark (or bright) spots corresponding to columns of atoms.

To make the sample transparent for the electrons and minimize inelastic scattering it is polished to a thickness in the range of ten of nanometers. Cross-sectional samples can be prepared by gluing two slices of a thin film sample face to face, embedding them in an epoxy resin, cutting discs of desirable size, grinding, dimpling and polishing and subsequently argon-ion milling after being cooled by liquid nitrogen.

Images for this paper were obtained using a JEOL 4000EX electron microscope operated at 400 kV.

3.2.6. Atomic Force Microscopy (AFM)

AFM provides a 3-dimensional image of the sample surface by measuring forces (mainly van der Waals interactions) between atoms of the surface and a microscope probe[99,100]. A very sharp tip attached to the free end of a cantilever is brought close to a sample surface. Interaction between the tip and the surface leads to bending of the cantilever. A bending angle is measured with use of a laser beam reflected from a back side of the cantilever in a direction of a position sensitive photodiode. An electronic feedback loop maintains a constant tip-sample distance determined by the user using a piezoelectric drive to move the cantilever closer or further from the sample (direction z). To produce an image of the surface the tip is dragged in both directions parallel to the sample surface (x and y) and the distance set with the actuator is stored in the computer relative to the position of the tip on the x-y plane. There exist three typical modes of imaging. In the contact mode the tip-sample distance is so small that bending of the cantilever is caused by the repulsive van der Waals forces. In the non-contact mode the probe oscillates above the sample surface in the distance range where the van der Waals forces are attractive. In the tapping mode the tip is oscillating above the sample surface but at the bottom of every oscillation it is momentarily brought in contact with a surface. This allows tapping the surface of the samples, even those easily damaged in the contact mode.

The smoothness of the surface is usually described by the root mean squared (rms) roughness defined as the standard deviation of the vertical height of the actual surface from its ideal atomically smooth approximation.

Most of the images in the thesis were acquired with a commercial surface image system (SIS) set-up equipped with a Si cantilever with a nominal tip radius of 10 nm and a spring constant of 40 N/m, working in the non-contact mode.

3.2.7. Local Conductivity Atomic Force Microscopy (LC-AFM)

LC-AFM simultaneously images topography and conductivity of the sample surface. It is acquired by using a conductive cantilever and a tip and by applying a bias voltage between the sample and the cantilever. Standard limit of current detection falls in a range of a few pA.

Measurements with conductive Pt/Ir coated silicon tips were carried out employing a JEOL JSPM-4210 microscope, working in the contact mode. The scans were taken after the chamber containing the sample was evacuated to a background pressure of 10^{-5} mbar.

3.2.8. Scanning Tunneling Microscopy (STM)

STM is based on tunneling of electrons between sample surface and a sharp conductive probe tip[99]. The tip is mounted on a piezoelectric drive. Using the drive the sample and the tip are brought close to each other. When their distance is reduced to about 1 nm the electron wavefunctions in the tip overlap the electron wavefunctions in the sample surface. If the sample is conductive or semiconductive it is possible to apply a bias voltage between the sample and the probe and generate a tunneling current. The amplitude of the current exhibits an exponential decay with the distance which allows precise control of the tip-sample gap by an electronic feedback loop. Topography image is produced by moving the tip across the sample exactly as in the case of AFM. The most widely used convention is that the bias voltage is measured in reference to the virtually grounded tip. It is possible to apply both positive and negative voltage, usually within a range of 0-3 V. In the first method of imaging the tunneling current is maintained constant by moving the probe from or towards the surface. Position of the probe is then stored in the computer and displayed as a single pixel of an image. In the second method the probe-sample distance is fixed. Information about topography is therefore stored in the variations of the tunneling current.

Images in the thesis were produced with a JEOL JSPM-4500 microscope under a base pressure of $3 \cdot 10^{-10}$ mbar, using self-made, electrochemically-etched tungsten tips.

4. Results

4.1. $SrRuO_3$ on $SrTiO_3$

In the x-ray θ-2θ scans only the (00l) peaks of both the $SrTiO_3$ substrate and the $SrRuO_3$ thin film were detected (fig. 9a). An out-of-plane pseudocubic lattice constant of 3.957±0.002 Å was found using Rietveld analysis. The periodic intensity oscillations (Laue oscillations), observed at the shoulders of the $SrRuO_3$ (002) x-ray peak (fig. 9a), indicated that the interface was sharp and free of intermixing. The thickness derived from their periods was in a good agreement with RBS simulations. The out of plane lattice constant exactly fitted the Rietveld analysis. In some cases the thickness and the quality of the interface was additionally confirmed with reflectometry scans (fig. 9b).

Typical ω scans of the (002) peak (fig. 9c) show Gaussian-like rocking curves with a FWHM of 0.05-0.06º (typical FWHM of $SrTiO_3$ substrate is 0.03º).

The scan of a reciprocal space (fig. 12) in the area around the $SrTiO_3$ (103) and the $SrRuO_3$ (103) peaks shows very good in plane alignment between the substrate and the thin film. It allowed the in plane lattice constant estimation of about 3.911±0.007 Å.

At the φ scan (not shown) of $SrRuO_3$ (221) reflection, measured for 100 nm thick film, four peaks separated by 90° from each other were observed. This result, as shown before in PLD experiments[39], indicates the coexistence of two orthorhombic $SrRuO_3$ domains with [110] axis normal to the substrate and two in-plane epitaxial arrangements of $SrRuO_3$[001] || $SrTiO_3$[010] and $SrRuO_3$[001] || $SrTiO_3$[100].

All AFM scans clearly show a flat and smooth surface built of stepped terraces (fig. 11a), having similar rms roughness value typically lower than 0.2 nm on an area 8×8 μm^2 and 2×2 μm^2. Such morphology resembles a similar surface structure of the $SrTiO_3$ substrate. The steps are present at the surface even for a single crystal substrate with a very low miscut (so called exact). An average terrace width for all our samples falls in a range of 100-800 nm, with all terraces of a single sample almost equally wide. It can be attributed to a substrate miscut of 0.03-0.23º, and is indeed lower than a tolerance value (< 0.5º) given by a manufacturer.

To acquire the image data the SIS microscope uses piezoelectric actuators to swing the cantilever over the surface of the thin film rather than move it across the surface. The image is therefore affected by the scan geometry and needs quite complex background subtraction to be viewed correctly. A view direction of the processed image is normal to the surface of the sample. To get some information about the height of the steps the view direction was set along the vertical crystallographic axis z. First a computer model of the surface was created, consisting of flat terraces of equal height, given by the matrix h:

$$h(x,y) = H_{step} \cdot i(x,y) \qquad i = 0,1,2,3\ldots$$

where H_{step} is a step height, i – a number of the step and (x, y) – coordinates on the image plane. The matrix h was then tilted about x and rotated about z axis (ω and φ angles) so that a transformed matrix h_{tr} would match the orientation of the scanned surface:

$$h_{tr}(x,y) = F\left(h(x,y), \omega, \varphi\right)$$

Created model was then optimized by varying the parameters: H_{step}, ω, φ and the matrix i, to achieve the best fit to the experimental data, using the least absolute deviations method, that is minimizing the sum S:

$$S = \sum_x \sum_y \left| h_{ex}(x,y) - h_{tr}(x,y) \right|$$

where h_{ex} is a matrix of experimental data (image data). Analysis was performed on several images of four different samples. Presented example (fig. 11b) shows that the model corresponded very well to the data. A fitting error was large only at the edges of the steps (compare with an inset), which proved that the steps were indeed of equal height. Instrument resolution of approximately 0.014 nm together with designed geometry of the measurement significantly affected accuracy, but obtained values of the height of 0.31-0.42 nm were comparable with one pseudo-cubic lattice cell. There was no indication of step bunching at any of the images.

In some cases numerous bulges, about hundred nanometers in diameter and tens of nanometers high, formed additionally on the surface (fig. 10). Their number and size varied but their presence could not be attributed to any obvious changes in deposition procedure. Only samples considered free of bulges were chosen for investigation in this thesis.

Smaller scale LC-AFM and STM images (fig. 13 and 14) revealed large number of nanoparticles, of a diameter of few nanometers, covering a flat surface of every atomic step. Such structures were also observed by other authors and identified as carbohydrate contaminates[73].

The RBS measurement for a 36 nm thick film gave a minimum ratio (χ_{min}) of the backscattering yield of about 2.2 %. The stoichiometry of the films was difficult to determine because of the overlapping of the signals coming from different elements, however a simulation gave the best fit to the obtained data for a ratio Ru/Sr = 0.84 (fig. 15).

The TOF-SIMS lateral scans, performed on $SrRuO_3$ thin film areas from 100×100 μm^2, to 10×10 μm^2 did not reveal any domains of different stoichiometry (fig. 16). With a resolution of about 300×300 nm^2, the chemical composition of the thin film seemed to be laterally homogeneous. The TOF-SIMS depth profile containing integrated signal from an area of 50×50 μm^2 (fig. 17) showed changes in concentration of the elements only in the surface and the interface. Both the surface and the interface were Sr-rich and accordingly Ru content dropped in these regions, however, the composition of the surface is better described with XPS measurements due to possible chemical reactions of SrO with adsorbates. Outside of these regions the stoichiometry of the thin film was constant.

XPS spectrum of the Sr3*d* electrons was fitted with two well resolved doublets. The lattice component was pronounced and narrow (0.75 eV), while the surface component much broader (>2 eV) and shifted to higher binding energies (fig. 18). The broad surface doublet most likely consisted of at least two components lying very close to each other. Oxygen O1*s* spectra also showed a presence of lattice and surface components (fig. 18) although in this case two surface peaks were clearly distinguished. Again surface electrons had higher binding energies than those coming from the lattice and their number was much higher than that of the lattice electrons, regardless of the analysis angle. The lattice peak was 0.95 eV wide and centered at 529.1 eV whereas widths of the surface components exceeded 2 eV. Detailed results are presented in a table 4.

Ru3*p* spectrum consisted of a single, very broad and asymmetric doublet (fig. 18 shows Ru3$p_{3/2}$ line). An unexpectedly large FWHM of the Ru3$p_{3/2}$ line, above 4.5 eV is a clear indication that the surface of the as-made $SrRuO_3$ film contains Ru atoms that are not fully oxidized but have mixed valence states varying from Ru^{4+} to Ru^0 (metallic). This situation did not seem to change in the bulk of the film because hardly any change in the spectra measured at different analysis angles was observed.

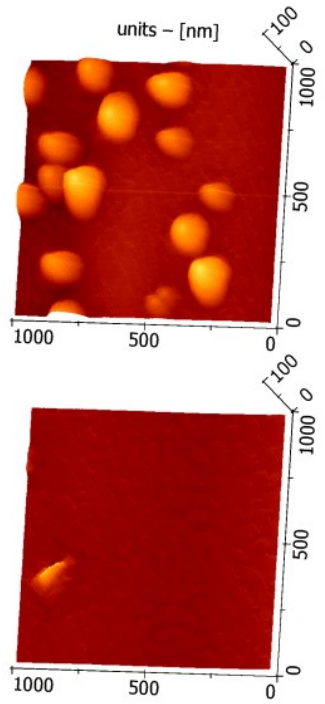

Figure 10
AFM topography images of $SrRuO_3$ thin films on $SrTiO_3$, showing different types of growth.

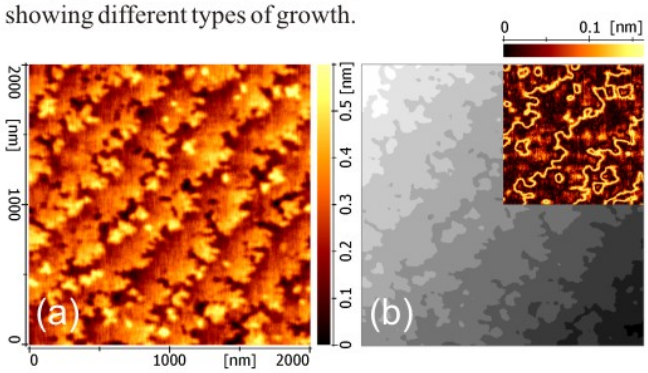

Figure 11
AFM topography image of an epitaxial $SrRuO_3$ thin film grown on $SrTiO_3$ by a step-flow mode (a) and a model of the surface, based on experimental data, built of flat steps of equal height (b). An inset shows a difference between the data and the model.

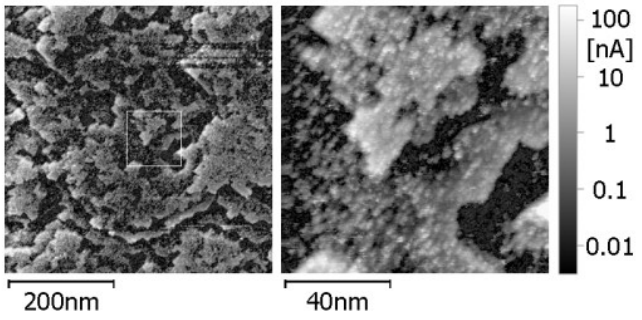

Figure 13
LC-AFM scan of a $SrRuO_3$ thin film on $SrTiO_3$ (log current). To show details of surface conductivity map a marked selection of a larger area scan (left) is shown on the right.

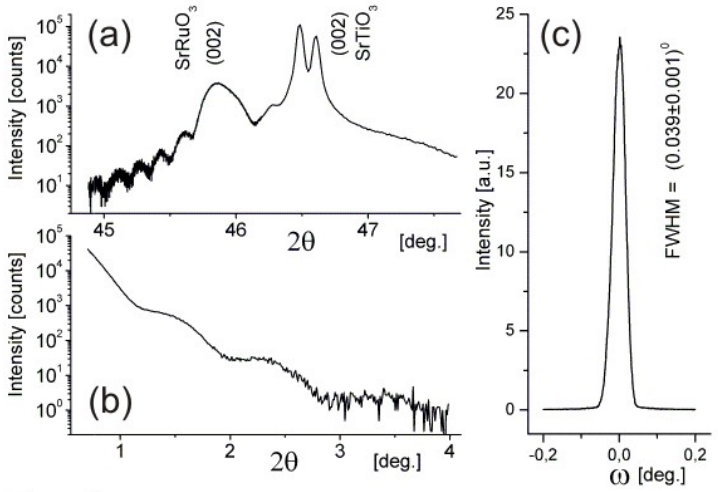

Figure 9
X-ray θ-2θ scan (a) and ω-rocking curve (c) of (002) peak and reflectometry scan (b), for $SrRuO_3$ thin film epitaxially grown on $SrTiO_3$.

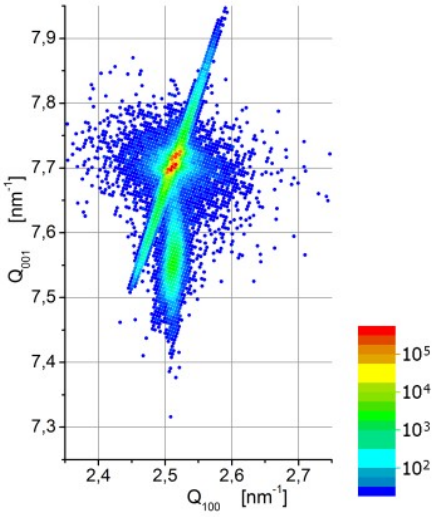

Figure 12
XRD reciprocal space maps measured around the (103) $SrTiO_3$ peak for an epitaxial $SrRuO_3$ thin film.

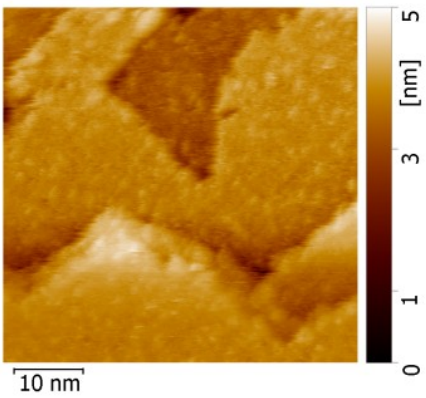

Figure 14
Small area STM image of a $SrRuO_3$ thin film on $SrTiO_3$.

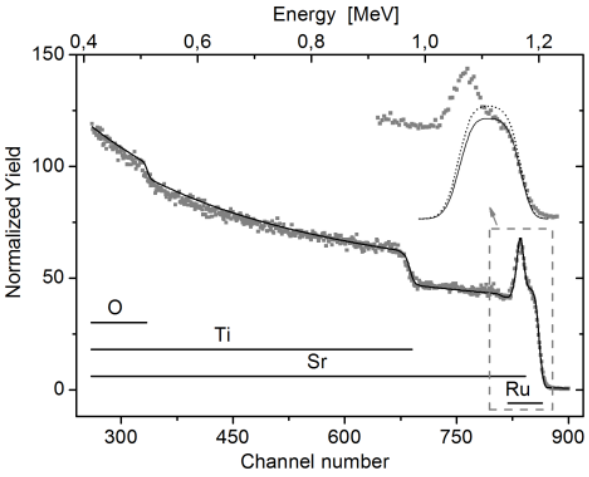

Figure 15
RBS spectum (points) and simulation (line) obtained for a 36 nm thick $SrRuO_3$ film deposited on $SrTiO_3$. A thin film region is enlarged in an inset. The simulations are presented for Ru/Sr ratios of 0.84 (solid) and 1 (dots) for comparison.

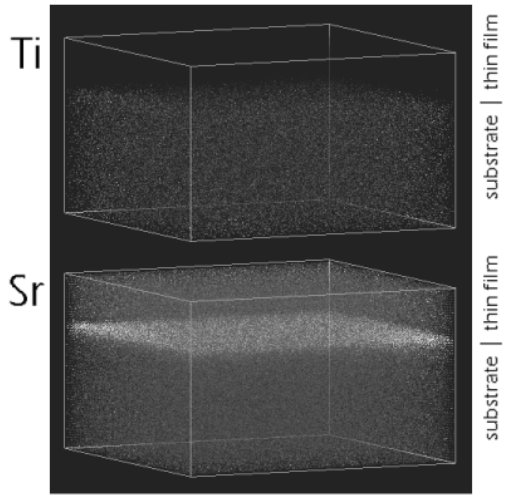

Figure 16
ToF SIMS three-dimensional (3D) spectrum of the $SrRuO_3$ thin film deposited on $SrTiO_3$, acquired on 20×20 μm^2 area.

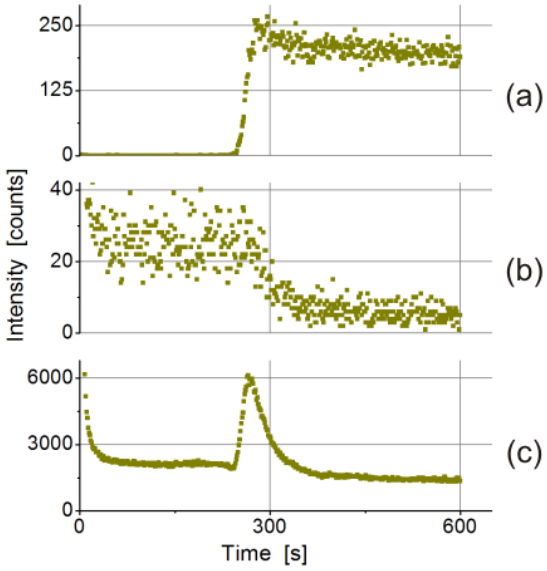

Figure 17
ToF SIMS depth profile data of the $SrRuO_3$ thin film deposited on $SrTiO_3$ integrated over 50×50 μm^2 area. Signals are presented for Ti (a), Ru (b) and Sr (c).

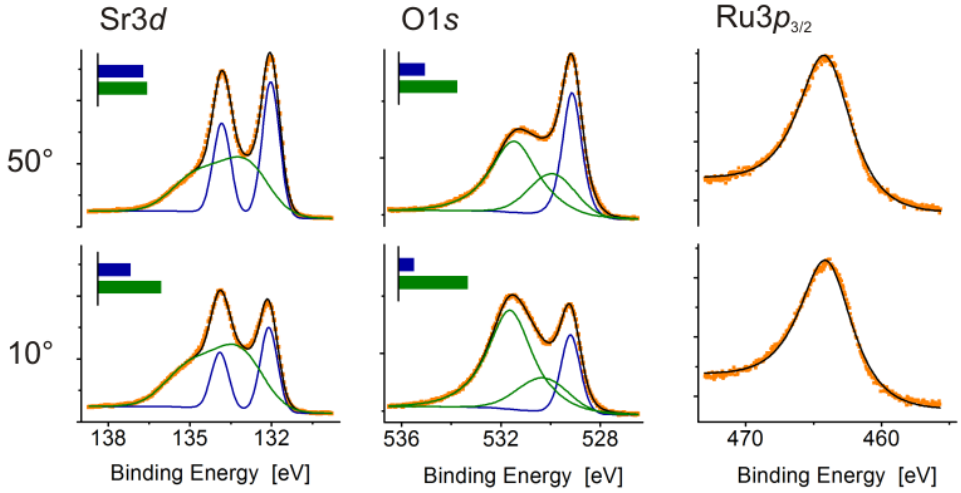

Figure 18
XPS core spectra for a $SrRuO_3$ thin film deposited on $SrTiO_3$, taken at two analysis angles (50° and 10°). Individual lines or doublets fitted to the spectra are presented and perovskite lattice contribution (blue) distinguished from the one coming from surface compounds (green) wherever possible. Small bar graphs show relative intensities of the lattice- and surface-originating components.

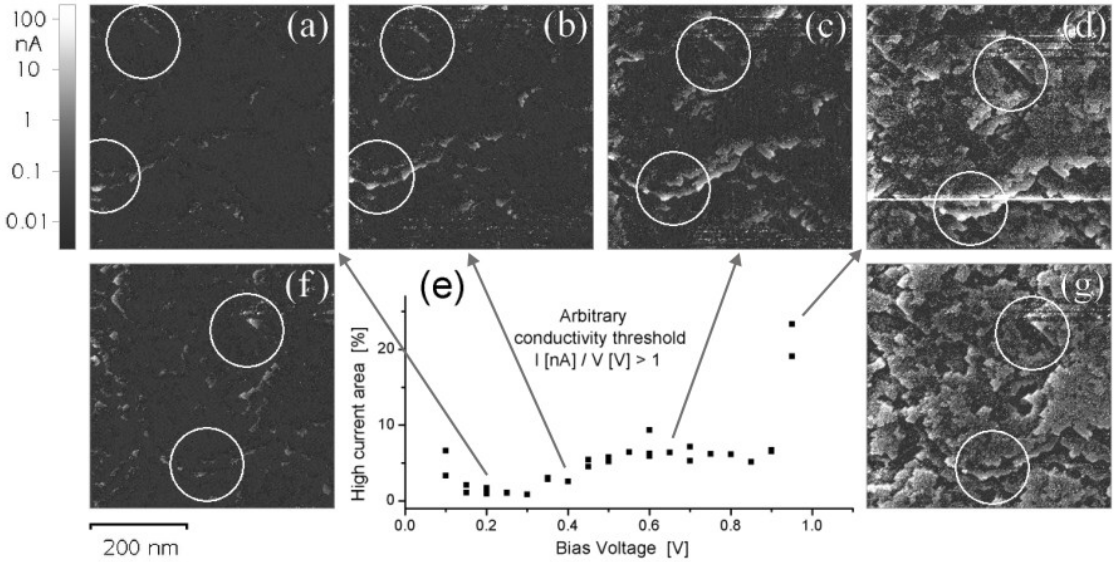

Figure 19
LC-AFM current images (log scale) taken at increasing bias voltage of 0.3 V (a), 0.4 V (b), 0.6 V (c) and 0.95 V (d) for a $SrRuO_3$ thin film on $SrTiO_3$. Two features are marked with white circles. The graph (e) shows the area of high conductivity (defined as exceeding arbitrary defined threshold). Images taken at 0.2 V (f) and 0.95 V (g) show surface changes after about 30 scans.

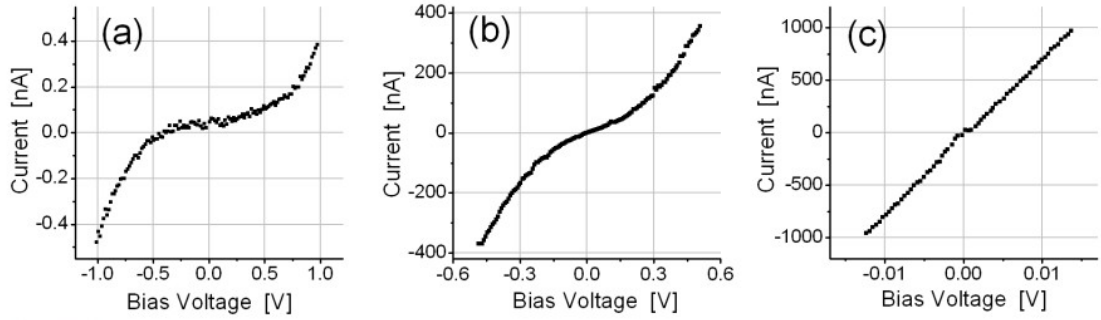

Figure 20
Typical I-V characteristics measured with LC-AFM taken at a low conductivity region (a) and two different types of high conductivity regions (b and c) for a $SrRuO_3$ thin film on $SrTiO_3$.

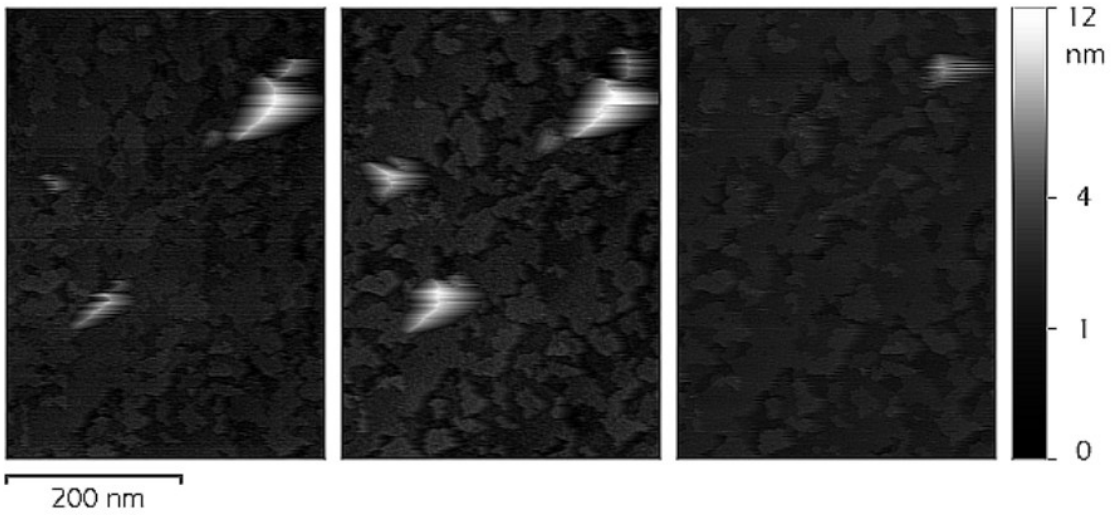

Figure 21
A sequence of STM images, taken at a bias voltage of 30 mV (grounded tip), revealing concentrated groups of adsorbates on the surface of a $SrRuO_3$ thin film on $SrTiO_3$.

Table 4
Positions, half widths and relative intensities of lattice and surface components inferred from the experimental XPS spectra for the as-made $SrRuO_3$ thin film.

		Center	Half-width	%mol	
				50°	10°
O1*s*	Line 1	529.1 eV	0.95 eV	20%	12%
	Line 2	530.1 eV	2.30 eV	45%	54%
	Line 3	531.6 eV	2.25 eV		
Sr $3d_{5/2}$ ($3d_{3/2}$) Δ = 1.8 eV	Doublet 1	132.1 eV	0.75 eV	10%	7%
	Doublet 2	133.1 eV	2.10 eV	11%	14%
Ru $3p_{3/2}$	Line	464.1 eV	4.55 eV	14%	13%

The thickness of the surface layer was calculated using the Cumpson and Seah bilayer model, independently for Sr3*d* and O1*s* spectra and at both analysis angles. The values 1.5 and 1.2 nm obtained at higher angle were both about 3 times larger than lower angle values of 0.5 and 0.4 nm. Therefore much more of lattice component signal was present when measured at 10º than expected from measurements at 50º. This suggests that the surface component does not actually form a separate uniform overlayer.

The valence band spectrum consisted of two main features, one beginning with a steep slope at the Fermi level and centered at binding energy of about 0.8 eV and another one centered at about 6.4 eV. Subtraction of the spectra, taken at analysis angles of 50º and 10º revealed another feature centered at about 3.4 eV (p. 67, fig. 58).

Macroscopically the films showed classical metallic behavior[101] in the temperature range 80-650 K (p. 67, fig. 59a), with a room temperature resistivity, measured using the van der Pauw technique[102], of about 340 μΩ·cm, and a slight kink at 153-158 K corresponding to the magnetic phase transition.

Detailed LC-AFM and STM measurements were performed to investigate changes of the $SrRuO_3$ thin film surface topography and morphology produced by low energy electron bombardment.

The LC-AFM scans were taken with a bias voltage varying from 0.1 to 0.95 V, with the steps of 0.05 V, at the scanned area of 500×500 nm^2. Regardless of the applied bias voltage observed surface always consisted of areas of different conductivity. At low voltages, up to 0.3V, most of the surface remained very low conductive (fig. 19a) and no topography details could be distinguished, except few features of very good conductivity. With increasing voltage more of the surface were becoming high conductive and this process seemed to obey certain threshold voltages. Clearly at the bias voltages of 0.4 V and 0.95 V rapid changes in the ratio between low and high conductivity area were observed, as shown in the figures 19b-19d.

To estimate these changes quantitatively, arbitrary resistance value, dividing highly conductive and low conductive areas, was taken at I/U = 1 [nA/V]. The results of calculation are presented in the figure 19e. After about 30 scans the bias voltage was decreased and again most of the surface became low conductive, according to the previously described voltage thresholds (fig. 19f and 19g) although some changes were noticeable in the areas of high conductivity. To show these changes two features were marked by circles in the figure19. Highly conductive areas were usually the edges of the steps of atomic layers, probably due to the smallest quantity of the surface contaminations. The lower marked feature was clearly such an edge. After several scans it became much less perceptible, which may be an indication of a partial decomposition. At the same time the upper feature became much more pronounced.

Several I-V curves, taken at high and low conductivity areas, showed its completely different character (fig. 20). Typical curves revealed a tunneling character of the charge transport (fig. 20a and 20b), although conductivity varied up to 10^3 times between different regions. Occasionally, after several scans with a bias voltage of about 1 V, metallic characteristics could be obtained (fig. 20c). The highest and lowest measured conductivity differed about 10^5 times.

The STM scans, taken in the constant current mode, showed the surface conductive at the whole area, regardless of an applied bias voltage or a fixed tunneling current, in the ranges of 0.005-1 V and 0.015-5 nA respectively. Results of measurements in air were similar to those obtained under UHV conditions. Using a bias voltage of 30 mV (grounded tip) and a tunneling current of 80 pA on a scanned area of 1×1 μm^2, under low vacuum conditions, a sequence of pictures was obtained, as shown in the figure 21.

Several 20-100 nm long structures were discovered on a flat surface with visible atomic steps. The material was easily formed below the tip during tunneling. Some parts became larger or smaller and finally disappeared during the process of scanning, indicating a possible mass transport or decomposition. After every transfer above the feature the tip was leaving a trace, tens of nanometers long, recorded on the picture. It meant the structure of this material was rather fragile. The height of about 10 nm excluded possibility that observed features consisted of an adsorbed water monolayer. Most likely some SrO-H_2O compounds were detected.

4.2. $Sr_{0.8}Ca_{0.2}RuO_3$ on $LaAlO_3$

For $Sr_{0.8}Ca_{0.2}RuO_3$ samples deposited on $LaAlO_3$, x-ray θ-2θ scans taken in the 2θ range of 15-115° showed, next to $LaAlO_3$ substrate peaks, only the (00*l*) thin film peaks. Thin film peaks had low intensities and the (003) peak was missing. Figure 23 shows changes in the $Sr_{0.8}Ca_{0.2}RuO_3$ (002) peak position and shape with the deposition temperature. A thin film deposited in 320 °C had the out-of-plane pseudo-cubic lattice constant of 3.965 Å. FWHM of a rocking curve was about 0.2° (fig. 24). Deposition in 625 °C gave the out-of-plane lattice constant of 3.942 Å and much broader rocking curve. Thin films deposited between 450 and 600 °C seemed to consist of at least two phases, as indicated by a splitting of the peaks appearing at every scan.

AFM pictures showed a surface morphology consisting of adjoining column-like grains (fig. 22). All columns were similar in size but their diameter grew with the deposition temperature. At 320 °C the average diameter was about 20 nm. In samples deposited above 600 °C their shapes became more irregular and the average diameter changed to about 150 nm.

The samples were macroscopically nonconductive, regardless of their deposition temperature.

Inability to produce a homogeneous thin film was a reason to abandon $LaAlO_3$ and focus on the better structurally matching $SrTiO_3$ substrate.

4.3. $Sr_{0.8}Ca_{0.2}RuO_3$ on $SrTiO_3$

In the x-ray θ-2θ scans of $Sr_{0.8}Ca_{0.2}RuO_3$ thin films deposited on $SrTiO_3$ for every $SrTiO_3$ substrate (00*l*) peak a corresponding thin film peak was detected (fig. 25a). There was no trace of peaks coming from other lattice planes or other RP phases. Intensities of thin film peaks were quite high, while their shapes and positions varied.

In the whole range of deposition parameters (see table 2) rocking curves consisted of at most two distinct components: a narrow and a very broad one (fig. 25b – gray). For more than half of all the thin films produced, a narrow part was dominant, making a broad one negligible (fig. 25b – black). FWHMs of the narrow rocking curves were lower than 0.045°. For clarity of the thesis the thin films were arbitrarily divided in two groups. If the broad component had any important contribution to the intensity of the rocking curve the sample was included in a first group. The second group consisted of the samples with only one, narrow peak.

Further investigations, using reciprocal space mapping, showed very poor in-plane alignment of the samples from the first group, whereas the thin films of the second type perfectly matched the square in-plane lattice of the substrate (fig. 27). Moreover, the second type thin films were flat and had sharp interfaces, which led to a formation of periodic intensity oscillations at the shoulders of the $Sr_{0.8}Ca_{0.2}RuO_3$ x-ray peaks (fig. 25a). From a period of these oscillations a thickness of each sample was derived with use of the Laue equation. Oscillations were also observed in reflectometry scans (fig. 25c), giving similar thickness values.

An out-of-plane pseudo-cubic lattice constant was found using Rietveld analysis and independently obtained from thickness calculations. Figure 29 shows its dependence on the deposition temperature. For the second type thin films the out-of-plane lattice constant increased continuously with the temperature. In-plane lattice constant estimation, with the use of reciprocal space mapping around the (103) $SrTiO_3$ peak, gave the value of 3.909 Å, thus slightly higher than that of $SrTiO_3$ (3.906 Å).

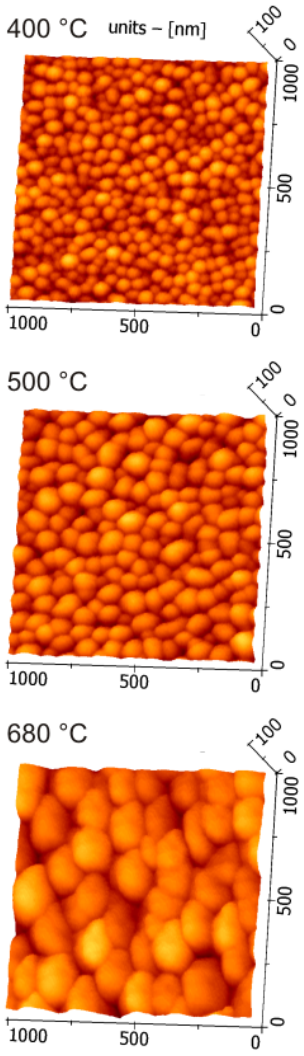

Figure 22
AFM topography scans for $Sr_{0.8}Ca_{0.2}RuO_3$ thin films, deposited on $LaAlO_3$.

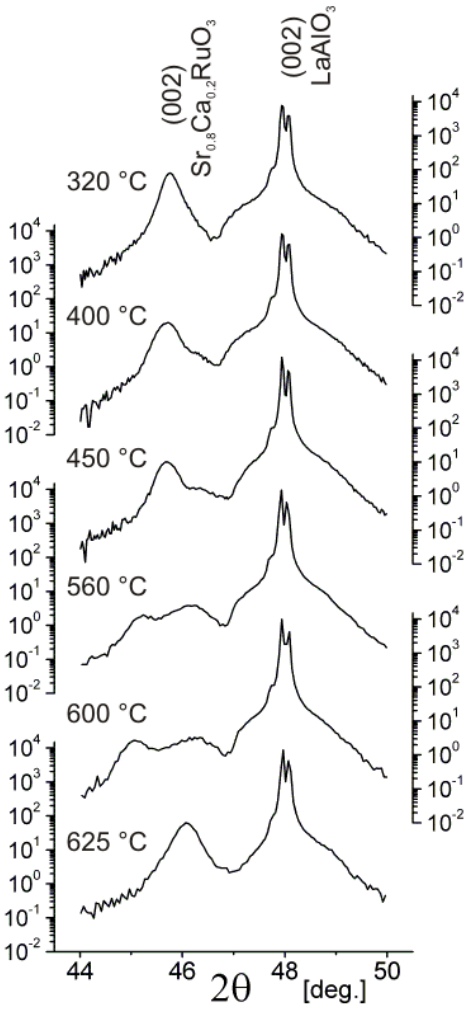

Figure 23
X-ray θ-2θ scans showing (002) peak evolution with deposition temperature for $Sr_{0.8}Ca_{0.2}RuO_3$ thin films deposited on $LaAlO_3$.

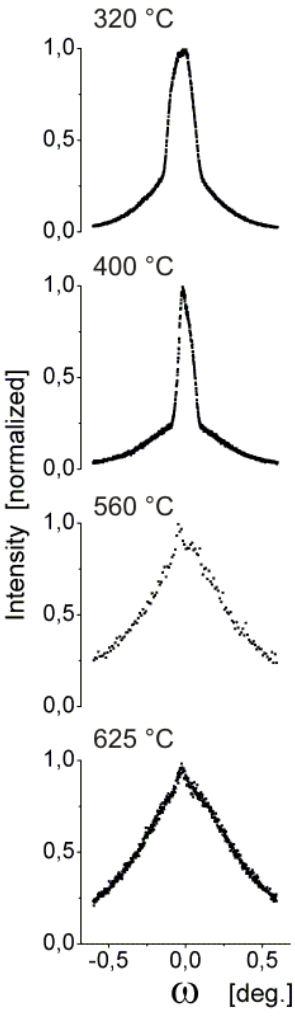

Figure 24
X-ray ω–rocking curves of (002) peaks for $Sr_{0.8}Ca_{0.2}RuO_3$ thin films deposited on $LaAlO_3$.

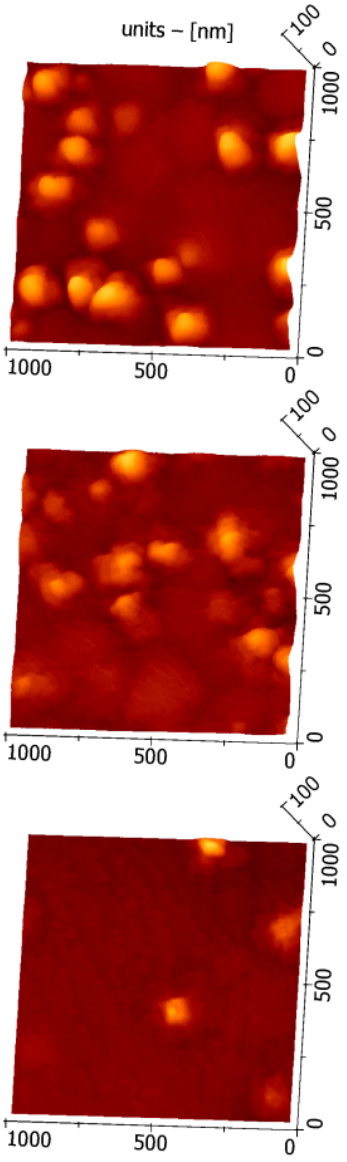

Figure 26
AFM topography images for $Sr_{0.8}Ca_{0.2}RuO_3$ thin films deposited on $SrTiO_3$ at 655–675 °C, showing undesirable type of growth.

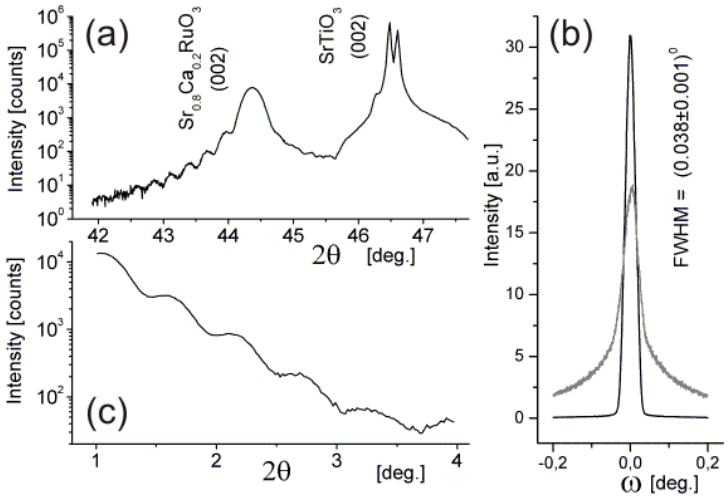

Figure 25
X-ray θ-2θ scan (a) and ω-rocking curve (b) of (002) peak and reflectometry scan (c), for a well alligned $Sr_{0.8}Ca_{0.2}RuO_3$ thin film on $SrTiO_3$ (black lines). A rocking curve of a poorly aligned thin film is shown for comparison (gray).

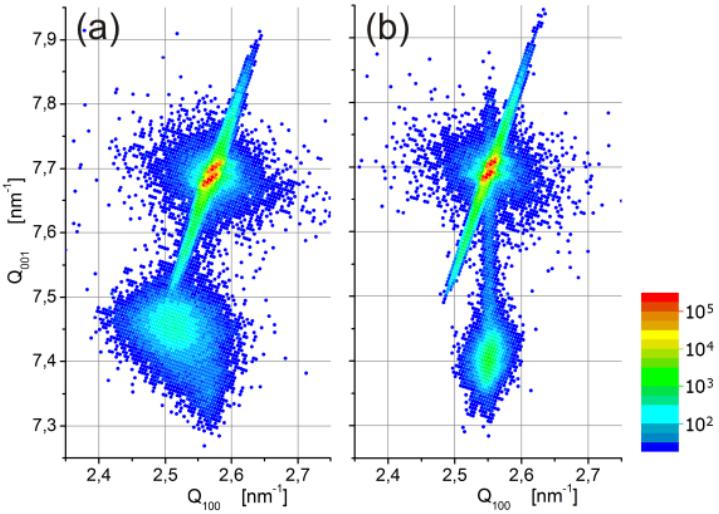

Figure 27
XRD reciprocal space maps measured around the (103) $SrTiO_3$ peak for $Sr_{0.8}Ca_{0.2}RuO_3$ thin films. Both, poorly (a) and well aligned (b) types of thin films are presented.

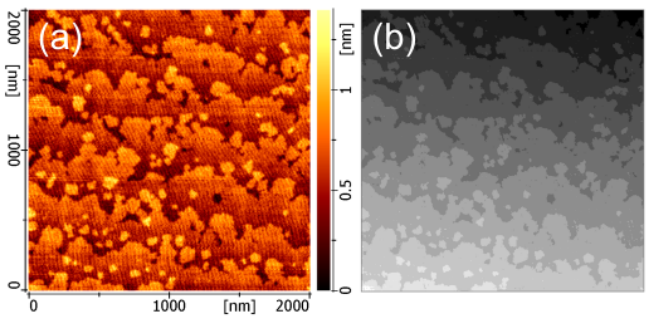

Figure 28
AFM topography image of a $Sr_{0.8}Ca_{0.2}RuO_3$ thin film grown on $SrTiO_3$ by a step-flow mode (a) and a model of the surface, based on experimental data, built of flat steps of equal height (b).

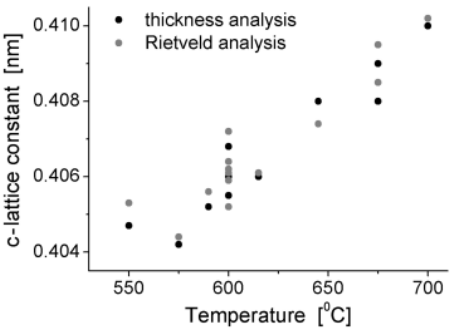

Figure 29
Out-of-plane lattice constant as a function of deposition temperature for $Sr_{0.8}Ca_{0.2}RuO_3$ thin films on $SrTiO_3$.

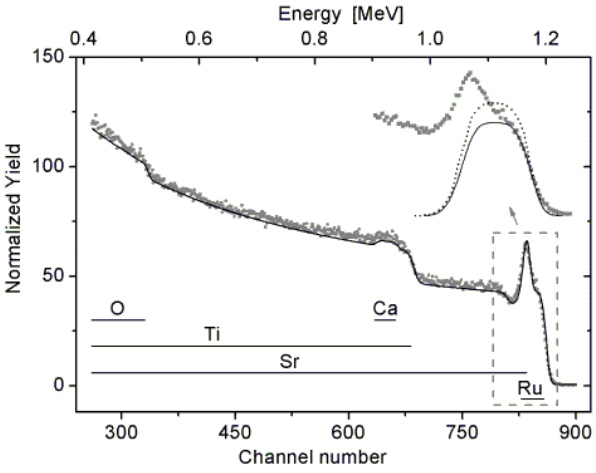

Figure 30
RBS spectum (points) and simulation (line) obtained for a 40 nm thick $Sr_{0.8}Ca_{0.2}RuO_3$ film deposited on $SrTiO_3$. A thin film region is enlarged in an inset. The simulations are presented for Ru/(Sr+Ca) ratios of 0.7 (solid) and 1 (dots) for comparison.

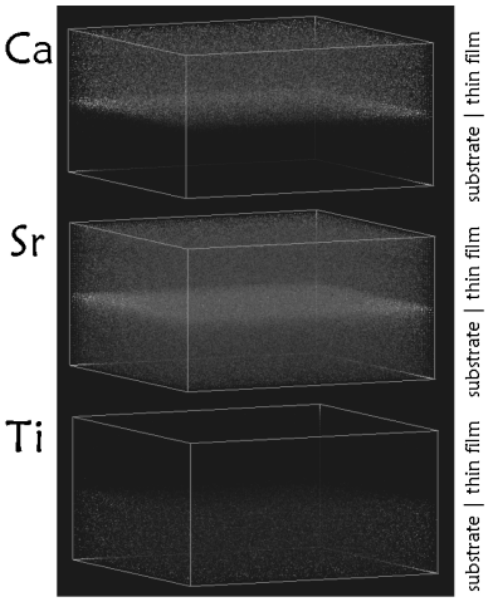

Figure 31
ToF SIMS 3D spectrum of the $Sr_{0.8}Ca_{0.2}RuO_3$ thin film deposited on $SrTiO_3$ acquired on 20×20 μm^2 area.

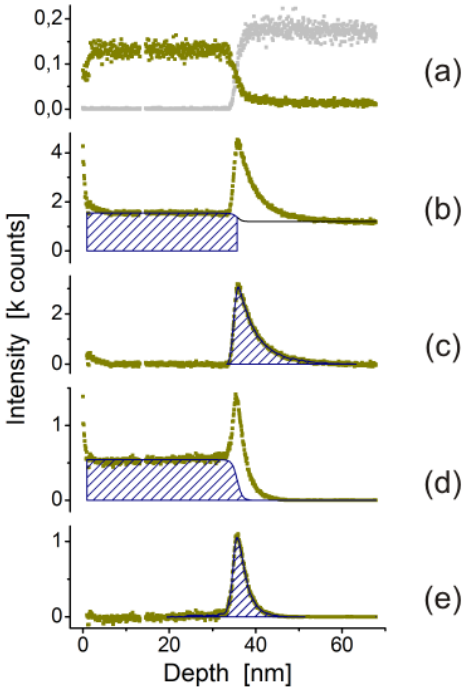

Figure 32
ToF SIMS depth profile data of the $Sr_{0.8}Ca_{0.2}RuO_3$ thin film deposited on $SrTiO_3$ integrated over 50×50 μm^2 area. Signals are presented for Ru (a – color), Ti (a – gray), Sr (b) and Ca (d). The extracted Sr and Ca excess coming from the interface is shown at (c) and (e) respectively.

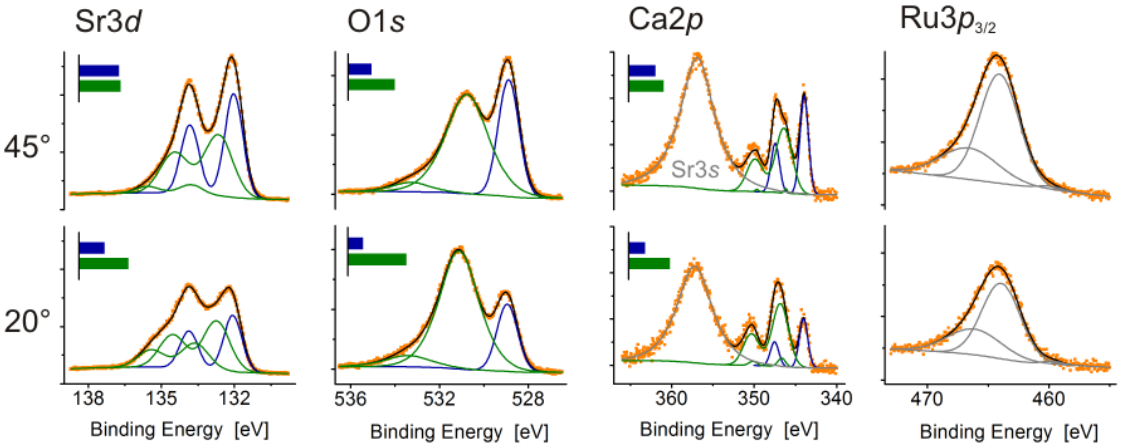

Figure 33
XPS core spectra for a $Sr_{0.8}Ca_{0.2}RuO_3$ thin film deposited on $SrTiO_3$, taken at two analysis angles (45° and 20°). Individual lines or doublets fitted to the spectra are presented and perovskite lattice contribution (blue) distinguished from the one coming from surface compounds (green) wherever possible. Small bar graphs show relative intensities of the lattice- and surface-originating components.

As in case of the $SrRuO_3$ a typical AFM image of a fresh $Sr_{0.8}Ca_{0.2}RuO_3$ thin film (fig. 28) showed a very smooth surface reflecting substrate steps. Both layer-by-layer and step-flow growth occurred concurrently with every layer having one pseudo-cubic lattice cell height, which was confirmed by a created theoretical model of the surface. No step bunching was observed.

Another similarity to the $SrRuO_3$ thin films was a formation of bulges on the surface (fig. 26). Again, their number and size varied and several samples, checked on the areas as large as 10×10 μm^2, were completely free of them. The 3D forms appeared in the whole range of deposition parameters but no obvious relation was found either to the substrate temperature, oxygen pressure, substrate-target distance or plasma current. In many cases AFM scans showed that the bulges seemed to maintain the stepped structure of the flat surface.

It was observed that the samples with a large number of bulges were the ones from the first group, with pronounced broad components in the rocking curves. The second type rocking curves usually concurred with AFM scans where the bulges were not detected. The latter type of the thin film was characterized with the rms roughness value lower than 0.3 nm on an area 4×4 μm^2 and 2×2 μm^2.

Among the 25 deposited thin films about half was qualified to the second group. The XRD as well as AFM analysis pointed out several parameters making these samples more desirable for both basic studies and technological applications. Whole characterization done to this point indicated their high quality. Therefore only these samples were selected for a further examination with RBS, TOF-SIMS and XPS.

The RBS measurements gave a minimum ratio (χ_{min}) of the backscattering yield (aligned to random) below 5%. The closest match between the obtained data and the simulations was found for a Ru/(Sr+Ca) ratio of 0.7 and even slightly lower for the samples deposited above 650 °C (fig. 30). The content of oxygen also decreased with the increasing deposition temperature. The Sr/Ca ratio remained the same as in the target (see table 5).

Table 5
Composition of the $Sr_{0.8}Ca_{0.2}RuO_3$ thin films inferred from RBS spectra.

Deposition temperature [°C]	Thickness of the thin film [nm]	Yield ratio χ_{min} [%]	Molar ratio			
			Sr	Ca	Ru	O
590	40	4.7	0.8	0.2	0.70	2.55
675	35	3.5	0.8	0.2	0.65	2.35

The results of the TOF-SIMS analysis were similar to those obtained for the $SrRuO_3$ thin film. The lateral scans (fig. 31) were performed on $Sr_{0.8}Ca_{0.2}RuO_3$ thin film areas from 100×100 μm^2 to 10×10 μm^2, with a resolution down to about 300×300 nm^2. Although no local variations of stoichiometry were found, the whole interface region showed uniform rise of Sr and Ca content. The TOF-SIMS depth profile (fig. 32) on an area of 50×50 μm^2 confirmed Sr and Ca concentration increase at the interface and revealed similar Sr- and Ca-enrichment at the surface of the thin film. Expectedly, in both regions Ru content dropped. As in case of the $SrRuO_3$ thin film it indicates incorporation of additional (Sr,Ca)O layers in the standard (Sr,Ca)O-RuO_2 structure and occurrence of RP phases. Outside of the interface and the surface region concentration of all the elements was constant.

The quantity of Sr and Ca excess in the interface was estimated using the depth profile. Original spectra showed the number of individual ions as a function of the exposure time. Clear slopes of the Ru and Ti signals (fig. 32a) allowed the distinction of the surface and the interface regions and a calculation of the time of the thin film removal. Given that the thickness was obtained in the XRD measurement it was possible to estimate a removal rate and to present the depth profile as a function of sample depth coordinate. The constant part of each, the Sr and Ca, signal (fig. 32b and 32d) was then fitted with a step-like function (Heaviside-type) and subtracted. The remaining part was assigned to the element excess (fig. 32c and 32e). The area of the excess part was then compared to the uniform part of the spectrum. Assuming that beyond the interface the thin film was stoichiometric the obtained value of global Ru/(Sr+Ca) molar ratio was 0.79 ± 0.04.

The assumption that the removal rate was constant, although not strictly correct, may nevertheless have been used for a rough estimation of an interface width. The value of 3 nm was inferred from the width of the Ca excess part.

XPS spectra of several $Sr_{0.8}Ca_{0.2}RuO_3$ thin films showed similar main features. A detailed description presented below refers to the sample measured ½ hour after deposition. The results were stored in the table 6. In all the core spectra, except for Ru3*p* line, lattice and surface components were easily distinguished. The lattice component of O1*s* signal consisted of a single line and in case of Sr3*d* and Ca2*p* of single doublets, all very narrow, with a peak width in the range of 0.9-1.2 eV (fig. 33). Normalized (relative to the total intensity of the whole spectrum) intensities of the lattice components measured at the angle of 45º, were much higher than measured at the angle of 20º.

The surface component photoelectrons had higher binding energies and their number exceeded the number of electrons coming from the perovskite lattice even when the fresh sample was measured at the angle of 45°. A complex character of the surface components was clearly visible in the O1*s*, Sr3*d* and Ca2*p* spectra (fig. 33). A very good fitting accuracy was obtained with 2 lines and 2 doublets respectively but an exact number of different chemical states of the atoms could not be resolved. The widths of the Sr3*d* lines were in the range of 1.2-1.4 eV while in case of O1*s* and Ca2*p* lines exceeded 2 eV and therefore were much wider than those of lattice component. The main surface component O1*s* line of the fresh sample was centered at a binding energy of 530.9 eV (fig. 33).

The Ru3*p* spectrum was shaped as a single broad line regardless of the angle of analysis (fig. 33). Its width, larger than 4 eV, indicated several different chemical surroundings of Ru atoms or a mixed valence state. At the angle of 20° the Ru3*p* lines had much lower relative intensity than at the angle of 45°.

Table 6

Positions, half widths and relative intensities of lattice and surface components inferred from the experimental XPS spectra for the $Sr_{0.8}Ca_{0.2}RuO_3$ thin film measured ½ hour after deposition.

		Center	Half-width	%mol	
				45°	20°
O1*s*	Line 1	528.9 eV	1.1 eV	22.0 %	14.2 %
	Line 2	530.9 eV	2.3 eV	43.8 %	55.4 %
	Line 3	533.3 eV	2.3 eV		
Sr $3d_{5/2}$ ($3d_{3/2}$) Δ = 1.8 eV	Doublet 1	132.0 eV	0.9 eV	9.7 %	6.2 %
	Doublet 2	132.7 eV	1.3 eV	10.1 %	12.0 %
	Doublet 3	133.7 eV	1.2 eV		
Ca $2p_{3/2}$ ($2p_{1/2}$) Δ = 3.5 eV	Doublet 1	344.0 eV	1.2 eV	1.3 %	0.8 %
	Doublet 2	346.4 eV	0.8 eV	1.7 %	2.0 %
	Doublet 3	346.6 eV	2.3 eV		
Ru $3p_{3/2}$	Line	464.7 eV	4.3 eV	11.5 %	9.4 %

Estimation of the thickness of the surface layer was based on O1*s*, Ca2*p* and Sr3*d* intensities. All six values obtained separately for each element and for both analysis angles, fell in the range of 0.8-1.3 nm, giving the average value of 1.0 ±0.2 nm.

The valence band spectra showed two main features similar to those observed for the $SrRuO_3$ thin film, one centered at about 1.1 eV and the other at about 5.9 eV. The slope at the Fermi level clearly indicated metallic character of atomic bonds (p. 67, fig. 60).

HRTEM cross-sectional image of the $Sr_{0.8}Ca_{0.2}RuO_3$ thin film on $SrTiO_3$ covered an area of 135×30 nm^2 (a fragment shown in the figure 34). The substrate structure part was virtually flawless, with perfect periodicity, no visible defects and comparable brightness of neighboring centers. The thin film image was much less uniform. Despite that, for most of its area expected periodic arrangement of centers could be distinguished. Irregularities mostly covered the interface region. They resembled defects of stacking fault character and clearly had different out-of-plane periodicity. This disturbance extended to about 1 nm and above that region the thin film regained its nearly-cubic regularity.

To investigate variations of the lattice constants the image was divided into 4.5 nm squares, overlapping by 75 %. For every square a two-dimensional Fourier transform was performed and the most pronounced frequency peak identified wherever possible. On this basis the in-plane (fig. 35a) and out-of-plane (fig. 35b) lattice constants were calculated locally. The in-plane spacing was similar for both the substrate and the thin film and did not seem to change with the depth, although the results were not accurate enough to resolve little differences. The out-of-plane atomic distance changed abruptly when crossing the interface. On the whole analyzed area of the thin film it was quite uniform and much larger than for the substrate. The thin film seemed therefore to be fully strained and in all its volume had an elongated out-of-plane lattice constant.

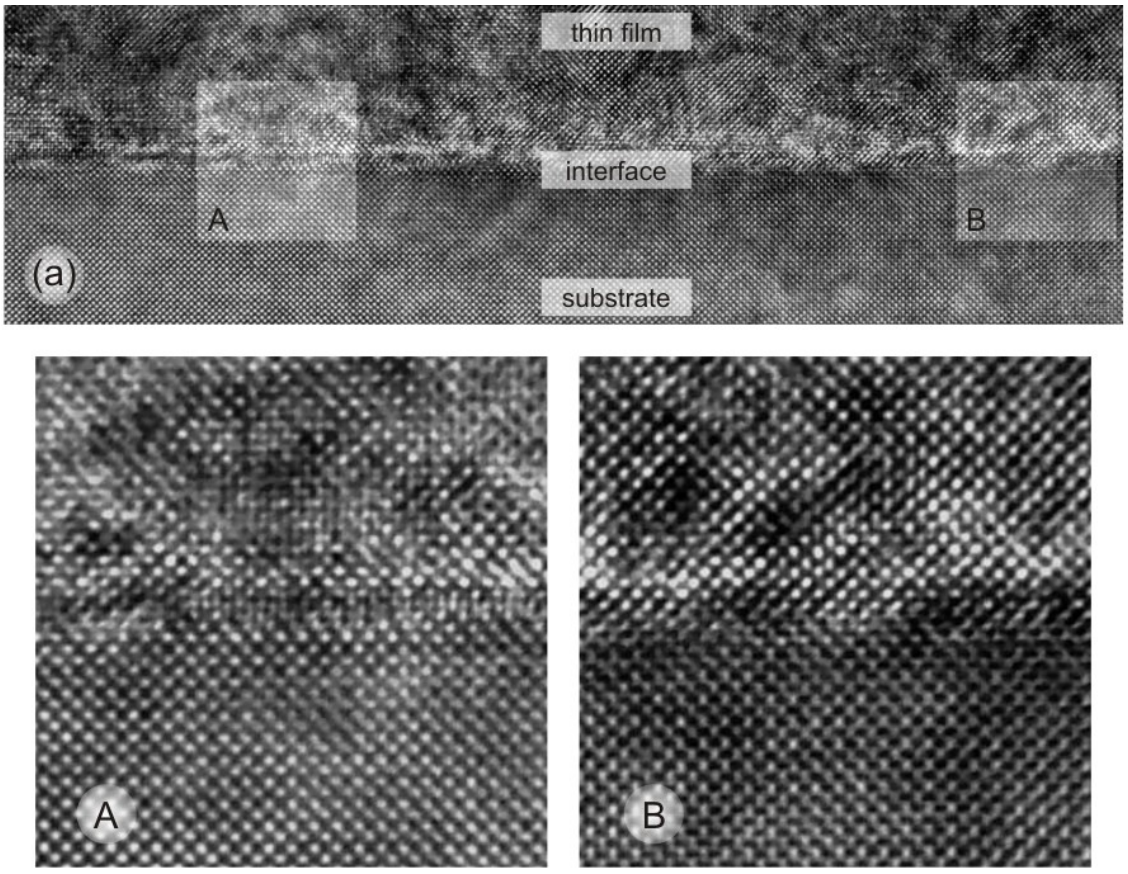

Figure 34
HRTEM cross-sectional image of a $Sr_{0.8}Ca_{0.2}RuO_3$ thin film on $SrTiO_3$on an area of 62×18 nm^2 (a). Regions A and B are magnified to show details of the structure.

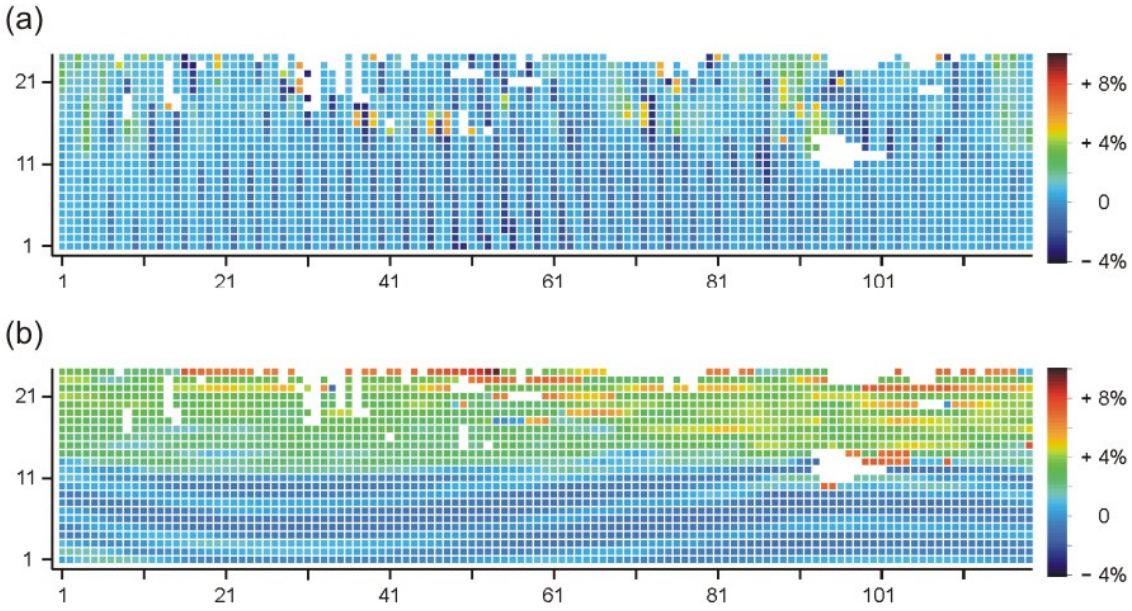

Figure 35
In-plane (a) and out-of-plane (b) lattice spacing calculated locally using a HRTEM cross-sectional image of a $Sr_{0.8}Ca_{0.2}RuO_3$ thin film on $SrTiO_3$. A color scale shows a deviation of the atomic distance from an average defined for the cubic substrate.

A room temperature electrical resistivity measured with a standard four-point method varied from 1.5 to 5 mΩ cm for most of the samples. The lowest values were obtained for the thin films with the out-of-plane lattice constant close to 4.06 Å.

4.4. $Sr_{0.6}Ca_{0.4}RuO_3$ on $SrTiO_3$

The x-ray θ-2θ scans of $Sr_{0.6}Ca_{0.4}RuO_3$ thin films deposited on $SrTiO_3$ showed a complete set of (00*l*) substrate and thin film peaks (fig. 36a). No other reflections were present. Intensities of the thin film peaks were rather low, positions and shapes varied.

As in the case of $Sr_{0.8}Ca_{0.2}RuO_3$ thin films were divided into two groups. The samples with a large amount of poorly oriented phase, having complex rocking curves with a very pronounced broad component (fig. 36b – gray) were included in the first group. Second group consisted of those characterized by a better alignment, a sharp interface with substrate and a flat surface. Their typical rocking curve had a very small broad component but a dominating narrow one had a FWHM below 0.07° (fig. 36b – black).

In case of the second type samples, clearly visible intensity oscillations (fig. 36a) allowed a calculation of the thickness and the out-of-plane lattice constant. The latter was then confirmed with a Rietveld analysis.

The out-of-plane lattice constant remained in the range of 4.04-4.08 Å. The in-plane lattice constant was estimated at 3.912 Å (again slightly higher than that of $SrTiO_3$) from reciprocal space scans (fig. 38) around (103) $SrTiO_3$ peak.

The AFM scans show a complex, non–uniform topography of the surface (fig. 37a-37c). It was relatively flat with a variety of hillocks protruding from it up to 10 nm high. Their shapes were irregular but in some cases they seemed to form elongated structures oriented along one specific direction. Roughness of the surface, as indicated by rms value, was between 1-2 nm on a 4×4 μm^2 area.

The RBS measurements gave rather high χ_{min} values, as shown in the table 7. The Ru/(Sr+Ca) ratio, obtained from the simulations (fig. 39), was close to 0.55. Again (as for the $Sr_{0.8}Ca_{0.2}RuO_3$ thin films) the content of ruthenium and oxygen decreased with the increasing deposition temperature. There seem to be a slight difference between the Sr/Ca ratio calculated for the thin films and the one obtained from chemical analysis of the target.

Table 7
Composition of the $Sr_{0.6}Ca_{0.4}RuO_3$ thin films inferred from RBS spectra.

Deposition temperature [°C]	Thickness of the thin film [nm]	Yield ratio χ_{min} [%]	Molar ratio			
			Sr	Ca	Ru	O
580	20	21.1	0.65	0.35	0.55	2.5
660	19	14.8	0.60	0.40	0.50	2.2

For the $Sr_{0.6}Ca_{0.4}RuO_3$ composition the XPS spectra of two samples, both stored for over a year under normal conditions, were taken. The results were similar thus only one set is shown in the table 8. As in the case of the $Sr_{0.8}Ca_{0.2}RuO_3$ samples O1*s*, Sr3*d* and Ca2*p* (fig. 40) spectra clearly consisted of lattice and surface components. One line or doublet was again fitted to the lattice and two to the surface part of each spectrum. However, the lattice component lines were wider (1.0-1.4 eV) and the Sr3*d* as well as Ca2*p* doublets had slightly higher (about 0.2 eV) binding energies. Their intensities were much higher measured at the angle of 45º than at 20º but still very low compared to the intensities of the surface component. The widths of the surface component lines were larger than for the lattice component and also larger than for corresponding lines of the $Sr_{0.8}Ca_{0.2}RuO_3$ composition. O1*s* surface component (fig. 40) was centered at a binding energy of 531.5 eV.

Ru3*p* line (fig. 40) was over 4 eV wide and its relative intensity increased with increasing analysis angle.

Table 8
Positions, half widths and relative intensities of lattice and surface components inferred from the experimental XPS spectra for the $Sr_{0.6}Ca_{0.4}RuO_3$ thin film stored for over a year.

		Center	Half-width	%mol	
				45°	20°
O1*s*	Line 1	528.9 eV	1.1 eV	7.4 %	4.1 %
	Line 2	531.5 eV	2.9 eV	66.1 %	71.4 %
	Line 3	533.8 eV	1.6 eV		
Sr $3d_{5/2}$ ($3d_{3/2}$) Δ = 1.8 eV	Doublet 1	132.2 eV	1.0 eV	4.8 %	2.7 %
	Doublet 2	132.8 eV	1.0 eV	6.7 %	9.0 %
	Doublet 3	133.6 eV	1.8 eV		
Ca $2p_{3/2}$ ($2p_{1/2}$) Δ = 3.5 eV	Doublet 1	344.3 eV	1.4 eV	0.8 %	0.4 %
	Doublet 2	346.2 eV	1.6 eV	3.8 %	4.5 %
	Doublet 3	347.6 eV	1.8 eV		
Ru $3p_{3/2}$	Line	464.4 eV	4.1 eV	10.4 %	7.8 %

The thickness of the surface layer was calculated for Sr3*d*, O1*s* and Ca2*p* spectra and both analysis angles. The six obtained values were diverse, varying from 1.1 nm for Sr3*d* at lower angle to 2.8 nm for O1*s* at higher angle. Reliability of the results becomes lower for the long stored samples as the intensity ratio between surface and lattice components increases. Nevertheless the numbers indicate that the simple bilayer model should be considered only an approximation for a description of the near-surface region. More likely, the change of ruthenium concentration is gradual and may extend over a few nanometers depth. The average value, 1.9 ±0.6 nm is much higher compared to 1.0 nm calculated for the $Sr_{0.8}Ca_{0.2}RuO_3$ thin film measured ½ hour after deposition.

Although all the produced samples were macroscopically nonconductive the valence band spectra revealed similar character of atomic bonds to that observed for the conductive samples of the $SrRuO_3$ and $Sr_{0.8}Ca_{0.2}RuO_3$ thin films. Again the steep slope was present at the Fermi level and two main features appeared, centered at about 1.5 eV and 6.2 eV (p. 67, fig. 60).

4.5. Aging

All the $Sr_{1-x}Ca_xRuO_3$ (x = 0, 0.2 and 0.4) thin films produced in the course of this work underwent extended process of aging while stored under normal ambient conditions. A severe deterioration of both surface topography and morphology was revealed by AFM and XPS analysis. At the same time XRD scans did not show any changes of the lattice parameters, epitaxy measured with FWHMs of rocking curves or sample thickness and brought no evidence of formation of different crystallographic phases.

The $Sr_{0.8}Ca_{0.2}RuO_3$ thin films, after an extended period of time seemed to be fully covered with a layer of contaminations (fig. 41b). Although the cover was not uniform it was thick enough to make the atomic steps no longer visible. The rms roughness changed from 0.3 nm to about 1 nm. In the case of the $Sr_{0.6}Ca_{0.4}RuO_3$ thin films similar contamination layer smoothened the surface (fig. 43b) filling the narrow crevices observed for the fresh samples. The roughness remained in the range of 1-2 nm.

Formation of the adsorbed overlayer was accompanied with a significant change of the character of atomic bonds. It is especially clear when one compares the XPS spectra of the $Sr_{0.8}Ca_{0.2}RuO_3$ sample measured after being stored for approximately 140 days (fig. 42 and table 9) with the spectra obtained ½ hour after sample deposition (figure 42 and table 6 at page 35).

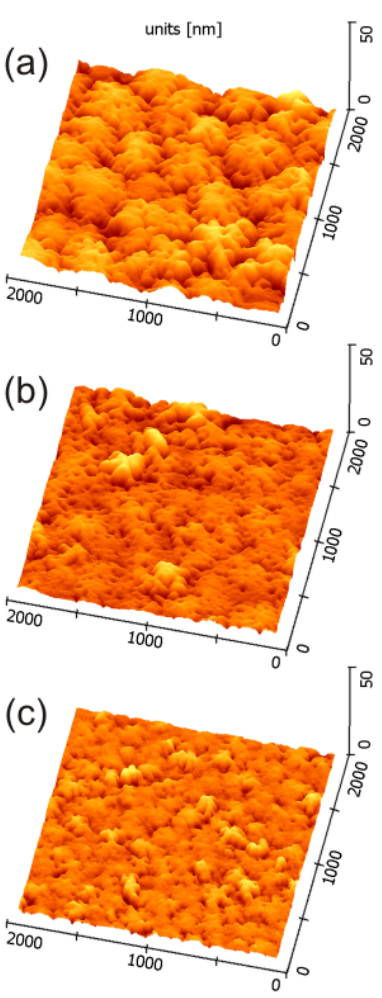

Figure 37
AFM images for $Sr_{0.6}Ca_{0.4}RuO_3$ thin films deposited on $SrTiO_3$ with different temperature and substrate-target distance: 610 °C, 36 mm (a), 610 °C, 40 mm (b), 660 °C, 44 mm (c).

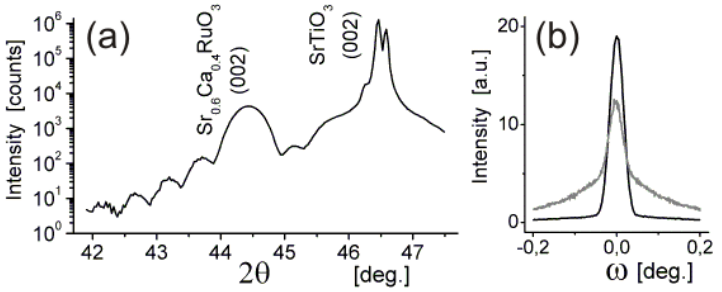

Figure 36
X-ray θ-2θ scan (a) and ω-rocking curve (b) of (002) peak, for a well aligned $Sr_{0.6}Ca_{0.4}RuO_3$ thin film on $SrTiO_3$ (black lines). A rocking curve of a poorly aligned thin film is shown for comparison (gray).

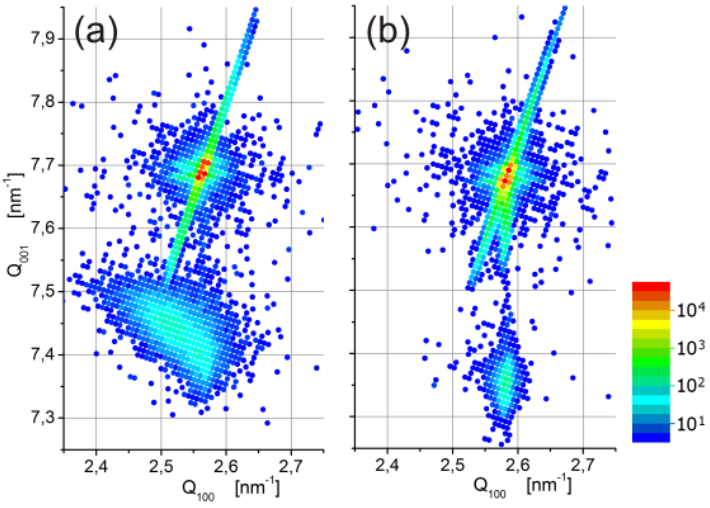

Figure 38
XRD reciprocal space maps measured around the (103) $SrTiO_3$ peak for $Sr_{0.6}Ca_{0.4}RuO_3$ thin films. Both, poorly (a) and well aligned (b) types of thin films are presented.

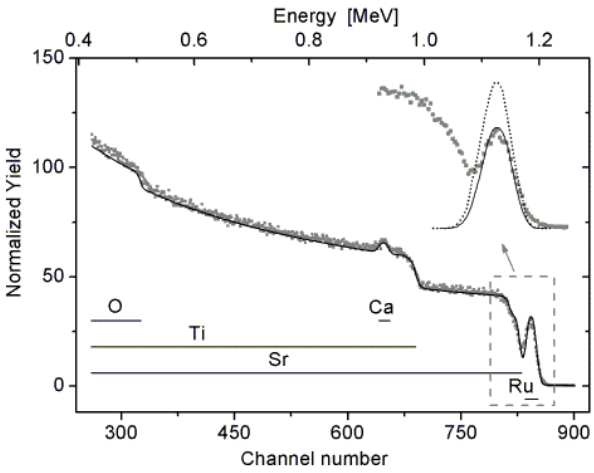

Figure 39
RBS spectum (points) and simulation (line) obtained for a 19 nm thick $Sr_{0.6}Ca_{0.4}RuO_3$ film deposited on $SrTiO_3$. A thin film region is enlarged in an inset. The simulations are presented for Ru/(Sr+Ca) ratios of 0.5 (solid) and 1 (dots) for comparison.

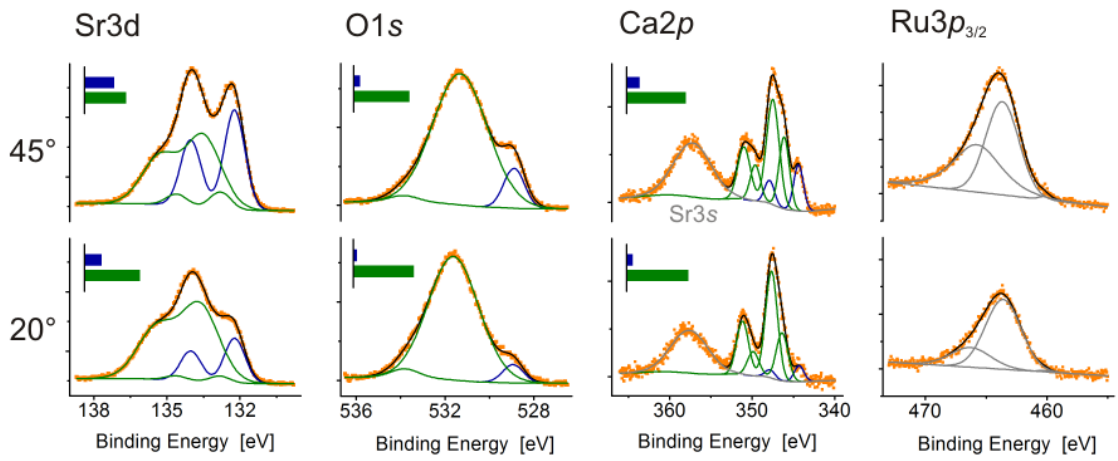

Figure 40
XPS core spectra for a $Sr_{0.6}Ca_{0.4}RuO_3$ thin film deposited on $SrTiO_3$, taken at two analysis angles (45° and 20°). Individual lines or doublets fitted to the spectra are presented and perovskite lattice contribution (blue) distinguished from the one coming from surface compounds (green) wherever possible. Small bar graphs show relative intensities of the lattice- and surface-originating components.

Table 9
Positions, half widths and relative intensities of lattice and surface components inferred from the experimental XPS spectra for the sample stored for approximately 140 days.

		Center	Half-width	%mol	
				45°	20°
O1*s*	Line 1	528.9 eV	1.1 eV	8.0 %	3.6 %
	Line 2	530.2 eV	1.8 eV	67.2 %	74.4 %
	Line 3	532.3 eV	2.1 eV		
Sr $3d_{5/2}$ ($3d_{3/2}$) Δ = 1.8 eV	Doublet 1	132.0 eV	0.95 eV	5.3 %	2.4 %
	Doublet 2	132.8 eV	1.3 eV	8.7 %	11.0 %
	Doublet 3	134.0 eV	1.4 eV		
Ca $2p_{3/2}$ ($2p_{1/2}$) Δ = 3.5 eV	Doublet 1	343.8 eV	1.15 eV	0.5 %	0.2 %
	Doublet 2	347.3 eV	2.5 eV	2.5 %	2.9 %
	Doublet 3	347.7 eV	1.3 eV		
Ru $3p_{3/2}$	Line	463.8 eV	4.3 eV	7.9 %	5.6 %

As in the case of the fresh sample in all core spectra, except for Ru3*p* line, lattice and surface components were easily distinguished. Although the number of photoelectrons forming the lattice part of Sr3*d*, Ca2*p* and O1*s* spectra at both analysis angles was largely reduced (2-4 times) the peaks were still equally narrow. The main surface component O1*s* line was shifted by 1.4 eV to higher binding energy after several days of storage. Concurrently a similar energy shift was observed for the surface part of Sr3*d* spectra. Relative intensity of the Ru3*p* line decreased significantly compared to the fresh sample.

The average value of the thickness of the surface layer estimated with the Cumpson and Seah bilayer model was 1.9 ±0.6 nm. The adsorbed cover was therefore much thicker than ½ hour after the deposition (1.0 nm) and similar to the one found on the long stored $Sr_{0.6}Ca_{0.4}RuO_3$ thin film (1.8 nm). The average stoichiometry of the surface region measured at the angle of 45° changed from the (Sr+Ca:Ru:O) = 1:0.5:2.9 for the fresh sample to 1:0.47:4.44 after long-term storage.

Such a change points to a complex and extended in time aging process. It was noticed before, that the $SrRuO_3$ thin films very easily adsorbed contaminations present in an ambient atmosphere, presumably carbon dioxide and water, even at room temperature[73]. Their incorporation in the structure of the thin film might explain widening of the surface region.

4.6. Reduction and oxidation

To investigate thermal stability of the thin films and get a better understanding of the aging process the samples were subjected to annealing under oxidizing and reducing conditions. Most of the experiments were carried out in a quartz tube using an induction-heated furnace. The tube was first evacuated to a background pressure of about 10^{-6} mbar and flushed a few times with oxygen. Then the samples were exposed to elevated temperatures at different partial pressures of oxygen and cooled down at a fast rate by removing the tube from the furnace and quenching it with water. The $SrRuO_3$ thin film was annealed in air using a standard ceramic furnace and in vacuum on the hot plate at the deposition chamber. For every sample the changes of the surface region were investigated by means of AFM and XPS. The crystal structure of the $SrRuO_3$ samples was additionally checked with XRD.

To determine the temperature range where substantial changes can be expected first a thermogravimetry analysis, using Netzsch thermobalance type TG439, was performed for polycrystalline $SrRuO_3$ samples. Few-gram samples were obtained by cutting a ceramic target used for deposition of thin films. It was mentioned before that the target contained about 20% excess of RuO_2.

Annealing at 800 ºC in 1 bar of a 79%Ar+21%O_2 mixture or the same mixture with an addition of 40 mbar H_2O did not cause any mass loss of the samples (fig. 44 – blue). θ-2θ scan of the sample exposed to a pure oxygen atmosphere at a temperature of 800 ºC and a pressure of a few mbar remained unchanged. A large loss of the sample mass occurred rapidly when annealing in 1 bar of a 96%Ar+4%H_2 mixture at 400 ºC was performed (fig. 44 – red). Addition of 40 mbar H_2O (fig. 44 – green) shifted the temperature of this process to about 450 ºC but the amount of 12.9% of the lost substance was exactly the same. During annealing $SrRuO_3$ decomposed completely following the reaction proposed by Lin *et al.* [103]

$$SrRuO_3 + 2H_2 \rightarrow Ru + SrO + 2H_2O$$

which might be facilitated by the prior thermal decomposition

$$SrRuO_3 \xrightarrow{T} RuO_2 + SrO$$

$$RuO_2 + 2H_2 \rightarrow Ru + 2H_2O$$

The number 14.8%, calculated for the full chemical reaction, and taking into account 20% RuO_2 excess, slightly differed from the experimental value. Furthermore, in the θ-2θ scan, besides a set of metallic Ru (space group $P6_3/mmc$) peaks, a few unidentified peaks were observed (not presented). That may be due to the concurrent formation of complex $SrO–H_2O$ compounds, as reported by Halley *et al.* [72] It is noteworthy that at the temperature as low as 400 ºC, when Ar/H_2 mixture was replaced by Ar/O_2, about 11.2% recovery of sample mass was observed. This process was identified as ruthenium reoxidation, which was previously reported to occur at this temperature range[104], for metallic Ru films. Moreover, according to the authors, reoxidation at 400 ºC seemed to be much more efficient in a mixture of Ru and SrO compared to pure Ru films. The final oxidation state for our samples was found to be higher than $RuO_{1.5}$. About 1.7% difference between initial and final sample mass may be due to the loss of volatile ruthenium or strontium oxides. E.g. a significant loss of SrO was observed by Shin *et al.* [34] under high vacuum conditions, after heating $SrRuO_3$ up to 500 ºC.

According to these results the $SrRuO_3$ thin films were annealed under different conditions, including short (1 h) and long (24 h) term annealing at an oxygen pressure below 10^{-5} mbar and a temperature of about 600 ºC, 24 h-annealing at 1 atm of air, and a temperature of 800 ºC and about 12 h-annealing in H_2 atmosphere at a pressure of 1 mbar and a temperature of 450 ºC. Oxygen partial pressure calculated for hydrogen annealing was lower than 10^{-36} mbar (for details of the calculation see appendix B).

Annealing in air at a temperature of 800 ºC led to an essential change of the surface topography, measured by AFM (fig. 45b). The surface consisted of rectangular regions attaining the width of hundreds of nanometers, ordered in parallel. Single regions were flat and free of features and resembled monocrystal grains. The rms roughness was about 0.39 nm on an 8×8 μm^2 area (<0.2 nm for the as-made sample). The x-ray θ-2θ scan did not show any changes of the out of plane lattice constant or deterioration of the crystal structure. In fact, the sample was still uniform enough to display the oscillations at the shoulders of the $SrRuO_3$ (002) x-ray peak and a narrowing of the rocking curve from 0.055º to 0.04º suggested an improvement of the thin film epitaxy.

Annealing in vacuum was carried out with the heater temperature varying from 400 ºC to 800 ºC in 50 ºC steps. At a heater temperature of 800 ºC a change of topography was observed. At this stage the surface temperature, measured by a pyrometer, was about 610 °C. Accordingly the next sample was annealed in a quartz tube at the temperature of about 600 °C and the oxygen pressure of about 10^{-5} mbar for 1 hour. After the treatment the surface was still flat and the thickness uniform, as shown in the AFM picture (fig. 45c) and confirmed by the x-ray θ-2θ scan intensity oscillations. Numerous precipitates, tens of nanometers in diameter and 5-20 nm high, appeared at the surface, changing the rms roughness to a value of about 0.37 nm on an 8×8 μm^2 area. The rocking curve became clearly asymmetric and several components less than 0.03º wide and separated by about 0.02º were noticeable although the FWHM of the whole curve remained unchanged. It may be an indication that the crystal grains forming the mosaic structure tended to group in microtwins locally improving epitaxy.

Annealing in air as well as short-term annealing in vacuum had little influence on the number and shapes of the Sr3*d* or O1*s* XPS lines (fig. 46a-46c). Neither of the treatments affected the positions or widths of fitted lines and doublets except for a minor narrowing of the O1*s* surface component. A lot more substantial was the change of the relative intensities. After both, air and vacuum annealing, the amount of the lattice strontium and oxygen observed at the spectra became significantly smaller regardless of the analysis angle. The Ru3*p* doublet was slightly shifted to a higher binding energy after air annealing and to a lower energy after annealing in vacuum (fig. 47b and 47c). Its relative intensity decreased after annealing, regardless of oxygen presence in the ambience (fig. 48). The highest drop was observed at the surface. General stoichiometry of the surface region derived from XPS spectra, taken at the angle of 50º, for the as-grown thin film was Sr:Ru:O = 1:0.7:3.1. After a long-term oxygen-rich annealing stoichiometry observed at the same angle changed to Sr:Ru:O = 1:0.4:3.1 and short-term vacuum annealing led to Sr:Ru:O = 1:0.6:2.9.

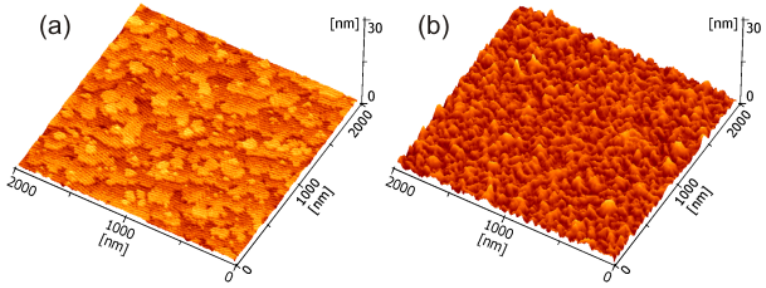

Figure 41
AFM topography scans for a fresh (a) and a long term stored (b) $Sr_{0.8}Ca_{0.2}RuO_3$ thin film deposited on $SrTiO_3$.

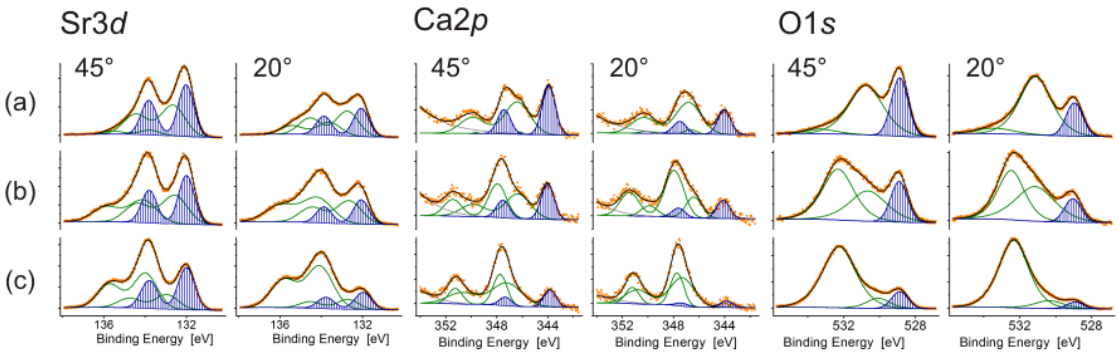

Figure 42
XPS core spectra for $Sr_{0.8}Ca_{0.2}RuO_3$ thin films deposited on $SrTiO_3$, taken at two analysis angles (45° and 20°). The samples were stored under normal conditions for 1/2 h (a), 37 days (b) and 145 days (c) before measurement. Perovskite lattice contribution (blue) is distinguished from the one coming from surface compounds (green).

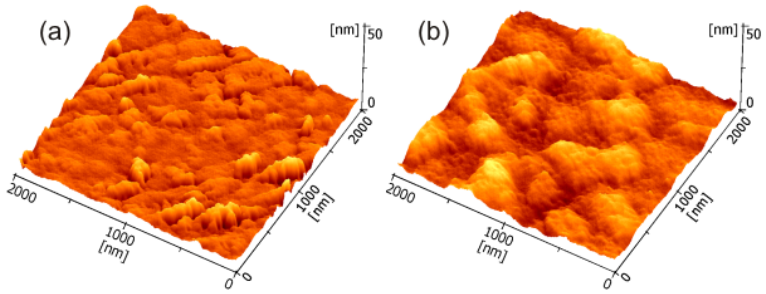

Figure 43
AFM topography scans for a fresh (a) and a long term stored (b) $Sr_{0.6}Ca_{0.4}RuO_3$ thin film deposited on $SrTiO_3$.

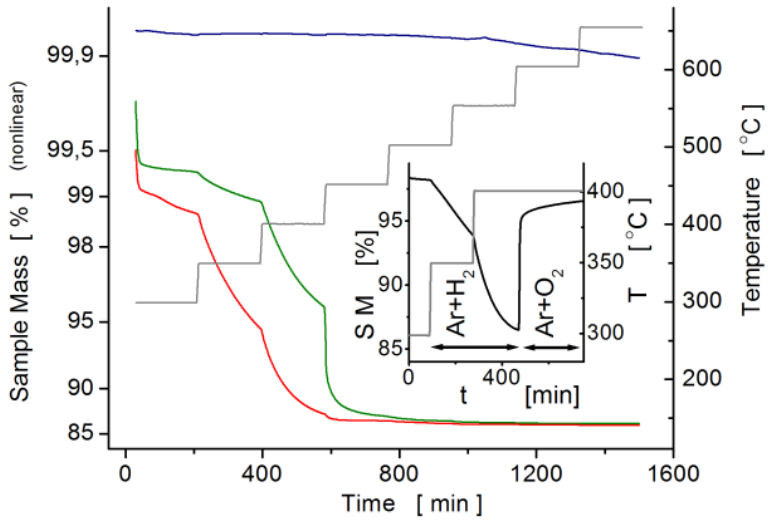

Figure 44
Thermogravimetry Analysis for polycrystalline $SrRuO_3$ samples annealed in air (blue), 96%Ar + 4%H_2 mixture (red) and 96%Ar + 4%H_2 + 40 mbar H_2O mixture (green). Inset shows reduction of a sample in H_2 containing environment and then its reoxidation after replacing H_2 with O_2. The temperature steps during annealing are shown in gray.

Long-term vacuum annealing and H_2 annealing led to a complete deterioration of the surface. In these cases also the $SrRuO_3$ peaks disappeared from θ-2θ x-ray scans, which confirmed a decomposition of the bulk structure of the thin film. In the XPS spectra (fig. 47d) of the long-term vacuum annealed sample the FWHM of the Ru3$p_{3/2}$ line decreased by more than 1.6 eV and the binding energy was about 2.5 eV lower (461.6 eV) compared to the as-grown sample. This is a strong indication that majority of Ru ions underwent a reduction to the metallic state. Such conclusion is supported by the fact that after a reduction by pure H_2 annealing the Ru3$p_{3/2}$ peak had exactly the same parameters (fig. 47e). Simultaneously the lattice part disappeared completely from the Sr3*d* spectra in both cases (fig. 46d). Calculated stoichiometries were also similar, Sr:Ru:O = 1:0.3:2.8.

After the short-term reduction of the $SrRuO_3$ thin film intensity of the valence band spectrum near the Fermi level increased and the slope became steeper. For the long-term reduced samples in which mainly metallic Ru remained, the valence band structure changed completely. The intensity of the spectra near the Fermi level significantly decreased and two maxima, centered at 0.8 eV and 6.4 eV for the as-grown samples moved closer to each other (p. 67, fig. 60).

The oxidation and reduction of the $Sr_{0.8}Ca_{0.2}RuO_3$ and $Sr_{0.6}Ca_{0.4}RuO_3$ thin films was performed with several modifications based on the results obtained for the $SrRuO_3$ samples. The quality of every specimen was first checked with XRD and AFM and then cleaved into four parts. One part was left as a reference and the other three annealed at different temperatures. Oxidation was carried out under the oxygen pressure of 1 mbar at the temperatures of 600 ºC, 750 ºC and 900 ºC for 3 hours and reduction under the oxygen pressure of 10^{-5} mbar at the temperatures of 500 ºC, 600 ºC and 700 ºC for ½ hour. All the parts of every sample were measured with AFM and XPS. The procedure of such an experiment required several days to complete therefore the samples used should be considered as long-term stored.

The samples of both compositions oxidized at 600 ºC displayed similar topography (fig. 49b and 51b). Numerous irregularly shaped precipitations appeared on the surface changing the rms roughness from the reference values of about 0.7 nm and 1.6 nm to 5.2 nm and 4.8 nm, for the $Sr_{0.8}Ca_{0.2}RuO_3$ and $Sr_{0.6}Ca_{0.4}RuO_3$ thin film respectively. Oxidation at 750 ºC led to a significant structural transformation of the bulk of both thin films (fig. 49c and 51c) resembling that observed for the $SrRuO_3$ thin film annealed in air. Fig. 49c shows the $Sr_{0.8}Ca_{0.2}RuO_3$ sample surface consisting mostly of two terraces, one rising about 10 nm above the other. All the terrace edges were oriented in two perpendicular in-plane directions, most likely the <100> and <010> axes of the substrate lattice. On top of them several crystallites were formed, having rectangular bases and up to 60 nm high. Crystallites covering the surface of the $Sr_{0.6}Ca_{0.4}RuO_3$ sample were more rounded and in some cases as high as 100 nm (fig. 51c). At 900 ºC the $Sr_{0.8}Ca_{0.2}RuO_3$ terrace structure became less uniform and riddled with holes and the crystallites attained the in-plane and out-of-plane dimensions exceeding 100 nm (fig. 49d). 3 hour treatment at the same temperature completely removed the $Sr_{0.6}Ca_{0.4}RuO_3$ thin film from the scanned areas of the substrate.

The XPS analysis showed (fig. 50 and 52) that the oxidation increased the relative amount of strontium in the surface region of the $Sr_{0.8}Ca_{0.2}RuO_3$ and $Sr_{0.6}Ca_{0.4}RuO_3$ thin films. The higher the annealing temperature the stronger was the total Sr3*d* signal in the XPS spectra however the lattice part remained nearly constant and the same as for the reference samples. The surface part of every spectrum shifted to lower binding energy. At the lower annealing temperatures the change of the calcium content was similar to that of Sr and the Ca/Sr ratio in the surface region remained constant or even slightly increased (fig. 50b and 52b). At 750 ºC for the $Sr_{0.6}Ca_{0.4}RuO_3$ and 900 ºC for the $Sr_{0.8}Ca_{0.2}RuO_3$ sample the total intensity of the Ca2*p* signal dropped back to the reference level (fig. 52d and 50c). The relative oxygen content did not change after oxygen-rich annealing of any sample. At the same time the lattice part measured at the angle of 45º for the $Sr_{0.8}Ca_{0.2}RuO_3$ sample gained about 50% of its reference intensity, regardless of the annealing temperature and even more measured at 20º. The O1*s* lattice part for the $Sr_{0.6}Ca_{0.4}RuO_3$ specimen annealed at 750 ºC increased about twice compared to the reference value (fig. 52c). For both compositions oxidation led to a significant decrease of the intensity of the O1*s* high-energy surface peak centered at about 532 eV. Simultaneously the surface peak at about 530.5 eV became more pronounced with growing temperature of the treatment, especially in case of the $Sr_{0.8}Ca_{0.2}RuO_3$ sample. The temperature of the process influenced also Ru content of the surface region of the samples (fig. 50 and 52). The higher the temperature the lower was the intensity of the Ru3*p* signal. The oxidation level slightly increased when the sample was annealed up to a certain temperature. At 750 ºC for the $Sr_{0.6}Ca_{0.4}RuO_3$ and 900 ºC for the $Sr_{0.8}Ca_{0.2}RuO_3$ thin film the Ti2*p* doublet appeared in the XPS spectra (fig. 52c and 50d). This, together with AFM results, indicated that the substrate became partially uncovered and thus a substantial deterioration of the bulk of each sample. At this stage ruthenium in the $Sr_{0.8}Ca_{0.2}RuO_3$ sample underwent a reduction to several low-oxidation states.

The total intensity of the core lines was used to calculate the stoichiometry of the surface region. The sum of Sr and Ca atomic fractions was fixed at 1 and used as a reference point. The results representative of the whole sets of samples were presented in the table 10.

The valence band spectra (p. 67, fig. 60) of the samples of both compositions showed a constant lowering of the intensity near the Fermi level with the oxidation temperature. This change was more pronounced when observed at the angle of 20º. The second maximum, located at about 6 eV split in two.

The reduction of the $Sr_{0.6}Ca_{0.4}RuO_3$ thin film had little influence on the surface topography (fig. 55). A long-term stored sample was used in the process and therefore the reference specimen was more uniform than a fresh one. Its grainy texture slightly improved with annealing temperature from the reference value of rms roughness of 2.1 nm to 1.5 nm at 600 ºC but the original topography of the fresh sample was not recovered (fig. 55c). Then, after annealing at 700 ºC the grains became larger and more distinct, which increased the roughness to 2.3 nm (fig. 55d). The evolution of the $Sr_{0.8}Ca_{0.2}RuO_3$ thin film surface was similar (fig. 53c and 53d), except for the change observed at 500 ºC (fig. 53b). Reduction at this temperature resulted in a sudden erosion of the surface as indicated by the rms roughness exceeding 5 nm. Sample treated at 600 ºC was again very flat (rms roughness of about 0.8 nm) with a small number of precipitations a few nanometers high. Annealing at the temperature of 700 ºC led to a development of the grainy texture resembling the one described for the reduced $Sr_{0.6}Ca_{0.4}RuO_3$ thin film and the increase of the roughness to 3.6 nm.

Intensity of the Sr3*d* XPS spectra of both, the $Sr_{0.8}Ca_{0.2}RuO_3$ and $Sr_{0.6}Ca_{0.4}RuO_3$ thin films, increased with growing annealing temperature (fig. 54 and 56) even more than during oxidation. On the contrary the temperature rise caused a very fast drop of calcium content. The reduction, the same as oxidation did not influence the relative content of oxygen in the surface region of any specimen. Regardless of the temperature or the thin film composition the treatment resulted in a decrease of the lattice part of the Sr3*d*, Ca2*p* and O1*s* spectra below any significant value. At the same time the surface part of each spectrum shifted to higher binding energy. Ruthenium content diminished during oxygen-deficient annealing of both thin films, especially fast at higher temperatures. Concurrently a significant reduction of ruthenium was observed to a combination of low-oxidation states, including Ru^0.

As in the case of the oxidation process the values of stoichiometry calculated for the surface region were listed in the table 10.

The valence band spectra of the thin films of both compositions also changed after the reduction (p. 67, fig. 60). The maximum, present at about 1.1 eV and 1.4 eV for the $Sr_{0.8}Ca_{0.2}RuO_3$ and $Sr_{0.6}Ca_{0.4}RuO_3$ reference samples respectively, moved to higher binding energy but the steep slope at the Fermi level was still observed. Intensity of this region of the spectra lowered constantly with the annealing temperature for the $Sr_{0.6}Ca_{0.4}RuO_3$ samples but remained nearly constant for the $Sr_{0.8}Ca_{0.2}RuO_3$ samples annealed at 500 ºC and 600 ºC. A substantial change occurred only when the temperature reached 700 ºC. In this case the part close to Fermi level disappeared almost completely. It is worth noting that after the reduction a new maximum in the valence band spectra evolved in the range of the binding energies of 10-11 eV for all the annealed specimens.

Table 10

Atomic ratio at the surface region derived from the XPS spectra measured at the angle of 50º for the thin films of nominal stoichiometry $Sr_{0.8}Ca_{0.2}RuO_3$ and $Sr_{0.6}Ca_{0.4}RuO_3$. The values are presented for the as-made long-term stored reference samples and after the oxidation or reduction treatment.

	Sr : Ca : Ru : O	
Nominal	0.8 : 0.2 : 1 : 3	0.6 : 0.4 : 1 : 3
Reference (oxidation)	0.83 : 0.17 : 0.47 : 4.44	0.69 : 0.31 : 0.40 : 4.42
Oxidized at 750 ºC	0.78 : 0.22 : 0.23 : 3.30	0.77 : 0.23 : 0.17 : 3.04
Reference (reduction)	0.79 : 0.21 : 0.52 : 4.40	0.71 : 0.29 : 0.64 : 4.53
Reduced at 700 ºC	0.99 : 0.01 : 0.03 : 2.71	0.93 : 0.07 : 0.12 : 3.14

$SrRuO_3$
thin film deposited on $SrTiO_3$,
(a) as-made sample,
annealed:
(b) in air
at 800 °C, for 24 h,
(c) in vacuum (<10^{-5} mbar)
at 600 °C, for 1h,
(d) in vacuum
at 600 °C, for 24 h,
(e) in hydrogen
at 450 °C, for 12 h.

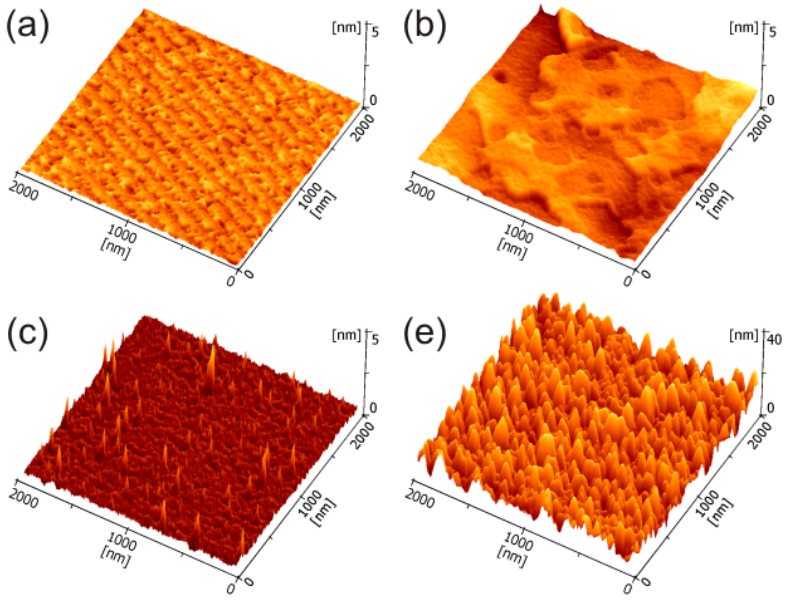

Figure 45
AFM topography images.

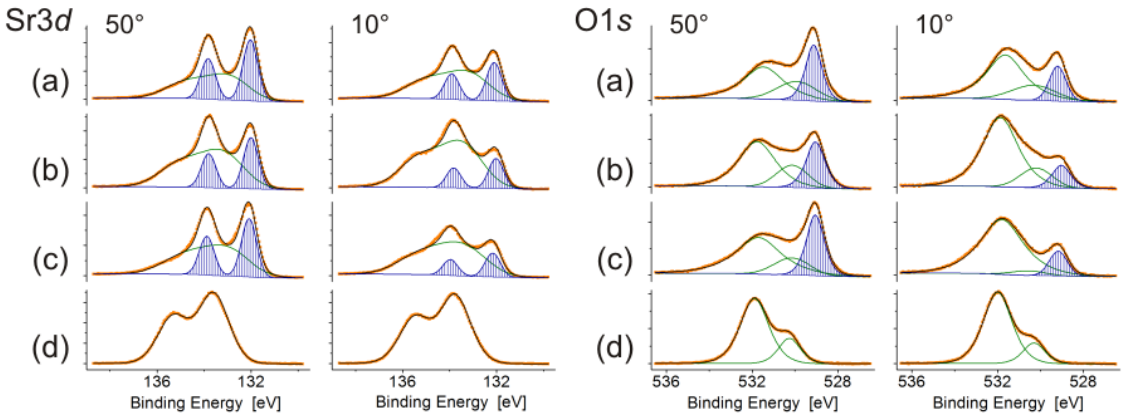

Figure 46
XPS core spectra for Sr and O taken at two analysis angles (50° and 10°). Individual lines or doublets fitted to the spectra are presented and perovskite lattice contribution (blue) distinguished from the one coming from surface compounds (green) wherever possible.

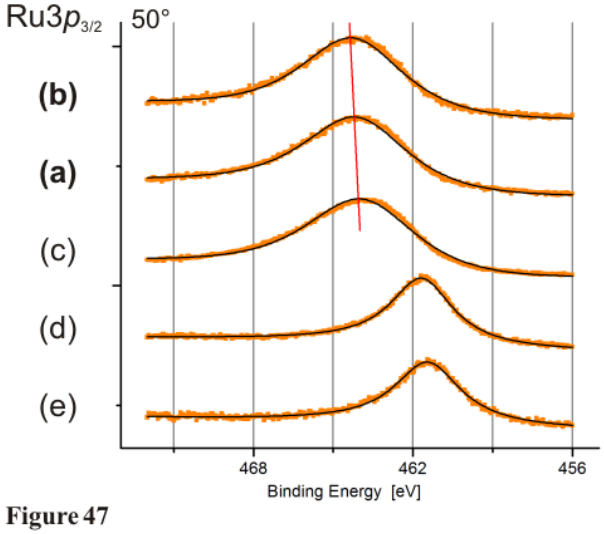

Figure 47
XPS core spectra for Ru taken at the analysis angle of 50°. Spectra of similar shapes were measured at the angle of 10°(not presented). A red line shows a shift of the center of the line caused by the sample treatment.

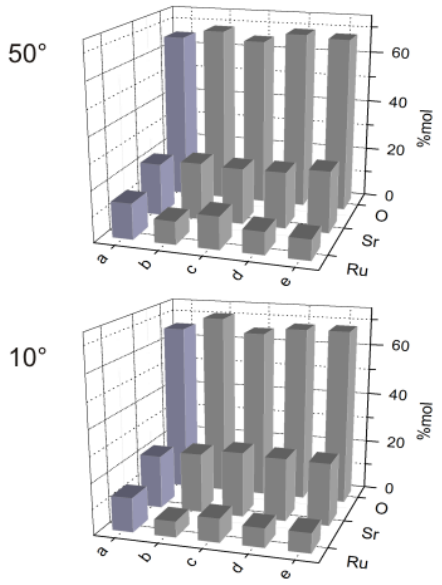

Figure 48
Treatment influence on stoichiometry of the observed surface region.

$Sr_{0.8}Ca_{0.2}RuO_3$
thin film deposited on $SrTiO_3$,
(a) as-made sample,
after 3 hours annealing under oxygen pressure of 1 mbar at a temperature of:
(b) 600 °C,
(c) 750 °C,
(d) 900 °C.

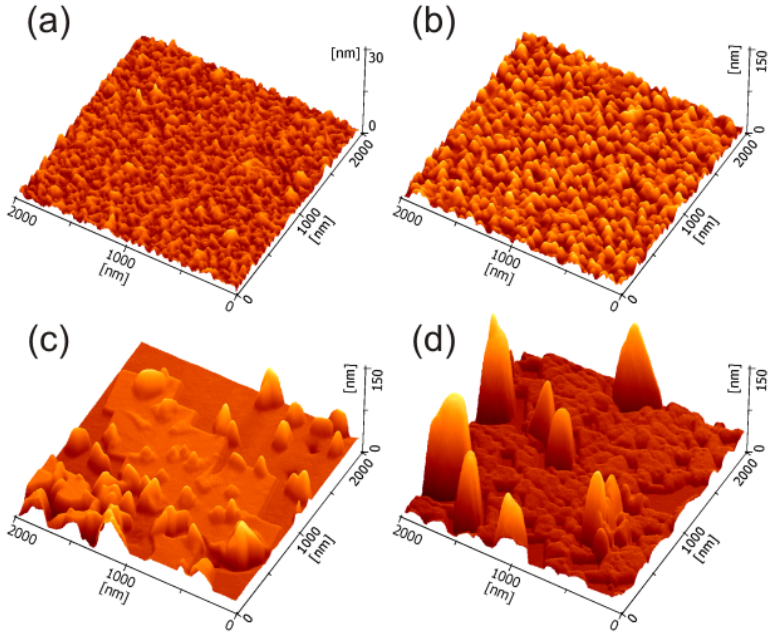

Figure 49
AFM topography images. After deposition the sample was stored for several days before annealing. Atomic steps are no longer visible (a).

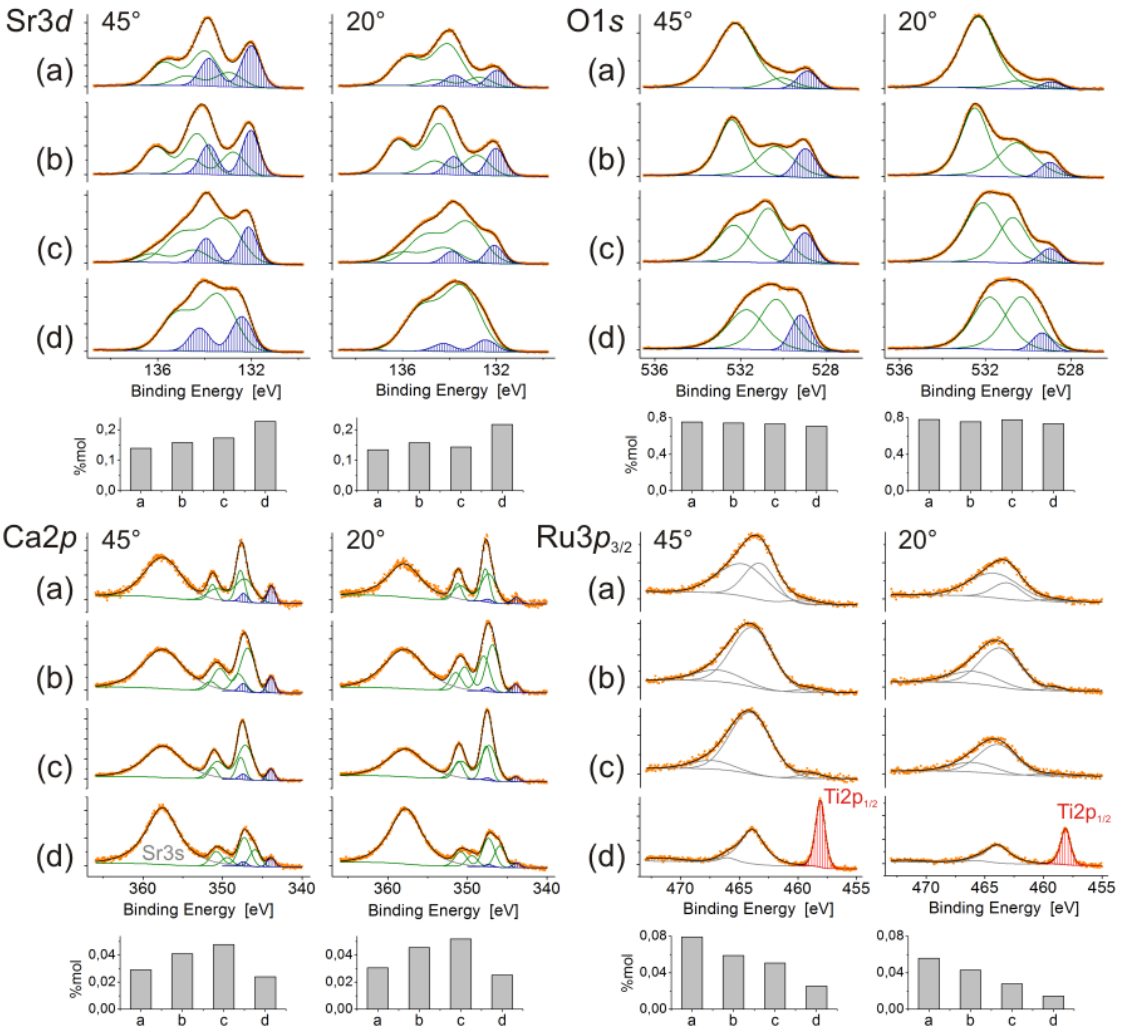

Figure 50
XPS core spectra for Sr, Ca, O and Ru taken at two analysis angles (45° and 20°). Individual lines or doublets fitted to the spectra are presented and perovskite lattice contribution (blue) distinguished from the one coming from surface compounds (green) wherever possible. Column graphs show evolution of stoichiometry of the observed region.

$Sr_{0.6}Ca_{0.4}RuO_3$ thin film deposited on $SrTiO_3$,

(a) as-made sample, after 3 hours annealing under oxygen pressure of 1 mbar at a temperature of:

(b) 600 °C,
(c) 750 °C,
(d) 900 °C.

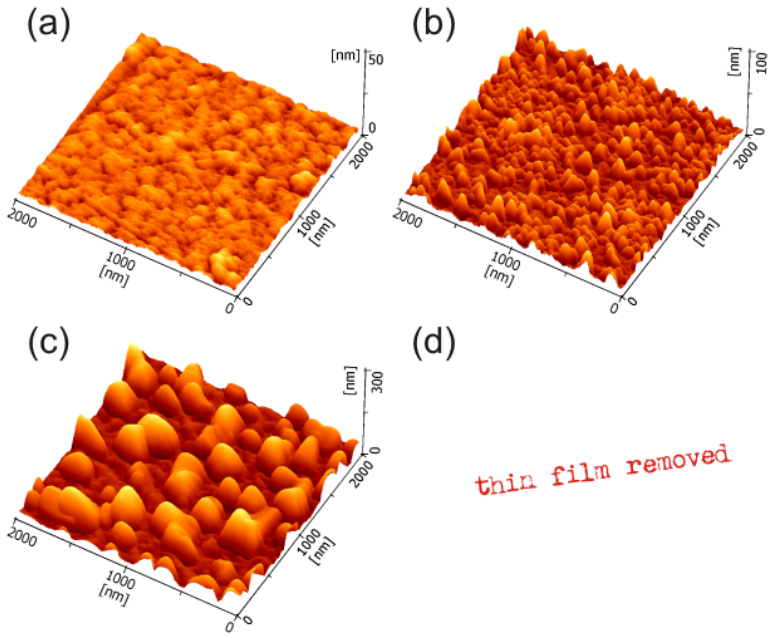

Figure 51
AFM topography images. After deposition the sample was stored for several days before annealing (a).

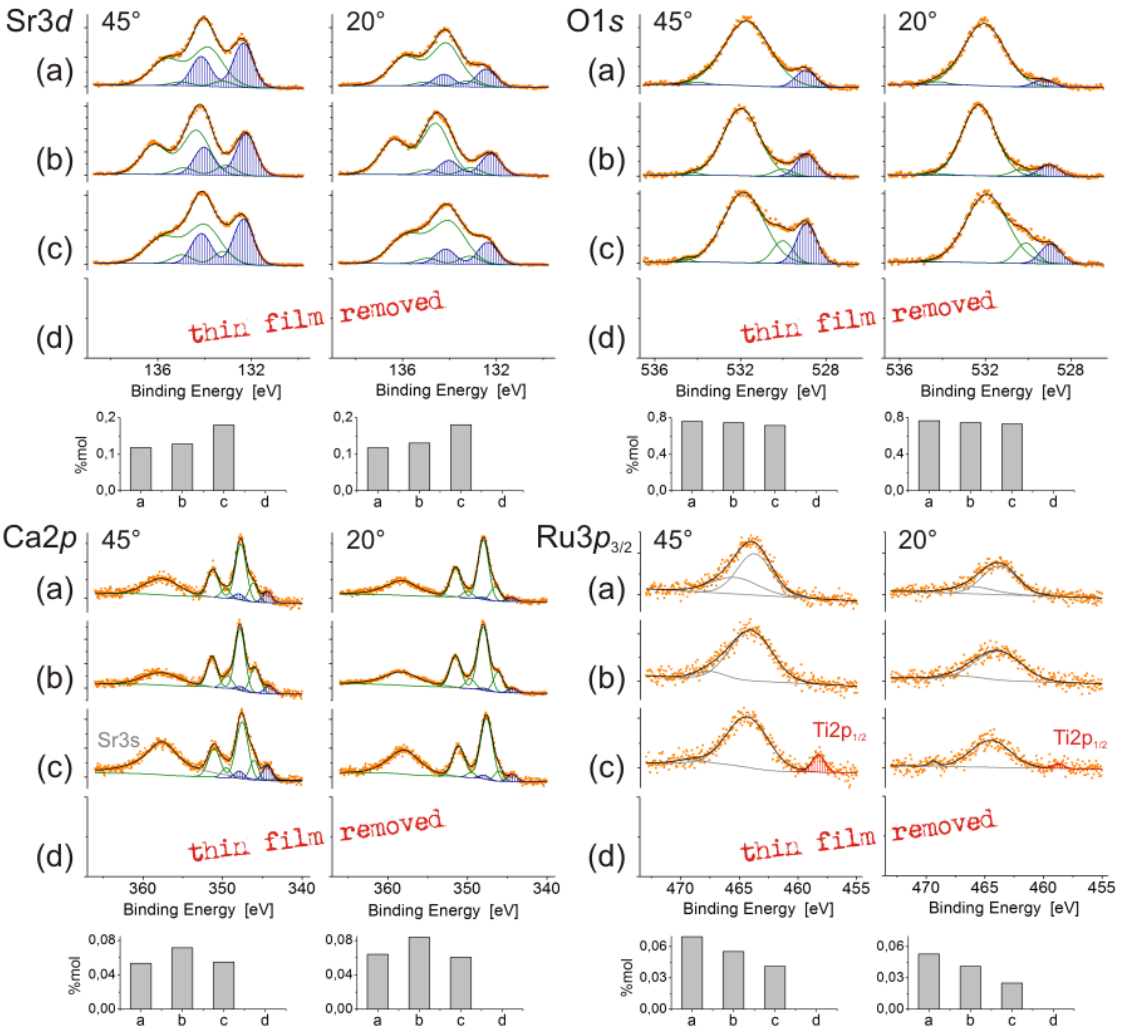

Figure 52
XPS core spectra for Sr, Ca, O and Ru taken at two analysis angles (45° and 20°). Individual lines or doublets fitted to the spectra are presented and perovskite lattice contribution (blue) distinguished from the one coming from surface compounds (green) wherever possible. Column graphs show evolution of stoichiometry of the observed region. At 900 °C the thin film was completely removed from the substrate.

$Sr_{0.8}Ca_{0.2}RuO_3$ thin film deposited on $SrTiO_3$,

(a) as-made sample, after 1/2 hour annealing under oxygen pressure below 10^{-5} mbar at a temperature of:

(b) 500 °C,
(c) 600 °C,
(d) 700 °C.

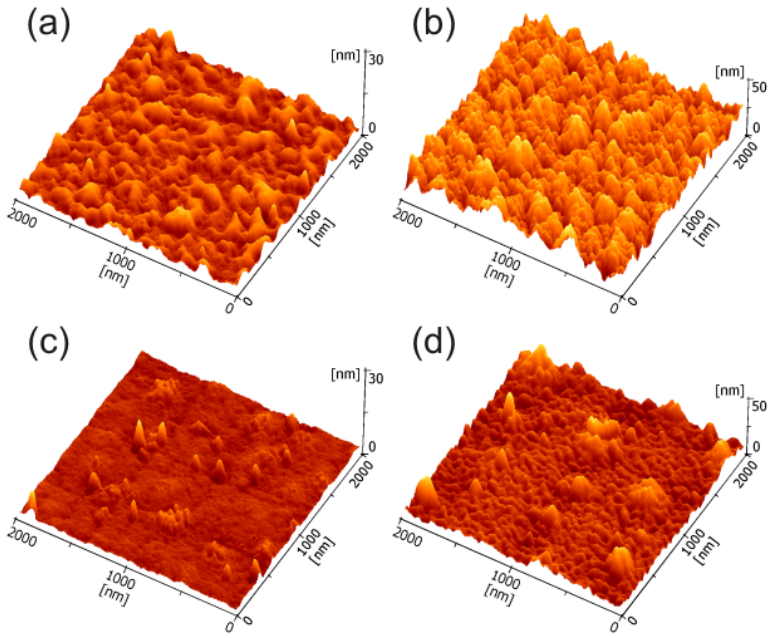

Figure 53
AFM topography images. After deposition the sample was stored for several days before annealing. Atomic steps are no longer visible (a).

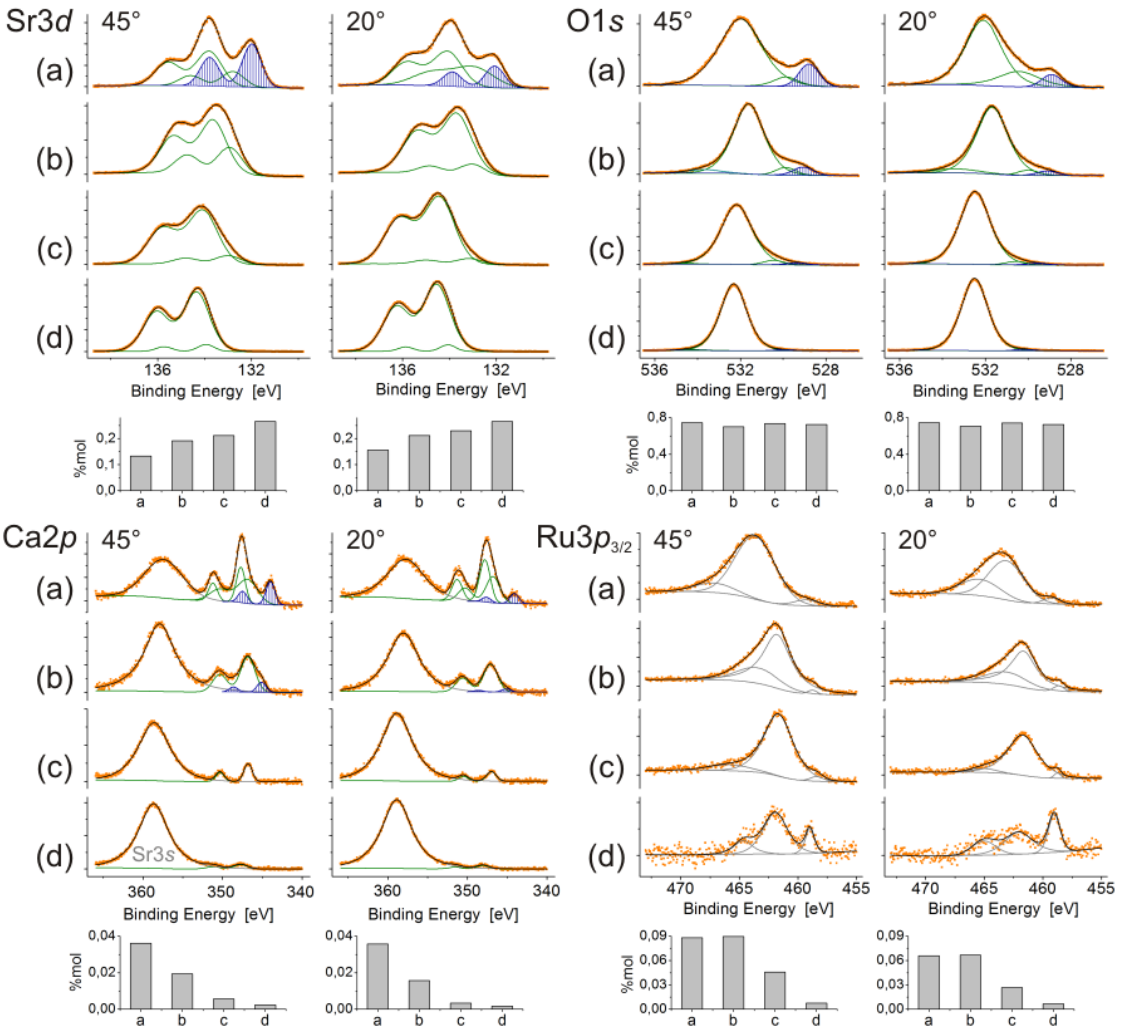

Figure 54
XPS core spectra for Sr, Ca, O and Ru taken at two analysis angles (45° and 20°). Individual lines or doublets fitted to the spectra are presented and perovskite lattice contribution (blue) distinguished from the one coming from surface compounds (green) wherever possible. Column graphs show evolution of stoichiometry of the observed region.

$Sr_{0.6}Ca_{0.4}RuO_3$
thin film deposited on $SrTiO_3$,
(a) as-made sample,
after 1/2 hour annealing under oxygen pressure below 10^{-5} mbar at a temperature of:
(b) 500 °C,
(c) 600 °C,
(d) 700 °C.

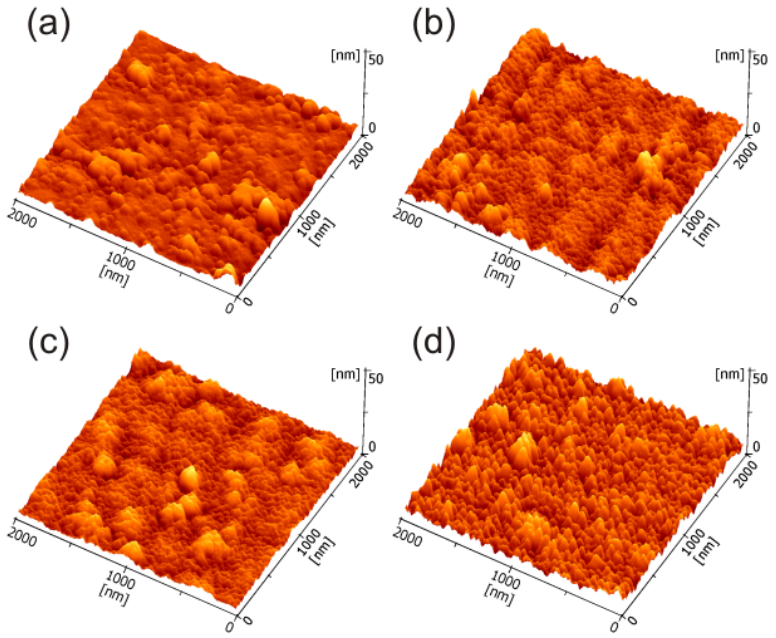

Figure 55
AFM topography images. After deposition the sample was stored for several days before annealing (a).

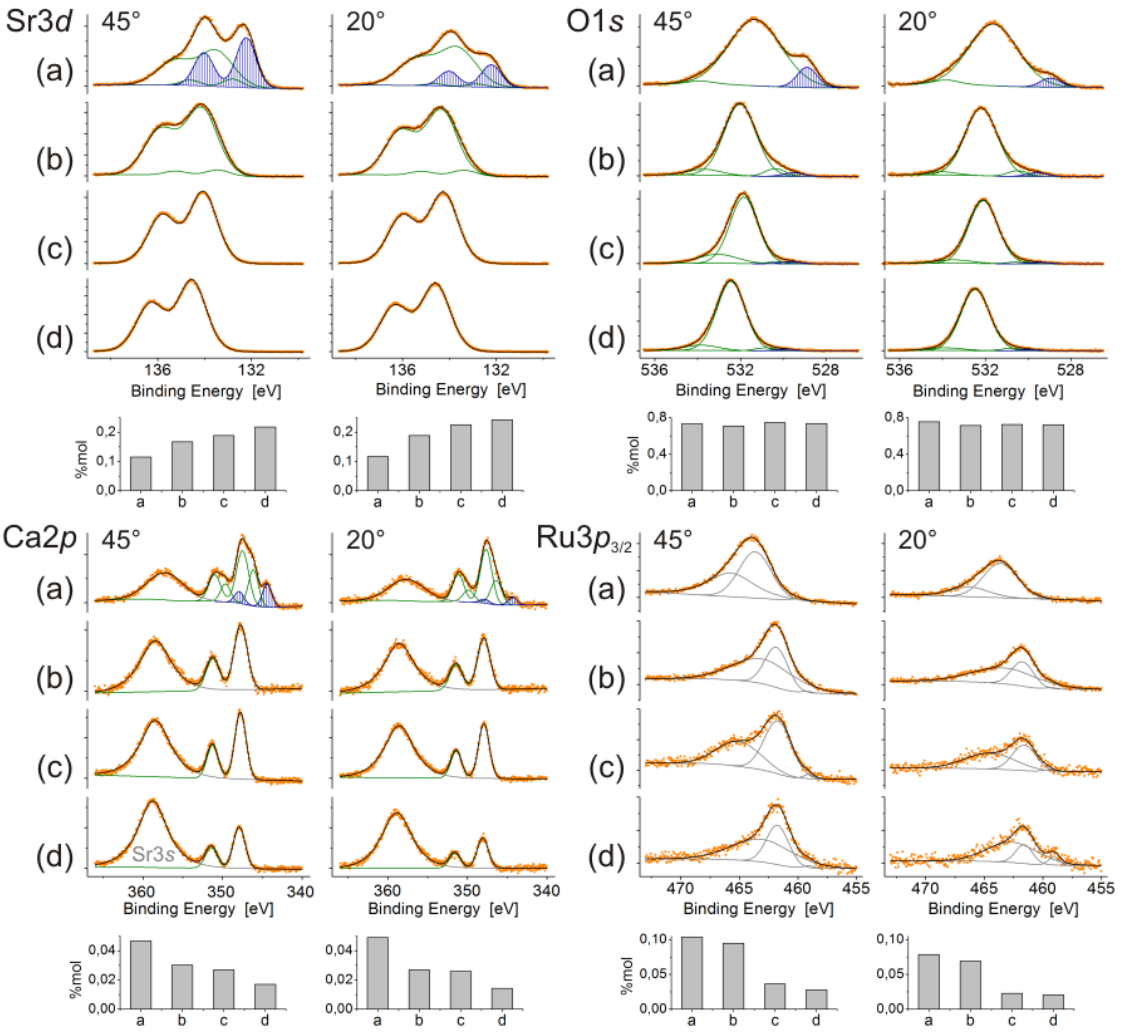

Figure 56
XPS core spectra for Sr, Ca, O and Ru taken at two analysis angles (45° and 20°). Individual lines or doublets fitted to the spectra are presented and perovskite lattice contribution (blue) distinguished from the one coming from surface compounds (green) wherever possible. Column graphs show evolution of stoichiometry of the observed region.

5. Discussion

The $Sr_{1-x}Ca_xRuO_3$ thin films were prepared with HPS using pure oxygen as a sputtering gas. The lowest pseudo-cubic lattice parameter mismatch with the $SrTiO_3$ single crystal typically used as the substrate was estimated for Ca content within a range of $0.2 \leq x \leq 0.4$. Therefore the $Sr_{0.8}Ca_{0.2}RuO_3$ and $Sr_{0.6}Ca_{0.4}RuO_3$ compounds were chosen for their expected improved structure quality over the $SrRuO_3$ thin films, a large area of possible applications and little-known properties. Furthermore, capability of HPS method to produce the samples of these compositions having desired parameters was under consideration. Applied measurement techniques allowed a systematic approach to the undertaken problems beginning with a thorough examination of the reference $SrRuO_3$ composition.

5.1. Growth types

All the $SrRuO_3$ thin films deposited on $SrTiO_3$ displayed topography of the surface preserving atomic steps of the substrate. Even on the exact (100) oriented substrates the observed very low miscut is sufficient to induce the step-flow growth mode with parallel and evenly spaced steps traveling in one direction on the areas as large as 10×10 nm^2 (p. 21, fig. 11). The surface of each step was usually large enough to support nucleation of 2D islands and trigger a local layer-by-layer growth mode. The steps had a height of one pseudo-cubic lattice cell and extremely low rms roughness with no step bunching ever observed. Most of the samples grew in the pure 2D mode while other developed additional 3D islands protruding from the otherwise flat surface. The islands were round and tens of nanometers high but had no other distinctive features therefore at this stage of work their origin remained unknown.

Consistently, a complete XRD analysis showed very good crystal structure of the thin films with no islands observed (p. 21, fig. 9 and 12). The rocking curves were very narrow and only slightly wider than the rocking curves of the substrate, the intensities of the peaks high, the Laue oscillations distinct. The in-plane pseudo-cubic lattice constant was similar to that of the substrate, the cell volume comparable with that of the bulk material.

The results obtained from both AFM and XRD measurements characterized the samples without the 3D structures as the highest quality crystals. The values of all the parameters commonly used as quality indicators fell within the best limits defined in the literature so far, regardless of the deposition technique used or the details of the procedure. Since this was the technological aim of the thesis only these samples were further examined.

The RBS analysis (p. 23, fig. 15) partly confirmed the above findings showing a minimum ratio of the backscattering yield χ_{min} of 2.2% comparable to the value of 1.9% reported for the high quality $SrTiO_3$ single crystal[105]. Surprisingly, however, the Ru/Sr cationic ratio derived from the best computed approximation of the random mode spectrum of the same sample was only 0.84. Further detailed examination with TOF-SIMS (p. 23, fig. 16 and 17) showed that the thin film was laterally homogeneous down to 300×300 nm^2 areas but revealed significant Sr enrichment in both, the surface and the interface. Considering that each deposited sample showed the features of an epitaxial single crystal the most probable is that the interface incorporated additional SrO layers in the standard alternating SrO-RuO_2 layer structure, which indicates occurrence of different RP phases. Similar planar defects, recognized as a double SrO layer were discovered by Jia *et al.*[106] at the $BaTiO_3/SrRuO_3$ interface, formed at the temperature of 800 °C and oxygen pressure of $2\cdot10^{-3}$ mbar.

Two kinds of substrate materials, $SrTiO_3$ and $LaAlO_3$, were used for a preparation of the $Sr_{0.8}Ca_{0.2}RuO_3$ and $Sr_{0.6}Ca_{0.4}RuO_3$ thin films. Potentially, in spite of a worse structural compatibility, in a testing procedure $LaAlO_3$ could offer some advantages over $SrTiO_3$. Larger lattice mismatch was expected to prevent overlapping of (00*l*) peaks of the substrate and the thin film in θ-2θ XRD scans (observed by other authors[88,90]). Lack of Sr signal from the substrate should make RBS spectra much easier to analyze and thus allow much more accurate stoichiometry estimation. Besides, successful utilization of the $LaAlO_3$ substrate was reported for deposition of both, $SrRuO_3$ and $CaRuO_3$ limiting compounds.

This argumentation turned out to be meaningless. Overlapping of the diffraction patterns did not occur for either of the substrates used. The measured out-of-plane lattice constants for the best obtained samples of $Sr_{0.8}Ca_{0.2}RuO_3$ on $LaAlO_3$, $Sr_{0.8}Ca_{0.2}RuO_3$ on $SrTiO_3$ and $Sr_{0.6}Ca_{0.4}RuO_3$ on $SrTiO_3$ were 4.00 Å, 4.06 Å and 4.07 Å respectively, which are sufficiently larger compared to 3.906 Å for $SrTiO_3$ and 3.792 Å for $LaAlO_3$.

Unfortunately, it was not possible to grow a flat and uniform $Sr_{0.8}Ca_{0.2}RuO_3$ thin film on $LaAlO_3$ regardless of the deposition temperature, the oxygen pressure, target-substrate distance or the sputtering

current used. The thin films consisted of grains, clearly observed at the AFM scans (p. 29, fig. 22). The topography was similar in the whole range of deposition parameters, only the diameter of the grains systematically increased with the increase of the substrate temperature. The shapes of the XRD rocking curves revealed a presence of epitaxial ordering in the thin films but at the same time a large amount of poorly oriented material (p. 29, fig. 23 and 24). The thin films seemed to grow as separate column-like islands, with individual grains epitaxial to the substrate and therefore, most likely in the 3D Volmer-Weber mode. Interestingly, the larger were the lateral dimensions of the grains the lower was their degree of epitaxy. Similar topography features were previously described for $BaTiO_3$ on $SrRuO_3$ / $SrTiO_3$ [107] or Nb-doped $SrTiO_3$ deposited homoepitaxially[108]. Above certain thickness the $BaTiO_3$ thin films accumulated strain energy large enough to allow forming of misfit dislocations and accompanying threading dislocations, which resulted in a macroscopic structure relaxation. This introduced local lattice distortions such as a spiral growth around the threading dislocation and led to incomplete coalescence of nucleated islands[107]. This detailed description allows identification of the intermediate Stransky-Krastanov growth mode. The main difference is that the initial layer-by-layer growth was not observed for our $Sr_{0.8}Ca_{0.2}RuO_3$ samples on $LaAlO_3$. Assuming the deposition rate in the same range as for the samples on $SrTiO_3$ the shortest, 100 min sputtering should produce a thin film having average thickness of about 10 nm. Down to this limit no trace of 2D growth was found. This may be due to the fact that in comparison to $SrTiO_3$ the twinned $LaAlO_3$ single crystal substrates contain a larger concentration of threading defects. The atoms along the dislocation have unsaturated chemical bonds and thus an excess of energy reducing the kinetic barriers and locally facilitating the mass transfer[109] which promotes the growth of 3D islands. The dislocations forming as a result of Ru deficiency could additionally support this type of growth.

The XRD analysis pointed out two possibilities of the relaxation of the structure. The samples deposited in low temperatures contained small highly ordered grains and most of the strain was released in the grain boundaries. Deposition in the high temperatures reduced the total area of the boundary regions but at the same time the strain relaxation caused a significant disorder inside the grains. In both reported cases of the similar growth the grain boundaries were Ti-rich and their stoichiometry was different than that of the grain centers and therefore the thin films were discussed in terms of a two-phase system. In case of our $Sr_{0.8}Ca_{0.2}RuO_3$ thin films on $LaAlO_3$ it can be assumed that the grain boundaries were Ru deficient. Ru vacancies would break the conduction paths between RuO_6 octahedra and could explain lack of the macroscopic conductivity observed for our samples. Nonconductive grain boundaries would act as an insulation coating of their core region.

When switching from $LaAlO_3$ to $SrTiO_3$ substrate one may expect the disorder caused by a structural relaxation to lessen, due to the decrease of the lattice misfit.

The topography of the $Sr_{0.8}Ca_{0.2}RuO_3$ thin films on $SrTiO_3$ was nearly the same as that of the $SrRuO_3$ reference layers. Again all the produced samples were divided in two groups, those forming by the step-flow mode enhanced by the layer-by-layer nucleation on the steps with no step bunching and a very low roughness and the ones with a various number of overgrown 3D islands (p. 31, fig. 26 and 28). A transition between the 2D and 3D modes did not seem to be induced by a change of any of the deposition parameters but the islands were observed only for thicker films (above 30 nm). The 3D structures were all similar in shape and slightly lower and more laterally extended than for the $SrRuO_3$ thin films. In several cases their spiral form consisting of atomic steps was clearly resolved. Similar spirals were noticed before[34] for PLD grown $SrRuO_3$ thin films. The threading dislocations, suitable as their nucleation centers may be present on the surface of the substrate or more probably, appear in the thin film as a result of the strain release or formation of the clusters of Ru vacancies. This mechanism has been already discussed for the thin films deposited on $LaAlO_3$. The main difference is the possibility of getting a 40 nm thick sample with no trace of the 3D islands. It can be assumed that the relaxation through the misfit dislocations starts above a certain thickness but is not only thickness dependent. It is known that $SrRuO_3$ thin films on $SrTiO_3$ release a very little amount of the substrate-induced strain and very thick but still fully strained films can be easily obtained[110]. Substitution of strontium with smaller calcium ions changes Ru-O-Ru bond angles introducing a local lattice disorder. This should facilitate the relaxation but at this level of Ca-doping our samples grown in a 2D mode showed no evidence of the strain being released with increasing distance from the substrate.

Both groups of the samples were fully characterized with XRD (p. 31, fig. 25 and 27). The purely 2D grown thin films had rocking curves nearly as narrow as the $SrTiO_3$ substrate, while the mixed type of growth was reflected in additional wide component. The simplest assumption that the wide part of the rocking curve comes from the poorly epitaxial 3D structures is in agreement with the hypothesis of their spiral growth.

The quality of the $Sr_{0.8}Ca_{0.2}RuO_3$ thin films grown on $SrTiO_3$ in the 2D mode, as indicated by AFM and XRD parameters, was similar to that of the $SrRuO_3$ reference composition. Therefore these samples were subjected to further analysis. The RBS measurements (p. 33, fig. 30) revealed that although the minimum yield ratio χ_{min} below 5% confirmed a very good lattice ordering the Ru/Sr cationic ratio was lower than 0.7, hence, the instoichiometry was twice as large as calculated for the $SrRuO_3$ samples. Once more the TOF-SIMS depth profile showed the deviations from the average cationic ratio only in the interface and the surface (p. 33, fig. 32).

When the Ca content was increased from $x = 0.2$ to 0.4 properties of the thin films significantly worsened, in spite of the fact that the lattice mismatch with the $SrTiO_3$ substrate remained very low. The surface topography of the $Sr_{0.6}Ca_{0.4}RuO_3$ thin films was quite different (p. 41, fig. 37). Every sample consisted of irregularly shaped, partially coalesced islands, occasionally forming larger, elongated structures. Although the atomic steps were not observed, the XRD θ-2θ scans clearly displayed the crystal lattice reflections of moderate intensity (p. 41, fig. 36 and 38) including, in some cases, the Laue oscillations. These are the features of the highly ordered material of a very uniform thickness. Moreover, these samples contained only one, epitaxial crystal phase. The best obtained rocking curves consisted of a single, narrow line but comparing to the $SrRuO_3$ reference thin films additional background appeared and the line was slightly wider. Together with a much higher RBS minimum yield ratio it reveals a presence of a disordered phase, possibly a very poorly oriented or even amorphous compound situated between the epitaxial 3D islands.

5.2. Stoichiometry

Both thin films possessing several features of a single crystal, namely $SrRuO_3$ on $SrTiO_3$ and $Sr_{0.8}Ca_{0.2}RuO_3$ on $SrTiO_3$ at the same time showed obvious variations of stoichiometry along the out-of-plane axis. The average value of the Ru/A (A = Sr, Ca) cationic ratio found with RBS was very low in both cases. The same ratio observed in the TOF-SIMS depth profiles was constant in the inner regions of both thin films except that it started with much lower values at their surfaces and again sharply dropped in the interfaces. One should be careful when interpreting these results since the removal rate may be altered by a different structure of the boundary regions and at the surface additionally affected by a presence of contaminants. Therefore the surfaces were further examined with XPS and an HRTEM image was taken for the $Sr_{0.8}Ca_{0.2}RuO_3$ thin film. Nonetheless, the assumption of the constant removal rate allowed certain quantitative estimations for the Ca-doped sample.

The TOF-SIMS depth profile of the $Sr_{0.8}Ca_{0.2}RuO_3$ composition showed that in the interface region the amount of A-type atoms removed during one sweep more than two times exceeded the nearly constant value measured for the interior of the thin film (p. 33, fig. 32). Accordingly, the number of the Ru atoms collected at the same sweep decreased. Since the estimated thickness of this border layer was about 3 nm the accumulated excess of Sr and Ca atoms was found to be significant. Consistently in the HRTEM image the interface region was clearly distinguished as several monolayers having different periodicity (p. 37, fig. 35), possibly RP-phases, although their total thickness did not seem to be as large as given above.

XPS analysis confirmed expected compositional irregularity at the surface for both, the $SrRuO_3$ and $Sr_{0.8}Ca_{0.2}RuO_3$ thin films. In both cases the very upper layer was nearly ruthenium free and the Ru/A ratio increased with sample depth. This disorder possibly reached as far as few nanometers deep into their perovskite structure. Approximated by the bilayer model, the surface layer of the $SrRuO_3$ reference thin film shortly after deposition was about 1 nm thick and nearly the same for the fresh Ca-doped sample.

The estimated Ru deficiency in the surface and the interface region alone is sufficient to explain the average Ru/A ratio even as low as 0.7 without assuming any nonstoichiometry in the inner layers of the thin film. Therefore instead of a description in terms of a perfect monocrystal structure a model can be proposed in which both kinds of thin films are Sr-O terminated, incorporate a large number of Ru vacancies in the near surface region gradually approaching the nominal composition in the interior and have a significant surplus of the Sr-O layers in the interface. This is quite different from the bulk structure where a presence of numerous Ru vacancies leads to a formation of the superlattice (RP-phase with $n < \infty$). Although the excessive and extended in time process of aging occurring in our thin films may be related to the reshuffling of the planar boundaries which is kinetically very slow no evidence of superlattice formation was ever found in the interior of the thin films. Moreover, the process seemed to proceed in the opposite direction, i.e. the Ru vacancies traveled towards the surface and the interface of the thin layer. We expect the change of the boundary conditions related to the presence of the substrate to play a key role in this phenomenon.

A much lower, RBS measured Ru/A ratio of 0.5, found for the $Sr_{0.6}Ca_{0.4}RuO_3$ thin films (p. 43, fig. 39) is definitely reflected in their different topographical and structural features. Clearly, such a Ru deficiency can no longer be accommodated in a monolithic layer. A larger distortion of a structure possibly decreased a number of nucleation sites suitable for ruthenium adatoms, especially at the areas where the nucleated epitaxial islands should merge together. This led to incomplete coalescence of the islands (see figure 37 at page 39 or figure 43a at page 45). The regions in between were subsequently filled with a poorly ordered and Ru scarce material.

Table 11
Magnitudes of the pseudo-cubic out-of-plane lattice constant.

Thin film (on $SrTiO_3$)	Out-of-plane lattice constant	
	predicted $\frac{V_{bulk}}{(a_{STO})^2}$	measured
$SrRuO_3$	3.96	3.95 - 3.96
$Sr_{0.8}Ca_{0.2}RuO_3$	3.93	4.04 - 4.10
$Sr_{0.6}Ca_{0.4}RuO_3$	3.88	4.01 - 4.08

5.3. Out-of-plane lattice constant

The aim to produce epitaxial thin films was achieved for every $Sr_{1-x}Ca_xRuO_3$ composition under investigation and both utilized substrates. The in-plane lattice constants derived from the 2D reciprocal space maps of the samples deposited on $SrTiO_3$ were less than 0.2% higher than that of the substrate, regardless of the Ca content (x = 0, 0.2 or 0.4). The out-of-plane atomic distances measured were collected in the table 11 compared to the ones predicted using tetragonal lattice cell parameters for the bulk materials. The values obtained for the $SrRuO_3$ reference thin films grown under optimal conditions nearly perfectly matched the predictions and were highly reproducible. For both Ca-doped compositions (x = 0.2 and 0.4) on $SrTiO_3$ a good epitaxy was always accompanied by an elongated out-of-plane lattice constant, regardless of the deposition parameters used. In case of the thin films with x = 0.2 the higher deposition temperatures produced the larger out-of-plane distances with a calculated rate of about 0.037 Å per 100 ºC (p. 31, fig. 29). The elongation occurred whether the expected substrate-induced strain was compressive (x = 0.2) or tensile (x = 0.4). This tendency, observed also in both limiting compositions (x = 0 and 1) of thin layers investigated by other authors, requires broader discussion as it is expected to strongly affect other physical properties.

Values of the out-of-plane lattice constants in the range of 3.98-4.00 Å were measured for pure $SrRuO_3$ thin films if the oxygen pressure was kept below 0.02 mbar during the deposition (PLD)[111]. The authors linked the elongation with a drop of the ferromagnetic Curie temperature T_C and explained both effects with a presence of Ru vacancies. Reduction of the oxygen pressure to the range of 10^{-6} mbar resulted in the atomic layers being moved apart above 4.09 Å for 11 nm thick sample, which in this case was attributed to an ion bombardment during the growth process[112].

Two types of structure were reported for the second limiting composition, $CaRuO_3$, both deposited on $SrTiO_3$ by 90º off-axis sputtering under identical conditions[46]. The one with the lattice parameters similar to those of the bulk material displayed a poor mosaic structure characterized by broad XRD rocking curves, while a good epitaxial growth was accompanied by an out-of-plane expansion up to 3.97 Å (from expected 3.72 Å), in spite of a tensile strain, and a change of electrical behavior from metallic to semiconductive. Considering that RBS measured Ru/Ca ratio was about 0.62 for epitaxial samples, the authors attributed their different structures and properties to a strain induced Ca^{2+} partial substitution of smaller Ru^{4+} cations. This thesis extends the field of investigation to samples of intermediate compositions.

The samples with x = 0.2 and x = 0.4 in spite of their obvious morphological differences were grown with the out-of-plane lattice constants in a similar range. Moreover, in the case of x = 0.2 HRTEM scan showed a very uniform atomic spacing through the whole interior of the thin film (p. 37, fig. 35). It is possible to verify the HRTEM results using the Williamson-Hall method[113,114] of microstrain analysis. Within this method the microstrain ε is defined as the average relative deviation of the distance between atomic planes:

$$\varepsilon = \frac{\langle \Delta d \rangle}{d}$$

According to Williamson and Hall ε is reflected in the widths of the XRD θ-2θ peaks and can be obtained from the formula:

$$\beta_Q = 2\varepsilon Q + \frac{1}{D}$$

where β_Q is the total integral peak width in the reciprocal space, Q describes planes separation also in the reciprocal space and D is a mean linear dimension of the grain under investigation. The analysis was performed for the (00*l*) reflections of both compositions and additionally for the reference ($x = 0$) layers. Example data presented for the $Sr_{0.8}Ca_{0.2}RuO_3$ thin films (fig. 57) confirm a linear relationship between β_Q and Q. The ε values estimated for the reference samples did not exceed 0.05%. In the Ca-doped thin films the microstrain was larger but still well below 0.5% and in several cases as low as 0.1%, regardless of Ca content. Assuming that the substrate-induced strain is gradually released with the distance from the substrate one would expect an in-depth variation of the out-of-plane lattice parameter and thus some increase of ε with the sample thickness. However, no correlation of any type was found. The results were therefore consistent with HRTEM imaging. It is interesting that in every investigated case the out-of-plane grain length obtained with the same formula was comparable with the layer thickness. This indicates that the diffraction is coherent over the whole depth of the thin film.

All the above findings suggest a fairly homogeneous and fully strained lattice with a low degree deformation coming from atomic vacancies or other structural defects. Considering that Ru atoms display a broad spectrum of different oxidation states one should expect a certain amount of oxygen vacancies present in the structure. In comparison, oxygen vacancies introduced to a similar perovskite structure of a $SrTiO_{3-\delta}$ ($\delta = 0.5$) thin film induced a much higher microstrain of about 1-2%[115]. Therefore we believe that the concentration of these defects in our thin films was much lower. Our composition with $x = 0.2$ displayed a negative thermal coefficient of electrical resistivity, which could be indicative of Ru vacancies if it were coexistent with a drop of magnetic transition temperature T_C. However, values of 126 K obtained from the change of resistivity gradient (fig. 59b) and 101 K from the inflection point of magnetization (fig. 59c) remained very high. Furthermore, composition analysis showed that except for the interface and the surface regions the samples with $x = 0.2$ were nearly stoichiometric. From this point of view the disorder caused by vacancies or other point defects is not likely to be strong enough to cause the elongation of the out-of-plane lattice constant.

Since the explanations of the observed changes of the lattice parameters given in the literature are not sufficient, it could be valuable to examine once again the assumption of the rigid RuO_6 octahedron. It is known that ruthenium oxides are volatile and our results confirm that a thermal treatment of $SrRuO_3$ leads to ruthenium loss even in the temperatures as low as 500 ºC and regardless of oxygen content in an ambient atmosphere. Figures 41 and 43 show an evolution of surface morphology of the $Sr_{0.8}Ca_{0.2}RuO_3$ and $Sr_{0.6}Ca_{0.4}RuO_3$ thin films after long term storage under normal conditions. Clear changes result from excessive reactions with adsorbates. Moreover, XPS measurements showed a significant decrease of Ru content in the surface which is an indication of a segregation process or possibly ruthenium loss. Considering all the above, the stability of the RuO_6 octahedra seems questionable. A length of a Ru-O bond in the $ARuO_3$ (A = Sr, Ca) structure falls in the range from 1.97 to 2.01 Å and reaches 2.05 Å for a $LaRuO_3$ perovskite[3]. The RuO_6 octahedron is strongly deviated from a regular shape, even in the bulk form of these compounds. A substrate induced strain may further increase this deformation[85].

Therefore the lattice parameters of our thin films with $x = 0.2$ and $x = 0.4$ may be specific for a new crystallographic phase. Interaction with a substrate would suppress the tilt of the octahedra existing in the bulk and instead force their expansion along the out-of-plane axis.

Nevertheless, the detailed reason for the difference between the volume of the thin film lattice cell and the one predicted from the bulk remains unclear. Furthermore, it is interesting to notice that the thin film adopts its crystallographic form on top of the compositionally disturbed and rather poorly ordered interface layer. Hence the exact role of the substrate in the thin film ordering requires further investigation.

5.4. Valence band spectra

The valence band spectra measured with XPS were nearly identical for every investigated as-made sample on the $SrTiO_3$ substrate, regardless of the Ca content ($x = 0$, 0.2, 0.4) or the analysis angle (fig. 60). A high intensity photoelectron signal was observed with binding energies of the electrons spreading continuously down to the Fermi edge. The first and second maxima were found at about 1 eV

and 6 eV. This shape was partly consistent with the theoretical DOS calculations by other authors and the maxima were attributed, respectively, to the Ru4*d* t_{2g}-O2*p* antibonding and bonding states. Subtraction of the spectra of the $SrRuO_3$ thin film at two different analysis angles allowed us to remove most of the surface contribution and revealed the third feature, centered at about 3.4 eV. We believe it to be the missing O2*p* nonbonding states contribution. Our results in comparison with theoretical predictions[116,117] are shown in the figure 58.

The deformation of the lattice cell described for the $Sr_{0.8}Ca_{0.2}RuO_3$ and $Sr_{0.6}Ca_{0.4}RuO_3$ thin films on $SrTiO_3$ did not change the main features of their valence bands. The first maximum moved slightly further from the Fermi level and accordingly the slope between occupied and unoccupied states became less steep. The third maximum was not observed even after the subtraction of the spectra.

Lack of the gap in the valence band spectra predicted by the calculations was not surprising. The gap was never observed in the experimental work done by other authors, since the Ru4*d* t_{2g}-O2*p* antibonding band measured with photoelectron spectroscopy in a wide range of incident photon energies[77,78,83,89,117] was in every case much broader than the calculated one. This is usually explained by the transfer of the spectral weight from the so-called coherent part near the Fermi level to the incoherent one situated at higher energies due to the electron correlations[78]. In case of $SrRuO_3$ it was shown[86] that such a widening of the band can be reproduced theoretically by adding a small Hubbard on-site repulsion term. The transfer to the incoherent part is predicted to be enhanced by the Ca doping[89] due to increasing lattice distortion. The expected energy cost of doubly occupied site (U), however, is not large enough comparing to the width of the individual t_{2g} band (W)[84] to induce a metal-insulator transition ($U/W > 1$), regardless of the Ca content.

Accordingly, the valence band spectra displayed a clearly metallic character for all three compositions, although the room temperature electrical resistivity of $Sr_{0.8}Ca_{0.2}RuO_3$ was about 5 times higher than that of $SrRuO_3$, for the best obtained samples, and the $Sr_{0.6}Ca_{0.4}RuO_3$ samples were macroscopically nonconductive. The worsening of the conductivity cannot be simply explained by a described spectral weight transfer, as a character of distortion in our Ca-doped samples is clearly different from that observed in the bulk. Nonetheless, the elongation of the Ru-O bonds in the out-of-plane direction has some impact on electric properties, weakening the Ru4*d* and O2*p* orbitals overlapping and lowering the effectiveness of conduction paths between the RuO_6 octahedra.

When Ca-doping was increased to $x = 0.4$ the conduction paths were entirely broken in the regions were the 3D islands did not merge together which led to a complete suppression of macroscopic conductivity.

5.5. Surface region

One should consider also the role of the Ru-deficient surface region on the macroscopic properties of the thin film. The conductivity of this region dependent on the number of conduction paths is expected to grow with increasing distance from the surface, which is additionally covered with a thick insulating layer of adsorbates. The atomic disorder in the surface region was pointed out before[86] as a possible reason for the metal-insulator transition.

The LC-AFM analysis of the $SrRuO_3$ thin film surface showed lateral areas of different conductivity (p. 25, fig. 19 and 20) and proved that a change of its character and magnitude is possible by applying voltage exceeding certain thresholds. The process of a transition from a low to a high conductivity state can be explained by electrically stimulated partial chemical decomposition of the adsorbed layer at first, but with increasing voltage also the decomposition of the first monolayers of the $SrRuO_3$ lattice. When a bias voltage of about -3V (grounded tip) was used holes of few nanometers depth could be obtained. Unfortunately the electrochemical reaction was destroying a conductive coating of the AFM tip as well.

In spite of the nonconductive cover the whole area of the surface was easily scanned with STM. Among other features the images revealed a presence of weakly bound and soft formations of adsorbates decomposing under the applied voltage as low as 30 mV, possibly SrO-OH compounds (p. 25, fig. 21).

The idea that cations at the surface of the thin film may react with water, forming hydroxides, which readily decompose in the electric field was proposed before. It is possible to remove the $YBa_2Cu_3O_{7-\delta}$ thin films locally using a STM tip and a bias voltage of 1.5 V[118]. In case of the $SrTiO_3$ thin films, ridges of several nanometers high were formed using a conductive AFM tip and a negative bias voltage in the range of 10-30 V[119]. In both cases transport of large amounts of material was thought to be possible due to the formation and decomposition of $Ba(OH)_2$ and $Sr(OH)_2$ respectively.

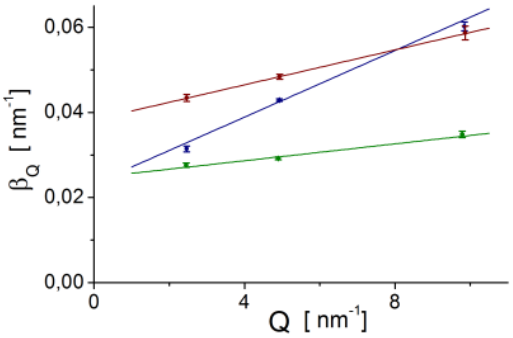

Figure 57
Example Williamson-Hall plots (widths of the θ-2θ peaks vs corresponding atomic planes spacings in the reciprocal space) for $Sr_{0.8}Ca_{0.2}RuO_3$ thin films on $SrTiO_3$.

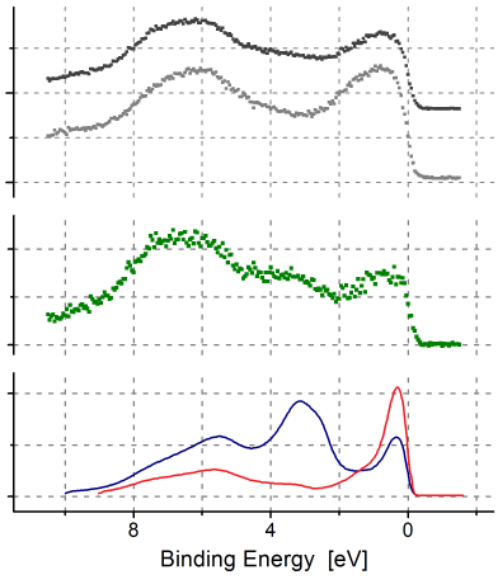

Figure 58
XPS valence band spectra of an as-made $SrRuO_3$ thin film on $SrTiO_3$ measured at the analysis angle of 50° (dark gray), 10° (gray) and their subtraction (green) exposing valence band of the thin film interior. Calculated O2*p* (blue) and Ru4*d* (red) partial DOS for $SrRuO_3$ /Ref. 117/.

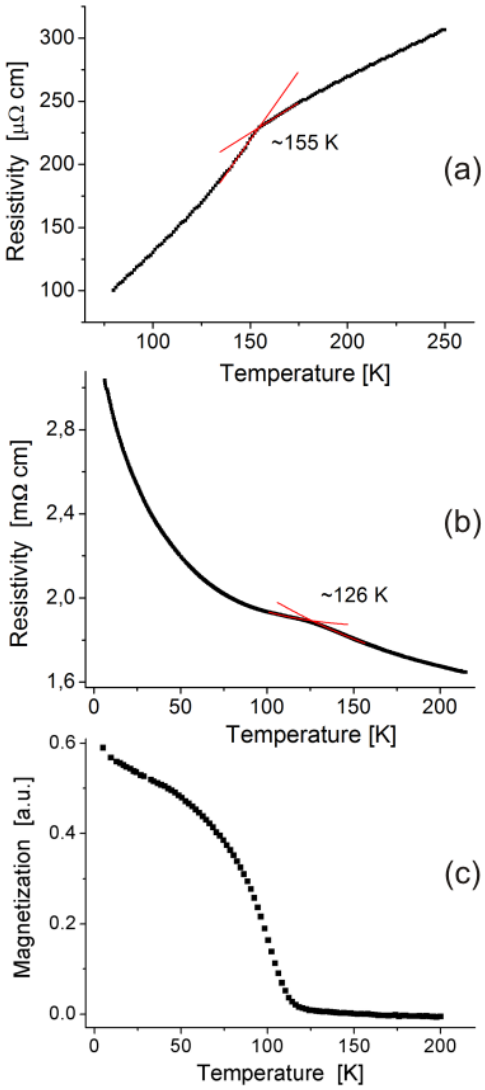

Figure 59
Resistivity (a) of a $SrRuO_3$ thin film on $SrTiO_3$, resistivity (b) and magnetization (c) of a $Sr_{0.8}Ca_{0.2}RuO_3$ thin film on $SrTiO_3$ as a function of temperature.

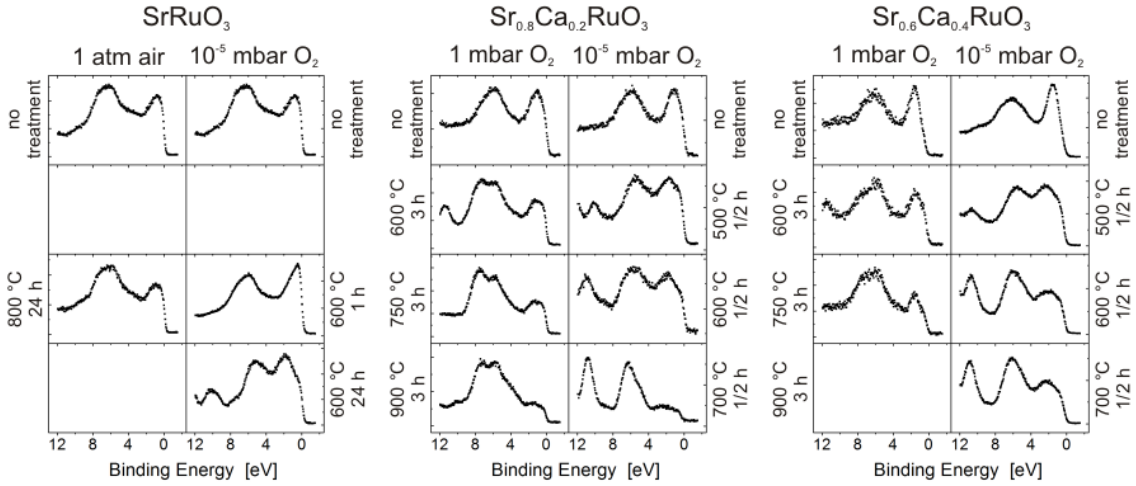

Figure 60
XPS valence band spectra evolution after oxidation and reduction. All the presented spectra were measured for the thin films deposited on $SrTiO_3$ at the analysis angle of 45°.

At first glance the difference between STM and LC-AFM results is surprising. Using STM it was possible to obtain any tunneling current in the range of 100-1000 pA at every scaned surface point, applying a voltage lower than 0.1 V. With LC-AFM and a voltage lower than 1 V there existed large surface areas where obtained current was below the measurement limit that is lower than 10 pA. To explain it one has to focus on different geometries of both types of measurements. A LC-AFM conductive tip is in contact with the material, which is the conductive $SrRuO_3$ thin film, mixed at the surface region with nonconductive contaminations. When the tip touches the adsorbate layer almost all the potential drops across this layer[120]. Polarized dielectric becomes a large potential barrier for the electrons. A STM conductive tip is separated from the material by a vacuum or air gap. In this case most of the potential drops across the gap and a contamination layer is much less polarized which makes the potential barrier lower. Also the electrons approaching the surface have a relatively high kinetic energy. It makes the electron transport in the case of STM much easier and weakly dependent on the thickness of a contamination layer, while for LC-AFM at a certain applied voltage only these regions are accessible which are uncovered or have a contamination layer thin enough to allow tunneling. A direct electrical contact forms mainly as a result of the electrochemical reaction at the least contaminated areas under relatively high applied voltage.

Considering that modern technological applications turn to the thin films of the lowest thickness at which required properties of the bulk are still preserved (so-called critical thickness) the in-depth heterogeneity and the surface disorder become of highest importance and should be carefully addressed.

Deepening with time deterioration of both, surface topography and morphology, observed for our samples, further limits their possible utilization as a bottom layer. The detailed analysis showed that the $Sr_{1-x}Ca_xRuO_3$ thin films ($x = 0.2,\ 0.4$) stored for several months underwent a process of atomic rearrangement. The phase diagrams of polycrystalline $SrRuO_3$ [121] and $CaRuO_3$ [122] show that normal storage conditions can be seen as moderately oxidizing but far from optimal for the formation of RuO_4 [73]. Furthermore, although the average Ru/A (A = Sr, Ca) cationic ratio measured for our thin films was too low to assure stability of the $ARuO_3$ polycrystalline compound the XRD θ-2θ scans did not change after long-term storage regardless of Ca content and the peak centered at 2θ of about 22º was indicative of $ARuO_3$ phase. No formation of other RP-phases was confirmed. Therefore it can be assumed that the rearrangement had a chemical rather than thermodynamic character.

The atoms at the non-contaminated surface do not usually occupy the positions fixed by the three-dimensional lattice. The forces induced by the broken oxygen-cation bonds may cause structural distortions of different types, the most frequent being relaxation, rumpling and reconstruction. Relaxation is a change of the spacing between the uppermost atomic planes, rumpling occurs when the cations and oxygen anions move in opposite out-of-plane directions and usually shifts oxygen outwards and reconstruction is a change of the periodicity of the outer layer[123]. Such a distorted surface is subsequently subjected to the interactions with the ambient species, mostly of van der Waals character.

All the AFM imaged surfaces of the aged samples were covered with a thick nonuniform layer of contaminations including carbon adsorbed from the ambient atmosphere (p. 47, fig. 41b and 43b). The signal of the lattice component significantly dropped in the XPS Sr3*d* and O1*s* spectra (p. 47, fig. 42). The Sr/Ru cationic ratio calculated from the spectra measured for the fresh and aged $Sr_{0.8}Ca_{0.2}RuO_3$ thin films at the analysis angle of 45º was nearly the same (1.7-1.8). That eliminated segregation of SrO and RuO_2 planes in the interior of the thin film or ruthenium oxide loss on the surface as the main factors leading to the surface rearrangement. However, at the analysis angle of 20º the Sr/Ru ratio changed from about 1.9 for the fresh sample to 2.4 for the one long-term stored. Therefore it can be assumed that in the near-surface region Sr atoms segregated to the surface. It is consistent with the observed change of the bonding character for the Sr and O atoms and furthermore, reflects in the widening of the surface region. The shift of the center of the O1*s* surface component by 1.4 eV to higher binding energy indicated that the adsorbates were gradually incorporated in the structure of the thin film. Presumably physisorbed contaminates, namely H_2O and CO_2, progressively established stronger chemical bonding as they slowly migrated inside the surface region. Similar process, although much weaker, was observed for $SrTiO_3$ single crystals[124]. At room temperature the surface of $SrTiO_3$ is expected to be covered with comparable amount of H_2O and CO_2.

Such an excessive aging process of the $Sr_{1-x}Ca_xRuO_3$ thin films raises a question of their stability at elevated temperatures and different oxygen partial pressures, including the role played by the surface contaminations. It is especially important considering that a subsequent deposition of another compound requires specific ambient conditions and a presence of contaminations may disturb the structure of the newly forming thin layer.

The results of annealing showed that the stability area of our $SrRuO_3$ thin films in the space defined by the temperature and oxygen partial pressure was much smaller than the one described in the phase diagram for a polycrystalline compound[121]. The treatment under conditions regarded as being within the stability region led to significant changes not only at the surface but also in the interior of the thin film. Calcium doping further narrowed down the usable range of temperature and pressure. Vacuum in the range of 10^{-5} mbar was sufficient to cause reduction of ruthenium even at the temperatures as low as 500 ºC whereas substantial ruthenium loss during annealing in 1 mbar of oxygen indicated possible formation of RuO_4 at 900 ºC.

The samples of all the investigated compositions ($x = 0$, 0.2 and 0.4) on the $SrTiO_3$ substrate annealed under both, oxidizing and reducing conditions suffered from the significant Ru loss at the surface region (see pages 49-53, 57-59). Before the treatment the Ru atoms were not fully oxidized and annealing in oxygen rich environment improved this situation only slightly, while vacuum annealing produced a large number of the low oxidation states including metallic ruthenium. Long-term reduction left only metallic ruthenium at the surface.

Similar changes of the ruthenium oxidation states were presented before by Hartmann *et al.*[43] for metallic Ru thin films annealed in air and Ohara *et al.*[125] for $Sr(Ti_{1-x}Ru_x)O_3$ thin films annealed in hydrogen. Presented Ru3*d* spectra always consisted of a low binding energy line related to metallic ruthenium and one or more lines, shifted by 1-2.5eV to higher binding energies, related to oxidized ruthenium. During air annealing of the metallic ruthenium, a line related to metal decreased, while oxidized ruthenium line became larger and shifted to higher binding energies[43]. Both metal and oxide lines were very narrow which may indicate existence of only Ru^0 and Ru^{4+} states. Annealing of $Sr(Ti_{1-x}Ru_x)O_3$ in hydrogen caused oxide line to shift to lower binding energies and finally to vanish, while metal line appeared and grew in size[46]. In this case a reduction clearly took place with the presence of intermediate oxidation states.

The relative content of oxygen at the surface region of our samples was very little affected by the treatment, whether the ambient was oxygen-rich or oxygen-scarce. Oxidation clearly triggered a transfer of the O1*s* XPS spectral weight from the higher to the lower energy surface component and when a long-term stored sample was oxidized the lattice component also increased. Accordingly, the Sr3*d* spectra moved to the lower binding energies. Reduction caused a reversed process. After ½ hour treatment the O1*s* and Sr3*d* spectra consisted mainly of the high energy surface components.

Substantial changes were observed also in the valence band spectra (fig. 60). A drop of the part near the Fermi level (Ru4*d* t_{2g}-O2*p* antibonding states), regardless of oxygen content in the ambient was simply a consequence of the ruthenium loss in the surface region. The O2*p* nonbonding part after oxidation moved to lower binding energies and after reduction widened and split in two components. The structure observed at a binding energy of about 11 eV and attributed by other authors to carbon monoxide states[77] appeared after vacuum annealing but also after low-temperature (600 ºC) oxygen annealing.

It should be noted that a short-term reduction of the $SrRuO_3$ thin film at 500 ºC actually improved the measured valence band, surprisingly, increasing the part near the Fermi level (fig. 60).

The topography scans revealed that oxidation destroyed the uniformity of the layers but large epitaxial crystallites remained as indicated by their rectangular shapes (p. 53, fig. 49 and p. 55, fig. 51). At 900 ºC for the $Sr_{0.8}Ca_{0.2}RuO_3$ and 750 ºC for the $Sr_{0.6}Ca_{0.4}RuO_3$ sample the 3 hour treatment partly uncovered the substrate. After a short-term reduction only small precipitations appeared on the flat surface but deterioration progressed with time and the process was faster at higher temperatures (p. 57, fig. 53 and p. 59, fig. 55).

There exist several mechanisms which may be responsible for a described surface rearrangement of our thin films. Szot *et al.*[126] observed changes of the near surface region of $SrTiO_3$ monocrystals annealed in oxygen (270 mbar) at 1000 ºC and in vacuum (10^{-7} mbar) at 950 ºC. The oxidized samples were Sr-enriched at the surface and Sr-scarce in the deeper layers, while the effects of reduction were exactly opposite. According to the authors this inhomogeneity was a result of demixing of the $AO\text{-}BO_2$ structure and a transport of SrO driven by a gradient of the oxygen concentration between the bulk of the crystals and their surface, in contact with low or high oxygen partial pressure in the ambient. Subsequently the excess of SrO was incorporated in the structure by a solid-state reaction, which led to a formation of RP phases, whereas Magnelli phases of Ti_mO_{2m-1} type appeared in the Sr deficient regions. Interestingly, after reduction droplet-like precipitations of SrO were discovered on the surface of fast cooled samples in spite of the general Ti-enrichment of this region.

In comparison with this approach our model of the surface rearrangement of the $Sr_{1-x}Ca_xRuO_3$ thin films should take into account a high degree of adsorbate coverage and a high volatility of ruthenium oxides.

The results consistent with our XPS spectra were obtained by Shin *et al.* [73] for the PLD deposited $SrRuO_3$ thin films annealed in vacuum by steps of 100 ºC up to 800 ºC. The structure of their Sr3*d*, O1*s* and Ru3$p_{3/2}$ reference spectra as well as a ratio between the surface and the lattice parts were similar to ours, even if components were broader and not so clearly separated. In-situ annealing in vacuum shifted the Ru3*p* peak to lower binding energies and lowered the total O/Sr intensity ratio. Lattice and surface components at the Sr3*d*, and O1*s* spectra were still present but the shift to higher binding energies was observed only for the Sr3*d* spectra. The main difference reported was the Ru/Sr intensity ratio, which was constant during in-situ vacuum annealing. However, the starting value of 0.45 was much lower than our ratio of 0.7 and very close to 0.3, which was the lowest value obtained by us for the long-term reduced $SrRuO_3$ thin films. The authors proposed several possible routes for decomposition of $SrRuO_3$ dependent on the annealing conditions:

(1)	oxidation	$SrRuO_3 + O_2 \rightarrow SrO + RuO_4\,(g)\uparrow$
(2)	disproportionation	$2\,SrRuO_3 \rightarrow 2\,SrO + Ru + RuO_4\,(g)\uparrow$
(3)	weak reduction	$SrRuO_3 \leftrightarrow SrRuO_{3-\delta} + \delta/2\,O_2\,(g)\uparrow$
(4)	strong reduction	$SrRuO_3 \rightarrow SrO + Ru + O_2\,(g)\uparrow$

The remaining excess of SrO formed the rock salt layers of the RP phases, whereas metallic Ru separated as nanoparticles. Shin *et al.* addressed also the problem of hydrocarbon contaminates but estimated their thickness to about 1 monolayer and assumed that they were situated on top of the perfect perovskite structure, taking a form of nanograins, similar to those observed by us in the small area STM and LC-AFM scans. A decomposition of the contaminated surface in vacuum started at the temperatures as low as 300 ºC, resulting in appearance of one or two layer deep pits. Reduction above 500 ºC produced the Ru nanoparticles and bulk decomposition occurred above 700 ºC. The samples cleaned by annealing in oxygen/ozone rich ambient were stable in vacuum up to 600 ºC. In 10^{-2} mbar of oxygen/ozone no structural decomposition was observed below 700 ºC.

Complex analysis showed that the disordered region in our $Sr_{1-x}Ca_xRuO_3$ samples extended several nanometers deep into the thin film crystal lattice. Distortion introduced by the Ca substitution on Sr sublattice further weakened the structure and caused a transition from 2D to 3D type of growth for $x = 0.4$. The cover of contaminations reached about 2-3 monolayers after ½ hour exposure to air and more hydrocarbons were slowly adsorbed during the next days of storage. The model of the separate and uniform layer of contaminations on top of the thin film failed to accurately describe the XPS spectra and AFM topography. Most likely physisorbed compounds at first formed weakly bound nanoparticles on top of the perovskite lattice but later progressively diffused into the lattice taking advantage of the Ru vacancies and establishing stronger bonds with the excess AO (A = Sr, Ca) material. At the same time AO moved to the surface using the same migration paths. Possibility of demixing is supported by the discovery of precipitations similar to SrO droplets observed on the $SrTiO_3$ surface. The exact fractions of adsorbed hydroxyls and carbon oxides were difficult to determine but the element ratios calculated for the surface region of the fresh and long-term stored $Sr_{0.8}Ca_{0.2}RuO_3$ samples showed additional 50% of incorporated oxygen atoms. This amount of oxygen excess most probably did not inflict any ruthenium loss or have any influence on the number of O vacancies in the perovskite lattice since neither the Sr/Ru ratio measured at the angle of 45º nor the mixed oxidation states of Ru atoms changed during storage. The adsorption process was highly irreversible therefore we assume that a water-catalyzed reaction of oxygen coordinated Sr with CO_2 led to a formation of stable $SrCO_3$ compound.

The loss of ruthenium during oxidation occurred according to the reaction (1) at low temperatures (600 ºC) and to some extent also to the reaction (2) at higher temperatures (900 ºC) possibly due to the increased mobility of the atoms. Vacuum annealing triggered mostly the reaction (4) and the Ru removal rate was much higher than in case of oxidation at the same temperature. This can be explained if the reduction induces the migration of AO to the interior of the thin film leaving the exposed RuO_2 layers at the surface, like in the case of the $SrTiO_3$ crystal described above. Annealing treatment allowed removing some of the adsorbed contaminations regardless of oxygen partial pressure. Oxidation slightly improved the perovskite lattice near the surface of the aged samples whereas reduction increased the disorder leading quickly to a complete suppression of the lattice component in the XPS spectra. After both types of the treatment the amount of oxygen at the surface region dropped along with the Ru loss and this time no significant increase of oxygen content was observed during long-term storage, i.e. at the XPS spectra taken long after annealing. It seems that the process of adsorption was suppressed. However, one should remember that at this stage the perovskite lattice was no longer observed at the surface region of the reduced samples and the oxidized thin films have lost their uniformity and released most of the substrate induced strain through a formation of rectangular grains.

Therefore, we believe that the surface disorder and Ru deficiency is an intrinsic property of the $Sr_{1-x}Ca_xRuO_3$ epitaxial thin films which leads not only to the formation of RP phases but also greatly increases adsorption of hydrocarbons and thermal as well as electrochemical instability of this region.

6. Conclusions

The $Sr_{1-x}Ca_xRuO_3$ (x = 0, 0.2, 0.4) thin films can be epitaxially deposited on $SrTiO_3$ and $LaAlO_3$ by HPS. Technologically, the main issue that needed to be addressed was a volatility of ruthenium tetroxide. A slow deposition rate and a high pressure of oxygen discharge gas, typical for the HPS technique and usually providing uniform and homogeneous growth of the layers in this case promoted Ru loss. On the other hand the rate of Ru evaporation from the thin film surface was even higher during annealing under low oxygen partial pressure and the disorder introduced to the surface region more substantial. Therefore a selection of optimal deposition method requires further investigation.

Although it was not possible to obtain stoichiometric samples we found Ru deficiency only in the boundary regions, with the interior of the thin film approaching the nominal atomic ratio. We claim that this kind of heterogeneity is characteristic for the $Sr_{1-x}Ca_xRuO_3$ thin films.

These specific structural properties make a description of their quality a complex task. The best obtained $SrRuO_3$ and $Sr_{0.8}Ca_{0.2}RuO_3$ thin films on $SrTiO_3$ grew in the 2D (step-flow) mode reflecting their nearly perfect atomic arrangement. The layers did not show any lateral inhomogeneity down to the areas of 300×300 nm^2. A presence of any instoichiometric phases or a significant concentration of randomly distributed defects in the interior was not confirmed. Consistently, the magnetic transition temperatures were only slightly lower than measured for the polycrystalline samples. The valence band spectra had a clearly metallic character, in accordance with predictions of theoretical calculations carried out by other authors. Nonetheless, the conductivity of the $Sr_{0.8}Ca_{0.2}RuO_3$ samples could be disappointing as indicated by a negative thermal coefficient of resistivity and its room temperature value several times exceeding that of the bulk material. The 3D growth of the $Sr_{0.8}Ca_{0.2}RuO_3$ thin films on $LaAlO_3$ and $Sr_{0.6}Ca_{0.4}RuO_3$ thin films on $SrTiO_3$ led to the appearance of a second, poorly oriented phase, most probably surrounding highly ordered 3D grains. In spite of the presence of the steep Fermi edge in the valence band spectra the samples were macroscopically nonconductive, which was attributed to the influence of the insulating, Ru-scarce grain boundary regions.

The $SrRuO_3$, $Sr_{0.8}Ca_{0.2}RuO_3$ and $Sr_{0.6}Ca_{0.4}RuO_3$ thin films on $SrTiO_3$ were grown fully strained to the substrate. The values of the lattice parameters remained constant in the whole volume of the thin film and no relaxation was observed even for the samples as thick as 50 nm. However, the out-of-plane lattice constants of the Ca doped compounds were much longer than that of the reference $SrRuO_3$ thin film in spite of the fact that the Ca^{2+} cations are significantly smaller than Sr^{2+} cations. We believe that this elongation results from a strain induced deformation of the RuO_6 octahedra. The exact nature of this phenomenon, observed also by others, remains an open question, since the explanations available in the literature cannot be directly applied to our samples.

The XPS core spectra were composed of several components reflecting different atomic surroundings of the elements. Such a complicated structure of the surface region, unexpected, considering perfection of the overall crystal lattice proved by other results is a consequence of the Ru deficiency in this region as well as excessive reaction with physisorbed hydrocarbons. A narrow and well defined component of the XPS spectra was attributed to the perovskite lattice of the interior of the thin film and the other components to the disordered surface region. Assuming a simple model in which a uniform layer of the material bound with adsorbates covers the thin film lattice it was possible to estimate the thickness of this layer to about 1 nm. However, a more appropriate description should take into account a partial mixing of the SrO excess material with the adsorbed carbon oxides and hydroxyls.

Long-term storage of the samples led to the extended in time further deterioration of the surface region. Interestingly, the gradient of Ru concentration between the interior and the surface of the thin film increased with time.

Improvement of the surface properties by a removal of contaminations seems to be a much more complex issue than previously reported. Thermal treatment allows removing some adsorbates but at the same time leads to the Ru loss, demixing of the alternating perovskite structure and a deterioration of the topography. Short-term annealing in vacuum at the temperature of about 500-600 ºC or oxidation at about 600-800 ºC affect only the surface region. Higher temperatures and extended time of the process induce changes in the bulk of the thin film. We recommend subsequent depositions of different layers and other types of treatments to be carried out in-situ, immediately after the $Sr_{1-x}Ca_xRuO_3$ deposition.

Electrochemical decomposition of the surface compounds under the STM and LC-AFM tips was observed even with a very low applied voltage. In the LC-AFM contact mode the reactions occurring below 1 V were attributed to the decomposition of the SrO-H_2O compounds, whereas a value of about 1 V seems sufficient to dismantle the edges of the SrO-RuO_2 atomic steps and possibly break the SrO-CO_y bonds. Therefore, in the designs of the nanodevices utilizing the $Sr_{1-x}Ca_xRuO_3$ thin film as a top electrode application of the electrical contacts requires special attention.

The $SrRuO_3$ and $Sr_{0.8}Ca_{0.2}RuO_3$ thin films on $SrTiO_3$ were produced as epitaxial single crystals albeit with imperfect interface and surface region, the $Sr_{0.8}Ca_{0.2}RuO_3$ thin films on $LaAlO_3$ and $Sr_{0.6}Ca_{0.4}RuO_3$ thin films on $SrTiO_3$ as separate or partly coalesced grains. A detailed analysis allowed characterization of the layers treated as a whole but also selectively for their different regions. Unfortunately, although several properties of the deposited layers, revealed in the course of the present work are interesting for further basic research at the same time greatly limit their possible applications. Nonetheless a well mastered process of synthesis followed by a precise description of the produced specimens is a key to understand and control their properties. It would be instructive to perform a similarly thorough investigation of the samples of these materials obtained with different deposition techniques. Each method introduces specific circumstances of layer growth and subsequently initial conditions determining their morphology. The comparison should allow distinguish the impact of production conditions (method artifacts) and intrinsic material properties.

Appendix A

Reported methods of the electronic band structure calculations for the $Sr_{1-x}Ca_xRuO_3$ system[127]

All the different theoretical calculations of the electronic band structure of the $Sr_{1-x}Ca_xRuO_3$ crystal start with the many-particle Schrödinger equation. The standard approach to solve this equation utilizes the Born-Oppenheimer approximation to decouple the electrons from ionic vibrations followed by the Hartree description allowing reduction of the interacting many-electron system to the problem of individual electron in an effective potential. The wave function of the N-electron system is then written as a product of one-electron wave functions and the effective potential a sum of the rigid field coming from the ions frozen in certain positions and the field determined from the distribution of all the other electrons. The single-electron Hartree equations can be solved self-consistently by assuming a particular set of eigenstates, calculating the effective potential and recalculating the eigenstates in successive iterations. It is common to use a spherically symmetric potential and a set of plane-wave states as the first approximation for the ground state.

This approach does not take into account the fact that a spherically symmetric potential of electron is deformed in the presence of another electron (electron correlations) or that a possibility of two identical electrons exchanging places may alter the energy of the eigenstates (exchange interactions). Both effects are included by a further modification of the potential.

In case of the calculations done for the $Sr_{1-x}Ca_xRuO_3$ compounds it is usually based on the local density approximation (LDA), local spin density approximation (LSDA) or generalized-gradient approximation (GGA). LDA postulates that the exchange-correlation energy functional in a certain point depends only on the density of electrons contained within a defined sphere around this point, LSDA involves two different spin densities and GGA additionally spin density gradients to expand and soften the bonds (all of them based on the density-functional theory).

In the crystalline materials the wave functions must satisfy the Bloch condition and the Pauli exclusion principle produces a quasi-infinite number of electronic states (electronic bands). To calculate their structure a proper approximation of the periodic potential is required.

The results reported for the $Sr_{1-x}Ca_xRuO_3$ crystal lattice were obtained with help of several models including atomic sphere approximation (ASA), muffin-tin approximation (MTA) and pseudopotential. Within ASA the crystal is divided into space-filling atomic spheres and the potential defined inside is spherically symmetric. MTA uses non-overlapping spheres centered at the atomic positions. Inside them the potential is spherically symmetric and outside approximated as a constant. Pseudopotential is based on orthogonalized plane-wave method in which the approximate correct solution to the crystal Schrödinger equation is a linear combination of plane waves and the Bloch functions formed from atomic orbitals describing the core states. The wave functions are described this way in the core and negligible in the interstitial regions and the lattice potential is substituted with a much weaker effective potential preserving the original eigenenergies. A different wave function is proposed in the augmented plane wave (APW) method. Inside the core the function is found by solving the appropriate free-atom Schrödinger equation. Outside the core the potential is approximated as constant and the function as a plane wave. Another wave function, used in the linear muffin thin orbital method, also consists of two parts, one calculated inside the muffin-tin sphere and second one assumed outside, both having matching values and slopes at the boundary surface.

It is important to remember that the approach to electronic band calculations within the density-functional theory is mainly designed for the systems with moderately correlated electrons, whereas the influence of correlations on the $Sr_{1-x}Ca_xRuO_3$ system is still unclear.

Appendix B

Calculation of oxygen partial pressure[128]

Oxygen partial pressure p_{O_2} was estimated for the process of reduction of the $SrRuO_3$ thin film at the hydrogen pressure p_{H_2} of $1\,bar$ and the temperature of $450\,°C$. The ambient atmosphere was treated as a hydrogen-steam mixture and the calculations made on a basis of the gas-phase (g) reaction

$$H_2(g) + O_2(g) \leftrightarrow H_2O(g)$$

Its standard Gibbs free energy change ΔG^0 at the temperature T is given by

$$\Delta G^0 = \Delta H^0 - T\,\Delta S^0$$

Standard enthalpy of the reaction ΔH^0 is equal to the enthalpy of formation of water vapor $\Delta H^0_{H_2O}$ and standard entropy change ΔS^0 is a difference between the standard molar entropies of the product and the reactants.

$$\Delta S^0 = S^0_{H_2O} - S^0_{H_2} - \frac{1}{2} S^0_{O_2}$$

The values of the $S^0_{H_2}$, $S^0_{O_2}$, $S^0_{H_2O}$ and $\Delta H^0_{H_2O}$ for the gaseous phase of each compound at $25\,°C$ were obtained from the thermodynamic tables[129]

$$S^0_{H_2} = 130.68\ J\,mole^{-1}K^{-1}$$

$$S^0_{O_2} = 205.152\ J\,mole^{-1}K^{-1}$$

$$S^0_{H_2O} = 188.835\ J\,mole^{-1}K^{-1}$$

$$\Delta H^0_{H_2O} = -241.826\ kJ\,mole^{-1}$$

At the annealing temperature of $450\,°C$ the calculated value of ΔG^0 is $-209.7\ kJ\,mole^{-1}$. If the reaction takes place under conditions different from the standard state the Gibbs free energy change can be written as

$$\Delta G = \Delta G^0 + R\,T\,\ln Q$$

where Q is the reaction quotient and R the gas constant. When the equilibrium is reached $\Delta G = 0$ and $Q = K$. The equilibrium constant K calculated using this approach is about $1.4 \cdot 10^{15}$. On the other hand the definition of the equilibrium constant K states that

$$K = \frac{p_{H_2O}}{p_{H_2}\sqrt{p_{O_2}}}$$

Having such a large K, even with an assumption that p_{H_2O} is as high as $10^{-7}\,bar$ – an ambient pressure measured during a similar experiment conducted in vacuum, one gets the value of p_{O_2} at the beginning of the reduction process well below $10^{-44}\,bar$. It means that at this moment the atmosphere surrounding the thin film is virtually free of O_2 molecules. Considering that a square $(1\,cm \times 1\,cm)$, $58\,nm$ thick $SrRuO_3$ sample is built of about $3 \cdot 10^{17}$ oxygen atoms and a $0.03\,dm^3$ quartz tube at $1\,bar$ and $450\,°C$ contains more than $3 \cdot 10^{20}$ H_2 molecules the oxygen released during even the most thorough reduction should not increase the value of p_{O_2} above $10^{-36}\,bar$, and that still denotes the absence of free oxygen molecules is the ambient.

[1] M. Mlynarczyk, K. Szot, A. Petraru, U. Poppe, U. Breuer, R. Waser and K. Tomala, J. Appl. Phys. **101**, 023701 (2007).
[2] M. Młynarczyk, K. Szot, U. Poppe, U. Breuer, S. Mi, B. Psiuk, E. A. Görlich, K. Tomala and R. Waser, Phys. Status Solidi A **210**, 239 (2013).
[3] H. Kobayashi, M. Nagata, R. Kanno and Y. Kawamoto, Mater. Res. Bull. **29**, 1271 (1994).
[4] G. Cao, C. S. Alexander, S. McCall, J. E. Crow and R. P. Guertin, Mater. Sci. Eng. **B63**, 76 (1999).
[5] B. C. Chakoumakos, S. E. Nagler, S. T. Misture and H.M. Christen, Physica B **241**, 358 (1998).
[6] C. W. Jones, P. D. Battel, P. Lightfoot and W. T. A. Harrison, Acta Crystallogr. **C45**, 365 (1989).
[7] W. Bensch, H. W. Schwalle and A. Reller, Solid State Ionics **43**, 171 (1990).
[8] M. V. Rama Rao, V. G. Sathe, D. Sornadurai, B. Panigrahi and P. Shripathi, J. Phys. Chem. Solids **62**, 797 (2001).
[9] G. L. Catchen and T. M. Rearick, Phys. Rev. B **49**, 1 (1994).
[10] C. B. Eom, R. J. Cava, R. M. Fleming, J. M. Phillips, R. B. van Dover, J. H. Marshall, J. W. P. Hsu, J. J. Krajewski and W. F. Peck, Jr., Science **258**, 1766 (1992).
[11] J. S. Anderson, J. Phys. **38**, C7 (1977).
[12] S. H. Oh and C. G. Park, Phil. Mag. **83**, 1307 (2003).
[13] R. J. Bouchard and J. L. Gillson, Mater. Res. Bull. **7**, 873 (1972).
[14] M. Shepard, P. F. Henning, G. Cao and J. E. Crow, J. Appl. Phys. **83,** 1 (1998).
[15] G. Cao, S. McCall, M. Shepard, J. E. Crow and R. P. Guertin, Phys. Rev. B **56**, 321 (1997).
[16] A. Kanbayasi, J. Phys. Soc. Jpn. **41**, 1876 (1976).
[17] B. Dabrowski, O. Chmaissem, P. W. Klamut, S. Kolesnik, M. Maxwell, J. Mais, Y. Ito and B. D. Armstrong, Phys. Rev. B **70**, 014423 (2004).
[18] M. Schneider, V. Moshnyaga, P. Gegenwart, Phys. Stat. Sol. B **247**, 577 (2010).
[19] R. M. Roshko, C. Viddal and W. Li, Physica B **343**, 30 (2004).
[20] K. Yoshimura, T. Iami, T. Kiyama, K. R. Thurber, A. W. Hunt and K. Kosuge, Phys. Rev. Lett. **83**, 4397 (1999).
[21] M. Rams, R. Kmiec, M. Kruzel, Z. Swiatkowska, J. Gurgul, K. Krolas and K. Tomala, J. Alloys Comp. **471**, 5-10 (2009).
[22] A. Banerjee, R. Prasad and V. Venugopal, J. All. Comp. **353**, 263 (2003).
[23] A. Banerjee, R. Prasad and V. Venugopal, J. All. Comp. **358**, 321 (2003).
[24] R. Vidya, P. Ravindran, A. Kjekshus, H. Fjellvåg and B. C. Hauback, J. Solid State Chem. **177**, 146 (2004).
[25] L. Pi, A. Maignan, R. Retoux and B. Raveau, J. Phys.: Condens. Matter **14**, 7391 (2002).
[26] W. Tong, F-Q. Huang and I-W. Chen, J. Phys.: Condens. Matter **23**, 086005 (2011).
[27] G. Cao, S. McCall, J. Bolivar, M. Shepard, F. Freibert, P. Henning, J. E. Crow and T. Yuen, Phys. Rev. B **54**, 21 (1996).
[28] I. M. Bradarić, I. Felner and M. Gospodinov, Phys. Rev. B **65**, 024421 (2002).
[29] I. Felner, U. Asaf, I. Nowik and I. Bradaric, Phys. Rev. B **66**, 054418 (2002).
[30] T. He and R. J. Cava, J. Phys.: Condens. Matter **13**, 8347 (2001).
[31] Y. J. Chang, J. I. Kim and C. U. Jung, J. Magn. **13**, 61 (2008).
[32] A. Grutter, F. Wong, E. Arenholz, M. Liberati, A. Vailionis, and Y. Suzuki, J. Appl. Phys. **107**, 09E138 (2010).
[33] F. Sánchez, G. Herranz, I. C. Infante, J. Fontcuberta, M. V. García-Cuenca, C. Ferrater and M. Varela, Appl. Phys. Lett. **85**, 1981 (2004).
[34] R. H. Chae, R. A. Rao, Q. Gan and C. B. Eom, J. Electroceram. **4**, 345 (2000).
[35] T. Fukuda and H. J. Scheel, *Crystal Growth Technology* (Wiley, New York, 2003).
[36] M. Hiratani, C. Okazaki, K. Imagawa and K. Takagi, Jpn. J. Appl. Phys. **35**, 6212 (1996).
[37] X. Fang and T. Kobayashi, J. Appl. Phys. **90**, 162 (2001).
[38] S. S. Kim, T. S. Kang and J. H. Je, J. Appl. Phys. **90**, 4407 (2001).
[39] Q. Gan, R. A. Rao and C. B. Eom, Appl. Phys. Lett. **70**, 1962 (1997).
[40] Z. R. Dai, S. Y. Son, B. S. Kim, D. K. Choi and F. S. Ohuchi, Mat. Res. Bull. **34**, 933 (1999).
[41] S. Ohashi, M. Lippmaa, N. Nakagawa, H. Nagasawa, H. Koinuma and M. Kawasaki, Rev. Sc. Instr. **70**, 178 (1999).
[42] M. A. López de la Torre, Z. Sefrioui, D. Arias, M. Varela, J. E. Villegas, C. Ballesteros, C. León and J. Santamaría, Phys. Rev. B **63**, 052403-1 (2001).
[43] N. Okuda, K. Saito and H. Funakubo, Jpn. J. Appl. Phys. **39**, 572 (2000).
[44] J. P. Mercurio, J. H. Yi, M. Manier and P. Thomas, J. All. Comp. **308**, 77 (2000).
[45] E. Vasco, R. Dittmann, S. Karthäuser and R. Waser, Appl. Phys. A **79**, 1461 (2004).

[46] R. A. Rao, Q. Gan, C. B. Eom, R. J. Cava, Y. Suzuki, J. J. Krajewski, S. C. Gausepohl and M. Lee, Appl. Phys. Lett. **70**, 3035 (1997).
[47] Y. S. Lee, J. Yu, J. S. Lee, T. W. Noh, T.-H. Gimm, H.-Y. Choi and C. B. Eom, Phys. Rev. B **66**, 041104 (2002).
[48] S. Hyun, J. H. Cho, A. Kim, J. Kim, T. Kim and K. Char, Appl. Phys. Lett. **80**, 1574 (2002).
[49] P. Khalifah, I. Ohkubo, H. M. Christen, and D. G. Mandrus, Phys. Rev. B: Condens. Matter **70**, 134426-1 (2004).
[50] F. Ricci, M. F. Bevilacqua, F. Miletto Granozio and U. Scotti di Uccio, Phys. Rev. B **65**, 155428 (2002).
[51] H. Funakubo, T. Oikawa, N. Higashi and K. Saito, J. Crystal Growth **235**, 401 (2002).
[52] C. U. Jung, H. Yamada, M. Kawasaki and Y. Tokura, Appl. Phys. Lett. **84**, 2590 (2004).
[53] K. Terai, T. Ohnishi, M. Lippmaa, H. Koinuma and M. Kawasaki, Jpn. J. Appl. Phys. **43**, 227 (2004).
[54] I. Stolichnov, A. Tagantsev, N. Setter, J. S. Cross and M. Tsukada, Appl. Phys. Lett. **75**, 1790 (1999).
[55] M. Hrovat, S. Bernik, J. Holc, T. Padeznik and M. Kosec, J. Mat. Sc. **35**, 1725 (2000).
[56] R. Domel, C. L. Jia, C. Copetti, G. Ockenfuss and A. I. Braginski, Supercond. Sci. Technol. **7**, 277 (1994).
[57] T. Yoshimura and S. Trolier-McKinstry, Appl. Phys. Lett. **81**, 2065 (2002).
[58] P. Lu, F. Chu, Q. X. Jia and T. E. Mitchell, J. Mater. Res. **13**, 2302 (1998).
[59] X. D. Wu, S. R. Foltyn, R. C. Dye, Y. Coulter and R. E. Muenchausen, Appl. Phys. Lett. **62**, 2434 (1993).
[60] A. P. Mackenzie, J. W. Reiner, A. W. Tyler, L. M. Galvin, S. R. Julian, M. R. Beasley, T. H. Geballe and A. Kapitulnik, Phys. Rev. B **58**, R13 318 (1998).
[61] R. A. Rao, D. B. Kacedon and C. B. Eom, J. Appl. Phys. **83**, 6995 (1998).
[62] C. S. Alexander, G. Cao, S. McCall and J. E. Crow, J. Appl. Phys. **85**, 6223 (1999).
[63] C. Bansal, H. Kawanaka, R. Takahashi and Y. Nishihara, J. All. Comp. **360**, 47 (2003).
[64] M. Wohlfahrt-Mehrens, J. Schenk, P. M. Wilde, E. Abdelmula, P. Axmann and J. Garche, J. Pow. Sour. **105**, 182 (2002).
[65] Gayathri N. Banerjee, R. N. Bhowmik and R. Ranganathan, J. Phys.: Cond. Matt. **13** 9481 (2001).
[66] H. -M. Christen, L. A. Boatner, J. D. Budai, M. F. Chisholm, L. A. Gea, D. P. Norton, C. Gerber and M. Urbanik, Appl. Phys. Lett. **70**, 2147 (1997).
[67] L. Miéville, T. H. Geballe, L. Antognazza and K. Char, Appl. Phys. Lett. **70**, 126 (1997).
[68] S. H. Oh and C. G. Park, J. Appl. Phys. **95**, 4691 (2004).
[69] C. H. Ahn, R. H. Hammond, T. H. Geballe, M. R. Beasley, J. –M. Triscone, M. Decroux, Ø. Fischer, L. Antognazza and K. Char, Appl. Phys. Lett. **70**, 206 (1997).
[70] C. L. Chen, Y. Cao, Z. J. Huang, Q. D. Jiang, Z. Zhang, Y. Y. Sun, W. N. Kang, L. M. Dezaneti, W. K. Chu and C. W. Chu, Appl. Phys. Lett. **71**, 1047 (1997).
[71] Y. L. Qin, C. L. Jia, K. Urban, J. H. Hao and X. X. Xi, J. Crystal Growth **252**, 279 (2003).
[72] D. Halley, C. Rossel, D. Widmer, H. Wolf and S. Gariglio, Mat. Sc. Eng. B **109**, 113 (2004).
[73] J. Shin, S. V. Kalinin, H. N. Lee, H. M. Christen, R. G. Moore, E. W. Plummer and A. P. Baddorf, Surf. Sci. **581**, 118 (2005).
[74] H. Paik, J. Hong, Y. Jang, Y. C. Park, J. Y. Lee, H. Song and K. No, Phys. Status Solidi A **206**, 1478 (2009).
[75] L. Capogna, A. P. Mackenzie, R. S. Perry, S. A. Grigera, L. M. Galvin, P. Raychaudhuri, A. J. Schofield, C. S. Alexander, G. Cao, S. R. Julian, Y. Maeno, Phys. Rev. Lett. **88,** 076602 (2002).
[76] Z. Sefrioui, D. Arias, M. A. Navacerrada, M. Varela, G. Loos, M. Lucía, J. Santamaría, F. Sánchez-Quesada and M. A. López de la Torre, Appl. Phys. Lett. **73**, 3375 (1998).
[77] J. Park, S.-J. Oh, J.-H. Park, D. M. Kim and C. B. Eom, Phys. Rev. B **69**, 085108 (2004).
[78] J. Kim, J. Chung and S.-J. Oh, Phys. Rev. B **71**, 121406 (2005).
[79] S. C. Gausepohl, M. Lee, R. A. Rao and C. B. Eom, Phys. Rev. B **54**, 8996 (1996).
[80] P. B. Allen, H. Berger, O. Chauvet, L. Forro, T. Jarlborg, A. Junod, B. Revaz and G. Santi, Phys. Rev. B **53**, 4393 (1996).
[81] G. Santi and T. Jarlborg, J. Phys.: Cond. Matt. **9**, 9563 (1997).
[82] J. Okamoto, T. Mizokawa, A. Fujimori, I. Hase, N. Nohara, H. Takagi, Y. Takeda and M. Takano, Phys. Rev. B **60**, 2281 (1999).
[83] J. Manica, M. Abbate, J. A. Guevara and S. L. Cuffini, Physica B **354**, 39 (2004).
[84] K. Maiti and R. S. Singh, Phys. Rev. B **71**, 161102(R) (2005).
[85] A. T. Zayak, X. Huang, J. B. Neaton and K. M. Rabe, Phys. Rev. B **74**, 094104 (2006).
[86] J. M. Rondinelli, N. M. Caffrey, S. Sanvito and N. A. Spaldin, Phys. Rev. B **78**, 155107 (2008).

[87] H. M. Christen, C. M. Rouleau, I. Ohkubo, H. Y. Zhai, H. N. Lee, S. Sathyamurthy, and D. H. Lowndes, Rev. Sci. Instrum. **74**, 4058 (2003).
[88] M. Schneider, V. Moshnyaga, P. Gegenwart, J. Phys.: Conf. Ser. **200**, 012178 (2010).
[89] M. Takizawa, D. Toyota, H. Wadati, A. Chikamatsu, H. Kumigashira, A. Fujimori, M. Oshima, Z. Fang, M. Lippmaa, M. Kawasaki, and H. Koinuma, Phys. Rev. B **72**, 060404 (2005).
[90] R. Mathieu, A. Asamitsu, H. Yamada, K. S. Takahashi, M. Kawasaki, Z. Fang, N. Nagaosa, and Y. Tokura, Phys. Rev. Lett. **93**, 016602 (2004).
[91] P. B. Mozhaev, P. V. Komissinski, N. P. Kukhta, A. Kiihle, G. A. Ovsyannikov and J. L. Skov, J. Supercond. **10**, 3 (1997).
[92] J. F. Watts and J. Wolstenholme, *An introduction to surface analysis by XPS and AES* (Wiley, New York, 2003).
[93] J. F. Moulder, W. F. Stickle, P. E. Sobol and K. D. Bomben, *Handbook of X-ray Photoelectron Spectroscopy* (Perkin-Elmer Corp., Eden Prairie MN, 1992).
[94] P. J. Cumpson and M. P. Seah, Surf. Interface Anal. **25**, 430 (1997).
[95] H. Bakhru, *Encyclopedia of Materials: Science and Technology*, 8242 (Elsevier, Amsterdam and New York, 2001).
[96] L. R. Doolittle, Nucl. Inst. Meth. **B15**, 227 (1986).
[97] J. C. Vickerman, *Surface Analysis: The Principal Techniques* (Wiley, Chichester, 1997).
[98] P. J. Goodhew, J. Humphreys and R. Beanland, *Electron microscopy and analysis* (Taylor & Francis, London and New York, 2001).
[99] R. A. Wilson and H. A. Bullen, *E-Learning Module: Introduction to Scanning Probe Microscopy*, JASDL, Article ID 100043 (2007).
[100] Ch. R. Blanchard, *The Chemical Educator: Atomic Force Microscope*, T. 1, Nr 5 (Springer-Verlag, New York, 1996).
[101] L. Klein, J. S. Dodge, C. H. Ahn, J. W. Reiner, L. Mieville, T. H. Geballe, M. R. Beasley and A. Kapitulnik, J. Phys.: Cond. Matt. **8**, 10111 (1996).
[102] L. J. van der Pauw, Philips Tech. Rev. **20**, 220 (1958).
[103] J. Lin, K. Natori, Y. Fukuzumi, M. Izuha, K. Tsunoda, K. Eguchi, K. Hieda and D. Matsunaga, Appl. Phys. Lett. **76**, 2430 (2000).
[104] A. J. Hartmann, M. Neilson, R. N. Lamb, K. Watanabe and J. F. Scott, Appl. Phys. A **70**, 239 (2000).
[105] Y. Zhang, J. Lian, Z. Zhu, W. D. Bennett, L. V. Saraf, J. L. Rausch, C. A. Hendricks, R. C. Ewing and W. J. Weber, J. Nucl. Mater. **389**, 303 (2009).
[106] C. L. Jia, J. Rodríguez Contreras, J. Schubert, M. Lentzen, U. Poppe, H. Kohlstedt, K. Urban and R. Waser, J. Crystal Growth **247**, 381 (2003).
[107] J. Q. He, E. Vasco, R. Dittmann and R. H. Wang, Phys. Rev. B **73**, 125413 (2006).
[108] R. Muenstermann, T. Menke, R. Dittmann, S. Mi, C. L. Jia, D. Park and J. Mayer, J. Appl. Phys. **108**, 124504 (2010).
[109] V. P. Zlomanov, Inorg. Mat. **42**, S19 (2006).
[110] G. Herranz, B. Martínez, J. Fontcuberta, F. Sánchez, C. Ferrater, M. V. García-Cuenca and M. Varela, Phys. Rev. B **67**, 174423 (2003).
[111] Y. Z. Yoo, O. Chmaissem, S. Kolesnik, B. Dabrowski, M. Maxwell, C. W. Kimball, L. McAnelly, M. Haji-Sheikh and A. P. Genis, J. Appl. Phys. **97**, 103525 (2005).
[112] C. Aruta, M. Angeloni, G. Balestrino, P.G. Medaglia, P. Orgiani, A. Tebano and J. Zegenhagen, Eur. Phys. J. B **46**, 251 (2005).
[113] G. K. Williamson and W. H. Hall, Acta Metall. **1**, 22 (1953).
[114] E. J. Mittemeijer and U. Welzel, Z. Kristallogr. **223**, 552 (2008).
[115] R. Perez-Casero, J. Perrière, A. Gutierrez-Llorente, D. Defourneau, E. Millon, W. Seiler and L. Soriano, Phys. Rev. B **75**, 165317 (2007).
[116] D. J. Singh, J. Appl. Phys. **79**, 4818 (1996).
[117] K. Fujioka, J. Okamoto, T. Mizokawa, A. Fujimori, I. Hase, M. Abbate, H. J. Lin, C. T. Chen, Y. Takeda and M. Takano, Phys. Rev. B **56**, 6380 (1997).
[118] G. Bertsche, W. Clauss, F. E. Prins and D. P. Kern, J. Vac. Sci. Technol. B **16**, 2833 (1998).
[119] L. Pellegrino, I. Pallecchi, D. Marré, E. Bellingeri and A. S. Siri, Appl. Phys. Lett. **81**, 3849 (2002).
[120] F. Peter, A. Rüdiger, R. Dittmann, R. Waser, K. Szot, B. Reichenberg and K. Prume, Appl. Phys. Lett. **87**, 082901 (2005).
[121] K. T. Jacob, K. T. Lwin and Y. Waseda, Mat. Sci. Eng. **B103**, 152 (2003).
[122] K. T. Jacob, K. T. Lwin and Y. Waseda, J. Electrochem. Soc. **150**, E227 (2003).
[123] C. Noguera, *Physics and Chemistry at Oxide Surfaces*, (Cambridge University Press, New York, 1996).

[124] J. D. Baniecki, M. Ishii, K. Kurihara, K. Yamanaka, T. Yano, K. Shinozaki, T. Imada and Y. Kobayashi, J. Appl. Phys. **106**, 054109 (2009).
[125] R. Ohara, T. Schimizu, K. Sano, M. Yoshiki and T. Kawakubo, Jpn. J. Appl. Phys. **40**, 1384 (2001).
[126] K. Szot, W. Speier, J. Herion and Ch. Freiburg, Appl. Phys. A: Solids Surf. **64**, 55 (1997).
[127] F. Duan and J. Guojun, *Introduction to Condensed Matter Physics, Vol. 1* (World Scientific, Singapore, 2005).
[128] D. L. Reger, S. R. Goode and D. W. Ball, *Chemistry: Principles and Practice, 3rd Edition* (Cengage Learning, Belmont, 2010).
[129] J. D. Cox, D. D. Wagman and V. A. Medvedev, *CODATA Key Values for Thermodynamics* (Hemisphere Publishing, New York, 1989).